Photodissociation dynamics of molecules on surfaces

Takehito Senga

Department of Molecular Engineering,
Graduate School of Engineering,
Kyoto University

1999

CONTENTS

General introduction

In the last several decades, the high-performance light sources, e.g. a super high pressure mercury lamp, easy operating lasers (Nd:YAG, dye, excimer), synchrotron radiation and so on, have been developed, and easily used for academic and industrial scenes. The field of the photochemistry is now rapidly and widely growing, and the investigations are fairly keeping not only the science people but also engineers and general people on an attention. Similarly, the surface science has also grown as a vacuum technology advance. Actually, these technologies play the most important key-roll in the field of new material developments and semiconductor-device fabrications. Nowadays, it is impressed that applications of the surface photochemical reactions are likely to precede the fundamental studies of it, and an understanding of the surface photo-enhanced process electronically and molecular-dynamically is persuaded. It seems, therefore, only nature that the photochemistry and surface science should have been harmonically extended to provide an experimental technique for investigations of the reaction between the light and solid surface.

As a fundamental study, in this thesis, reactions between simple molecular adsorbates (Cl_2, HCl, NO_2, N_2O_4, N_2O_3) on the solid surface (a semiconductor, metal and water ice) and visible – ultraviolet light sources (Xe arc lamp, cw Ar^+ laser, the second, third, fourth harmonic lights of YAG laser, ArF, KrF and XeCl excimer lasers) are examined. The adsorption states of the molecules are investigated by the surface analyzing techniques (X-ray photoelectron spectroscopy, ultra-violet photoelectron spectroscopy, temperature programmed desorption spectrometry, Fourier-transformed Infrared reflective absorption spectroscopy), and the desorbing molecules are detected by the Quadra-pole mass spectrometer and laser induced multi-photon ionization technique.

In the Chapter 1 the author reports on the etching reaction of HCl and Cl_2 on a single crystal GaAs(100) surface. The reaction mechanism between molecules on a semiconductor surface and various laser lights is discussed. In the Chapter 2 and 3, the reaction between N_xO_y molecules on a single crystal

Au(111) surface and the light of a monochromatized Xe arc lamp is investigated stoichiometrically. The desorption-yield spectrum of these adsorbates on the surface is obtained respectively. Photochemical reactions of these molecules on the insulator surface (ice surface) are also examined partially. In the Chapter 4, the author investigates the photochemical reaction dynamics of N_2O_4 on a polycrystalline Au (111) surface with excimer lasers. Rotational, vibrational and translational energy distributions of the desorbing NO are obtained. The reaction mechanism will be discussed in this chapter. At the last, all excitation mechanisms concluded in this thesis will be summarized in the last section, as a general conclusion.

Chapter 1
Photochemical reactions of HCl and Cl_2 on GaAs surface

1.1 Introduction

Etching processes on semiconductors

Very-large-scale-integrated-circuit (VLSI) technology was started in the middle of the 1970's as a technology for 64K-bit dynamic random access memory and still has a significant impact on the electronic industry. The number of memory bits in dynamic memory chips in near future is predicted to be some gigabits. On this progress, one of the most important key-technology has been dry etching. It is used to make a small device structure on the semiconductor wafer and a contact hole on the insulator. This result in a great interest of the electronic industry for research which might give an insight into the fundamental possibilities and limitations of plasma etching and possible other new techniques.

In order to produce semiconductor nano-structures such as quantum wires, resist patterns must be transferred into the layers comprising the device. Etching process for the surface flatness in atomic order and transferring the patterns is to selectively remove unmasked portions of a layer. This technique is commonly used in VLSI processing because of their potential for very-high-fidelity transfer of resist patterns, and provide selectivity between different GaAs over AlGaAs in field effect transistor fabrication.

Since etching is often followed by epitaxial growth on the etched planes, it is essential to produce damage and contamination free, clean etched surfaces. Traditional techniques, such as plasma or chemical wet etching can have serious drawbacks; plasma etching often results in ion-bombardment induced deterioration and wet etching may result in surface oxidation and contamination by etchant solution. This has lead to a considerable interest in "dry etching" techniques, and in particular the use of molecular chlorine as the etchant. Due to their ease of production and their high reactivity, halogen atoms play essential roles in both etching and desorption system. At room temperature the formation of $GaCl_x$(x=1, 2, 3) compounds is occurred on the

surface. These reaction products can be removed in a thermal reaction, thus allowing the etching to processes. Despite considerable effort the dominant processes occurring in the GaAs system, the identity and role of the surface intermediates are still far from well understood.

GaAs crystal is an extremely attractive material because of its potential for high-speed devices and its suitability for monolithic optoelectronic integration, including digital, microwave, and optical circuits. Especially, laser diodes and light emitting diodes made of GaAs substrates are often used for sensing devices in environmental scientific measurements. For example, InGaAsP diode lasers have properties that make them well suited to detection of trace gases by optical absorption. CH_4, CO_2 and H_2O molecules have characteristic absorption bands in the 1.2-1.7 μm wavelength region where InGaAsP diode lasers operate. Single-frequency lasers can be tuned so that an output wavelength coincident with a specific gas-absorption line can be obtained. Detection techniques based on high-frequency modulation yield sensitivities for measuring one ppm absorbance or smaller. In the study on the desorption products from steady-state continuous etching of GaAs by a molecular beam of Cl_2, Su et al. [1] it was found that rapid etching occurred at above 650 K, giving GaCl, As_2, and As_4 as the major desorption products, whereas below 650 K the etch rate was much slower and the main desorption products were As_4 and $GaCl_3$. The temperature programmed desorption spectroscopy (TPD) data [2] indicated that etching was suppressed below 350 K by the accumulation of arsenic products on the surface rather than by the accumulation of $GaCl_2$ and $GaCl_3$. The rapid increase of the etch rate above 650 K was attributed to the fast desorption of GaCl. The fact that the desorption rates of As_2 and As_4 increased rapidly above this temperature was also observed.

A recent study by Lishan and Hu [3] compared Cl_2 and HCl etching of GaAs both with and without a remote plasma. One of the findings of their study was that without the remote plasma, Cl_2 etched the surface at temperatures as low as 320 K whereas HCl did not etch the surface up to 520 K. Saito and Kondo[4] observed efficient HCl etching of GaAs for temperatures above 720 K. In addition, several studies confirmed the ability of HCl to remove surface oxide

from GaAs at room temperature [4, 5, 6] and to dramatically reduce surface carbon contamination [4]. Since the dosing of hydrogen atoms has also been found to remove carbon [7], it is likely that the mechanism of HCl etching involves formation of hydrocarbons such as CH_4 and C_2H_n (n=2, 4, 6).

By the way, the investigation of the laser has triggered a lot of research making use of its specific properties. Besides the spectroscopic techniques, in which properties like small band width and high coherence are of importance, a lot of effort has been put into its use as a tool in process development. At the moment, the laser processes applied in industry like cutting, cladding, drilling and welding, only make use of the high power density of the processes can developed which use its special properties. In several research laboratories, lasers are used to modify surfaces. It has been shown that semiconductor surface damage, caused by e.g. ion bombardment, can be annealed by laser heating [8,9] also implanted dope in wafers can be redistributed applying a short laser pulse [10]. It is concluded that electronic excitation effects do not cause these processes but the thermal effect initiated by the laser irradiation. But of course, this does not mean that electronic excitation effects would not play a decisive role in other laser-initiated processes. Since direct bond breaking can be induced in solids with photons that have an energy larger than the binding energy, It might be possible that the laser assisted dry etching process is achieved by using its direct electronic excitation, making the etching process in lesser damage and lower temperature.

In this chapter, the mechanisms of thermal etching reactions on undoped GaAs (100) surface with HCl or Cl_2, have been studied using X-ray and ultraviolet photoelectron spectroscopy. The photoirradiation effect on the GaAs etching processes and its wavelength dependence have been also studied to examine the possibility of etching at low temperature.

References

[1] C. Su, H. Hou, G. H. Lee, Z. -G. Dai, M. F. Vernon and B. E. Bent, J. Vac. Sci. Technol., in press.

[2] A. Ludviksson, M. D. Xu and R. M. Martin, Surf. Sci. **277**, 282 (1992).

[3] D. G. Lishan and E. L. Hu, J. Vac. Sci. Technol. **B 8**, 1951 (1990).

[4] J. Saito and K. Kondo, J. Appl. Phys. **67**, 6274 (1990).

[5] J. Massies and J. P. Contour, Jpn. J. Appl. Phys. **26**, L38 (1987).

[6] J. P. Contour et al., J. Vac. Sci. Technol. **B 5**, 730 (1987).

[7] A. Takamori, S. Sugata, K. Asakawa, E. Miyauchi and H. Hashimoto, Jpn. J. Appl. Phys. **26**, L142 (1987).

[8] W. F. Tseng, J. W. Mayer, U. S. Campisano, G. Foti and E. Rimini, Appl. Phys. Lett. **32**, 824 (1978).

[9] J. Narayan, C. W. White, M. J. Aziz, B. Stritzker and A. Walthuis, J. Appl. Phys. **57**, 564 (1985).

[10] R. F. Wood, C. W. White and R. T. Young, *Semiconductors and Semimetals* **23**, (1984).

1.2 Experimental

1.2.1 Photoelectron spectroscopy (XPS and UPS)

The theoretical foundation of photoelectron spectroscopy was laid way back in 1905 [1], when Einstein wrote his well-known photoeffect equation:

$$h\nu = E_B + E_K \qquad (1\text{-}1)$$

where hν is incident photon energy, E_B is the binding energy of the electron in matter and E_K is the kinetic energy of the ejected electron. The method of photoelectron spectroscopy can be summed up as the measurement of the kinetic energy of the electron ejected by an incident photon. Knowing these values, it is easy to calculate E_B, which is a sensitive characteristic of chemical bonds in a compound and is related to the energy of ionization.

Figure 1-1 shows the schematic diagram of the principle of photoelectron spectroscopy. In Fig. 1-1, electronic orbitals of an atom or a molecule are divided into core and valence orbitals. A monochromatic source of X-ray (100 - 1 keV) may be used to remove core and valence electrons and the technique is often referred to as X-ray photoelectron spectroscopy (XPS). On the other hand, ultraviolet radiation (10 - 100 eV) has sufficient energy to remove only valence electrons and such a source is used in ultraviolet photoelectron spectroscopy (UPS).

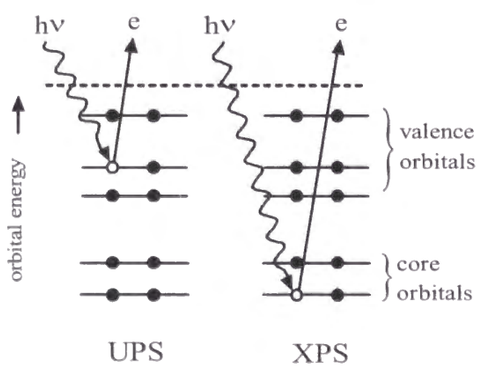

Figure 1-1. Processes for photoelectron emission from core and valence orbitals in XPS photoelectron spectroscopy (XPS) and ultraviolet photoelectron spectroscopy (UPS).

In the case of the emission of photoelectron from solid, the electron transport in the solid has to be considered, which can be ignored in atoms or molecules in the gas phase. The electric potentials applied between the solid sample and the spectrometer should be taken into account.

Basic processes

To explain the basic physical processes giving rise to typical features in a photoemission spectrum, Fig. 1-2 shows the schematic of diagram an X-ray excited photoemission spectrum, which has a wide energetic range. The upper part of Fig. 1-2 shows an XPS spectrum of a metal in the second row of the periodic table. The spectrum has the appearance of sloped steps with sharp lines at the high-energy edge of the steps. The total width of the spectrum is hν-ϕ, where ϕ is the work function of the sample and in our case this value is estimated to be 5.0 eV. The lower part of Fig. 1-2 shows schematic diagrams of the processes that lead to the characteristic features in the spectrum. The diagrams illustrate the primary excitation processes of the photoelectron formation. The photon hν is absorbed by a core electron or valence electron, leading to a photoionization process. The binding energy of the emitted electron is determined by subtracting the photon energy from the measured kinetic energy of the core line,

$$E_B = h\nu - E_K, \qquad (1\text{-}2)$$

The binding energy represents, apart from a small correction termed relaxation shift, the one-electron energy level of the core shell, so XPS allows a direct observation of core terms. This fact immediately provides chemical specificity for the spectra. In a different chemical environment the core levels exhibit a small shift due to the different contributions of the charge density of the valence electrons at the core orbit. This chemical shift permits conclusions on

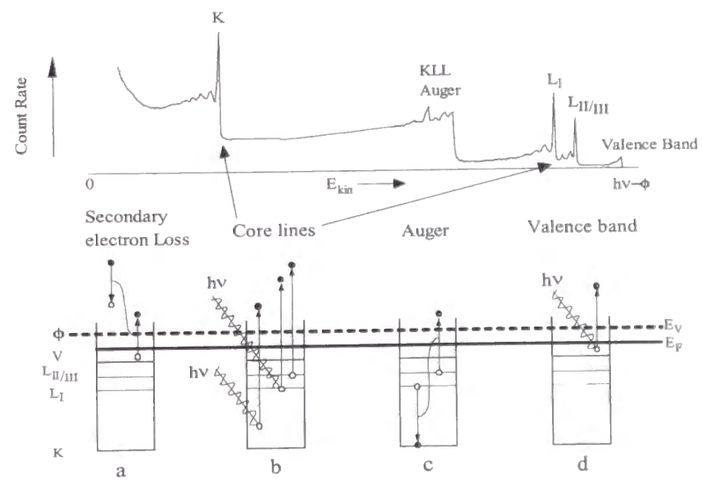

Figure 1-2 Typical XPS spectrum and basic processes of the photoelectron emissior
(a) Inelastic loss, secondary electrons and plasmon satelites.
(b) Direct excitation of core electrons.
(c) Hole deexcitation via the Auger process.
(d) Direct excitation of valence electrons.

the chemical bonds of the atom involved, making its observation very attractive in chemistry. The electrons with the highest kinetic energy in the spectra reflect the density of states in the valence band, with possible intensity modulations due to cross-section variations for electrons of different orbital character.

After excitation and emission of a core electron a hole is left in the core shell. This hole can be filled either by radiative deexcitation, giving rise to a characteristic X-ray spectrum, or by an Auger process. The electrons emitted by the Auger process, which is the dominant deexcitation mechanism for elements lighter than Z≈35, are observable in the XPS spectrum. Diagram c in Fig. 1-2 schematically shows a KLL Auger process. Here a hole in the K shell is filled by an electron from the L shell. Another L electron carriers away the energy arising from this process. Auger lines are independent of the way the core hole has been created, so they are found at the same kinetic energy for photon- and electron-excited spectra. Being element specific, those lines may also be used for chemical identification. Each peak in the spectrum is accompanied, on the low kinetic energy side, by a characteristic loss spectrum. Core electrons may excite collective electron oscillations, plasmons, during their excitation or emission, so bulk and surface plasmon loss lines are found on the low energy side of each sharp structure. This and many other energy loss mechanisms lead to the low-energy tails forming the characteristic overall step shape of the spectra. Figure 1-2 shows the process of secondary electron

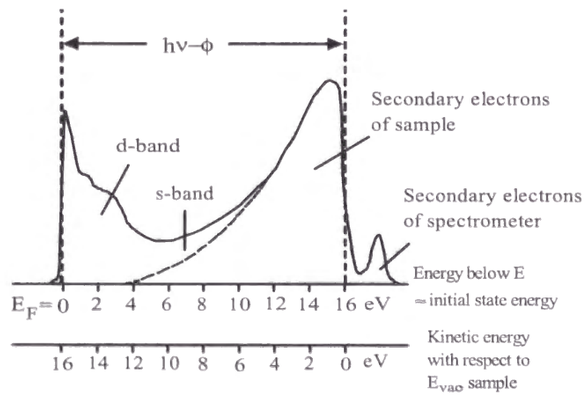

Figure 1-3. Typical shape of an UP spectrum excited by He I radiation. The relative intensities of primary and secondary electrons are very dependent on experimental arrangements. f is the work function of the system. hn is the photon energy (21 eV).

emission, where a hot electron loses energy by creating an electron-hole pair in the valence band. These secondary electrons give rise to the huge low-energy hump in photoemission spectra.

XPS has the following characteristic. (a) Large energetic probing depth makes observations of core levels possible. This results in chemical specificity. (b) XPS is not intrinsically very surface sensitive. This spatial information depth is limited by the electron mean free path to 50 Å. But the combination of chemical specificity and high sensitivity makes it an attractive tool for the study of adsorbates. (c) Chemical shifts on adsorbates permit conclusions on chemisorption bonding. However, the interpretation is complicated due to atomic and extra-atomic relaxation. (d) Valence states may be directly observed. Usually the resolution is not sufficient to show fine details, unless a x-ray monochromator is used to reduce the line width of the light source. (e) Energy-loss structure and Auger lines are observable in XPS spectra.

True secondary electrons produced by the photoelectrons surpass the potential barrier at the sample surface down to

$$E_K(s) = 0. \tag{1-3}$$

The cut-off of emission then occurs if the secondary electron has energy ϕ with respect to the Fermi level. The principal shape of an UPS spectrum of a d-bond metal is shown in Fig. 1-3. For the reason considered above, the onset of emission at E_F is taken as the energy zero. Emission down to some eV below E_F displays the density of states of the metal. The increase in emitted intensity towards lower energy is due to secondary emission, the sudden drop in signal indicates that the condition in Eq. 1-3 is met. The maximum kinetic energy (at the Fermi level), as determined by the spectrometer, is given by

$$E_K(sp)_{max} = h\nu - \phi_{sp}, \tag{1-4}$$

where ϕ_{sp} is a target region exhibit specific work function.

The minimum value (at the cut-off) is located at

$$E_K(sp)_{min} = \phi - \phi_{sp}, \tag{1-5}$$

where ϕ is a target region exhibit specific work function.

The width of the spectrum E therefore amounts to

$$\Delta E = \left[E_K(sp)_{max} - E_K(sp)_{min}\right] = h\nu - \phi \tag{1-6}$$

so the work function of the sample is available through

$$\phi = h\nu - \Delta E. \qquad (1\text{-}7)$$

A complication arises from the secondaries produced in the spectrometer itself. A separation of secondaries from the sample and the spectrometer can be obtained by placing the sample at a negative potential of some volts with respect to the analyzer. In this way the whole spectrum emitted from the sample is shifted toward higher $E_{kin}(sp)$ values and spectrometer inherent background is separated from the sample emission.

UPS is understood as excited by resonance light sources in the 21.2 and 40.8 eV range. A short electron mean free path in the sample makes those spectra surface sensitive. The energy probing depth is sufficient to cover the valence band of most solids. With UPS the change of chemical environment of an atom and a molecule may be also observed for surfaces covered with adsorbed layers and may be related to the electronic structure of surface adsorbate bond.

UPS has the following characteristics; (a) intensities of available light sources are high, permitting relatively easy angle-resolved studies; (b) resolution is high and usually limited by analyzer performance; (c) surface sensitivity is achieved by the surface photoelectric effect at lower photon energies; (d) valence levels, involved in bonding or not, are directly observed with high resolution; (e) surface and volume contributions are intermixed and very difficult to distinguish.

1.2.2 Angle-resolved XPS

Angle-resolved photoelectron spectroscopy has a rather long history, as recently reviewed by Jenkin *et al.*[2]. However, the current interest in angle-resolved X-ray photoelectron spectroscopy (ARXPS) as applied to solids and surfaces in only approximately twenty years old, having begun with observations of diffraction-induced channeling effects in single-crystal specimens by Siegbahn *et al.*[3] and by Fadley and Bergstöm [4] and of enhanced surface sensitivity for grazing angles of emission by Fadley and Bergström [4]. A number of other effects of interest in surface science have been noted since these first studies, and several quantitative models have been developed for describing them.[5-7]

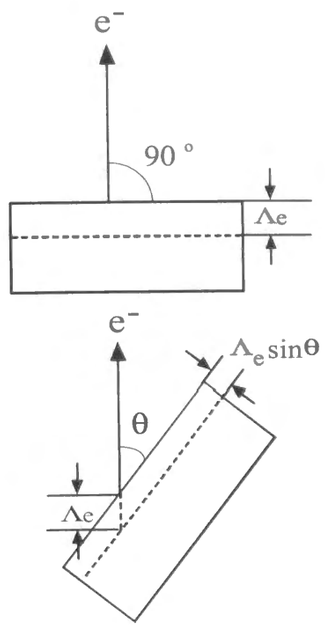

Figure 2-4 Schematic diagrams of the angle resolved photoelectron spectroscopy(ARPS). Λ_e is the escape depth of the photoelectron. At small θ angle (lower) the sensitivity of the surface species is enhanced.

The basic mechanism of surface sensitivity enhancement at grazing emission angles is illustrated in Fig. 1-4 for the case of an idealized homogeneous, semiinfinite, flat-surface specimen in which any effects due to atomic positional order are assumed to be fully averaged over. The mean free path for inelastic scattering Λ_e is further taken to be a constant independent of emission angle. In this case, the mean depth of no-loss photoelectron emission as measured perpendicular to the surface is exactly equal to Λ_e for normal emission or $\theta = 90°$, but it decreases as $\Lambda_e \sin$ for non-normal emission. Consequently, in the case of a substrate (s) with a uniform thin overlayer (o) the angular variation of intensities is given by

$$I_s(\theta) = I_s \exp(-d / \Lambda_e \sin\theta) \qquad (1\text{-}8)$$

and

$$I_o(\theta) = I_o\{1 - \exp(d / \Lambda_e \sin\theta)\} \qquad (1\text{-}9)$$

where $I_o(\theta)$ and $I_s(\theta)$ are intensities of overlayer and substrate at θ respectively: I_0 is overlayer intensity at a certain angle and I_s is substrate intensity without overlayer at the same angle: d is the thickness of uniform overlayer on the substrate. However, the real case is usually complicated by the fact that the system geometry imposes a response function also dependence on. A useful summary of these effects for one particular spectrometer has been given by Dilks.[8]. This complication is avoided by measurements of relative values, $R(\theta)=I_o(\theta)/I_S(\theta)$, so that the instrument response function is canceled. Thus, as shown in Fig. 1-4, at low values of θ, R(θ) increases significantly.

Defining $K \equiv I_0/I_S$ then yields after Fadley's [9]

$$\ln\left[\frac{R(\theta)}{K}+1\right]=\frac{d}{\Lambda_e \sin\theta}. \qquad (1\text{-}10)$$

Equation 1-10 present linearized methods for plotting data versus 1/sin . The slopes of such plots are thus given by plus or minus the effective overlayer thickness $\tau \equiv d/\Lambda_e$

Atomic sensitivity factor

As shown in Eq. 1-11, the integrated intensity is divided by an atomic sensitivity factor, because each atom has its characteristic sensitivity,

$$\frac{S_1}{F_1}:\frac{S_s}{F_2}=I_1:I_2, \qquad (1\text{-}11)$$

where F_i is the XPS atomic sensitivity factor for the i-th element, S_i is integrated intensity of each peak, and I_i is signal intensity of each peak.

Concerning XPS atomic sensitivity factors (ASF) relative to fluorine atom F1s=1.00, the ASF applied here were 0.205 for C1s, 0.63 for O1s, 0.48 for Cl2p, 6.9 for $Ga2p_{3/2}$, 0.31 for Ga3d, 9.1 for $As2p_{3/2}$, and 0.38 for As3d and 3s. A concentration of each element was obtained from the XPS signal area divided by the corresponding ASF. Our ASF are in agreement with those given by Wagner et al.[10].

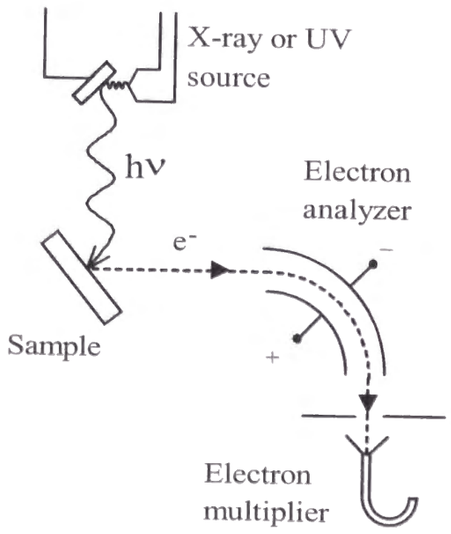

Figure 1-5. Schematic diagram of the experimental arrangement for the photoelectron spectroscopy(XPS and UPS) of solid surfaces.

Instrumentation

The basic elements for photoelectron spectroscopy are a light source, an electron energy analyzer and a detector system, as drawn schematically in Fig. 1-5. X-ray and ultraviolet light from the light source fall on the sample in an ultra-high-vacuum (UHV) chamber and eject electrons from core and valence levels. The ejected electrons pass through the slit into the electron energy analyzer which disperses electron kinetic energy.

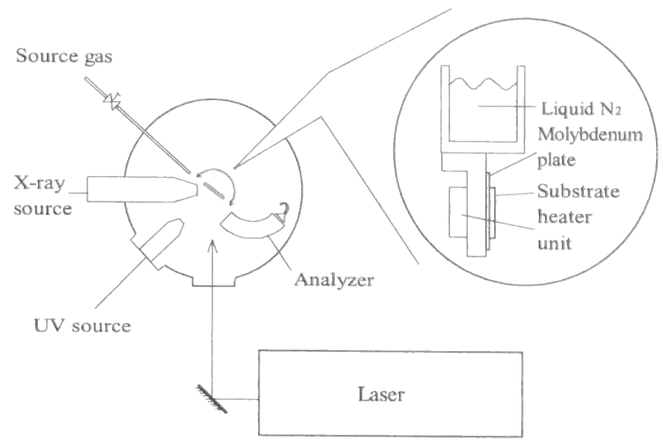

Figure 2-6 Schematic diagram of top view of XPS and UPS aparatus. The inset shows the sample holder that is cooled by liquid N and heated by a tantal heater unit.

Monochromatic electrons which pass through the analyzer is detected by the electron multiplier of the channeltron type.

Figure 1-6 shows a schematic diagram of our apparatus. The XPS and ultraviolet photoelectron spectroscopic (UPS) spectra were obtained using an apparatus (Vacuum Generator, Model ADES-400). The vacuum system had a base pressure in the 1×10^{-10} Torr range. The sample holder was mounted on the end of a rotatable manipulator with an XYZ-translation stage. The sample was placed on the molybdenum plate equipped with a stainless sample holder which has a tantalum wire heater unit. The sample temperature was measured with a type-K thermocouple. The sample could be cooled down to ~-100℃ with liq. N_2. Usually, the angle θ for the XPS measurement was set to 25° for surface-enhanced analysis, whereby the sensitivity for surface species is enhanced by shallow take-off angle measurement. For UPS, was set to 90°. The errors of XPS signal intensities are ±10%.

X-ray light source

Our XPS data were obtained with a using X-ray tube, in which an electron beam of several keV kinetic energy strikes an anode, providing characteristic radiation at fixed photon energy superimposed on a bremsstrahlung background. AlKα (h =1486.6 eV) radiation is used in our experiment. Thin

(~20 μm) aluminum window separates the tube from the spectrometer chamber and are sufficiently transmitting for photons in the energy range. This device allows separation of photoemitted electrons (photolines)-whose kinetic energy depends on hν and of Auger electron, whose energy is fixed. The main disadvantage of this X-ray source is inherent energy width of the line, which is about 1.2 eV. The energy resolution is thus limited by the primary radiation, rather than by properties of the energy analyzer.

UV light source

The operation of a resonance lamp is done with He. Fluorescence from the He(1s, 2p) state occurs with photon emission via so-called He-I radiation [11].

$$He(^1P_1) \rightarrow He(^1S_0) + h\nu(21.21eV) \qquad (1\text{-}12)$$

When the lamp is driven at lower pressures and higher currents, emission from a resonance line of ionized He^+ is increased, corresponding to photon energy of 40.8 eV. Typically, 10^{10} 10^{11} photons are emitted from the He I source.

Under our operation condition, the photoemitted current is about 55 mA and supplied voltage is 600 - 640 V.

Electron energy analyzer

The cylindrical analyzer [12] is used for the dispersion of photoelectron energy. Its principle is depicted in Fig. 1-7. The sector angle Θ in the ADES-400 machine is adjustable (generally Θ = 127°). Electrons entering the cylindrical section through the entrance slits are deflected by the transverse field, created by a voltage V_k applied between the two electrodes. An electron with velocity v describes a circular path with radius R depending on V_k. To a first approximation, electrons with energy eV_e can passthrough the exit slit when the values of V_e, V_k and the radii of curvature r_1 and r_2 fulfill the following expression,

$$\frac{1}{2}V_k = V_e \ln\frac{r_1}{r_2} \qquad (1\text{-}13)$$

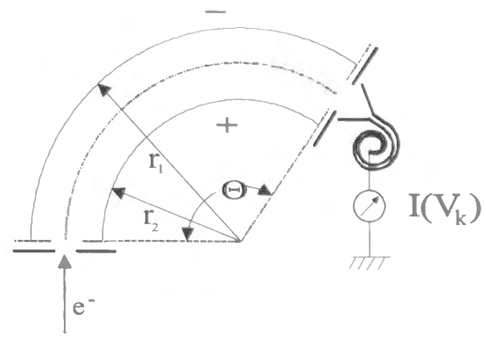

Figure 1-7. Schematic cross section of the cylindrical analyzer.

For fixed values of r_1 and r_2, the electron energy distribution can be recorded by varying V_k. The resolution is mainly determined by the widths of the entrance and exit slits. The sector angle θ is set to obtain the optimum directional focussing. By using a sensitive electron multiplier as a detector the slits can be made very narrow, which provides very high resolution in the electron spectroscopy. This analyzer is constructed on a movable turntable for studies on angle-resolved electron energy distributions [13].

Resolutions of the photoelectron analyzer used in this study are 1.05 eV at an analyzer energy of 10 eV which was used in UPS measurements, and 1.2 eV at an analyzer energy of 20 eV which was used in XPS measurements.

Sample

GaAs(100) wafers (undope-type) were purchased from Mitsubishi Chemical Co. Their physical properties are shown in table 1-3. The wafers were processed with chemical cleaning before they were placed into the vacuum chamber. In the chemical cleaning process a GaAs substrate was steeped in boiled acetone

Table 1-3. The physical properties of GaAs substrates (Ref. 15)

parameters	value
Density, ρ (g/cm^3)	5.32
specific heat, C (J/g K)	0.35
heat capacity per unit volume, ρC (J/cm^3 K)	1.86
thermal conductivity, K (W/cm K)	0.46
thermal diffusivity, β (cm^2/sec)	0.247

for 10 minutes, and washed with a supersonic machine in acetone, methanol, and distilled water for 5 min, respectively. Then, after steeping in conc. HCl solution and blowing with N_2 gas, the sample was placed into the vacuum chamber within 10 min and pumped to UHV.

The sample surface was irradiated in the UHV condition with Ar^+ bombardment (1.5 kV, 15 minutes) and annealed at 570℃ for 20 minutes. After these procedures, the GaAs surface was clean enough to detect neither carbon nor oxygen in XPS spectrum, which should be reconstructed to Ga-rich c(8×2) LEED.[14]

The etching was introduced into the UHV chamber through the tube shown schematically in Fig. 1-6.

Lasers

For the photoirradiation experiments, an ArF (193 nm) and KrF(248 nm) pulsed excimer laser, the second (532 nm), third (355 nm) and fourth (266 nm) harmonics of a pulsed YAG laser, and cw Ar^+ laser (488 nm) were used.

The conditions of the lasers for the photoirradiation experiments are summarized in table 1-4.

Table 1-4. Experimental conditions of the lasers used in the photoirradiation experiments

parameters	ArF	KrF	YAG-FH	YAG-TH	YAG-SH	Ar^+
wavelength (nm)	193	248	266	355	532	488
pulse or cw	pulse	pulse	pulse	pulse	pulse	cw
power density (mJ/cm^2)	1.6	3.2	9.0	11.3	11.3	60
pulse width (ns)	16	16	4.5	5.5	6.5	-
repetition rate (Hz)	10	10	10	10	10	-

References

[1] A. Einstein, Ann. Phys. Leipzig. **17**, 132 (1905).

[2] J. Jenkin, J. Elect. Spect. **23**, 187 (1981).

[3] K. Siegbahn, U. Gelius, H. Siegbahn, and E. Olsen, Phys. Lett. **32A**, 221 (1970).

[4] C. S. Fadley and S. A. L. Bergstrom, Phys. Lett. **35A**, 375 (1971); and in *Electron Spectroscopy*, D. A. Shirley, ed., North Holland, Amsterdam (1972), p.233.

[5] C. S. Fadley, R. J. Baird, W. Siekhaus, T. Novakov, and S. A. L. Bergstrom, review in J. Elect. Spect. **4**, 93 (1974).

[6] C. S. Fadley, Prog. in Sol. St. Chem. **11**, 265 (1976).

[7] C. S. Fadley, *Electron Spectroscopy: Theory, Techniques, and Applications* **2**, ch.1 (1978).

[8] A. Dilks, *Electron Spectroscopy: Theory, Techniques and Applications* **4**, (1981).

[9] J. M. Hill, D. G. Royce, C. S. Fadley, L. F. Wagner, and F. J. Grunthaner, Chem. Phys. Lett. **44**, 225 (1976)

[10] C. D. Wagner, W. M. Riggs, L. E. Davis, J. F. Moulder, and G. E Muilenberg, *Handbook of X-ray Photoelectron Spectroscopy*, (1979).

[11] J. A. R. Samson, *Technique of Vacuum Ultraviolet Spectroscopy*, (1967).

[12] A. L. Hughes and V. Rojansky, Phys. Rev. **34**, 284 (1929).

[13] H. F. Kempin, K. Klapper and G. Ertl, Rev. Sci. Instr. **49**, 1285 (1978).

[14] A. Ludviksson, M. D. Xu and R. M. Martin, Surf. Sci. **277**, 282 (1992).

[15] S. M. Sze, *Physics of Semiconductor Devices*, 850 (1981).

1.3 Results

1.3.1 Absorption states of etchant gas

HCl

Figure 1-8 shows angle resolved XPS spectra of GaAs(100) substrate at θ=75, 45 and 10° with a HCl adsorbate layer (6 L) at temperature of -100℃, in which Cl2p and As3s signals are assigned. At θ=75° the Cl2p peak is not discernible. With decreasing θ the Cl2p peak intensity relatively increases, while the As3s peak intensity decreases. These results indicate that Cl atoms are present on the top surface. At -100℃ HCl adsorbs dissociatively on the GaAs surface, that is, chemisorbs on GaAs.

The XPS signal intensities of the Cl2p and As3s peaks were monitored as a function of HCl exposure up to 4.5 L at -100℃, where As3s peak was used as an internal reference signal. The results are shown in Fig. 1-9, in which the peak intensity ratios, I(Cl2p)/I(As3s), are corrected to population ratios [Cl]/[As] with the atomic sensitivity factors. The ratios approach an asymptotic value at the high exposure region due to saturation effect on the adsorption process.

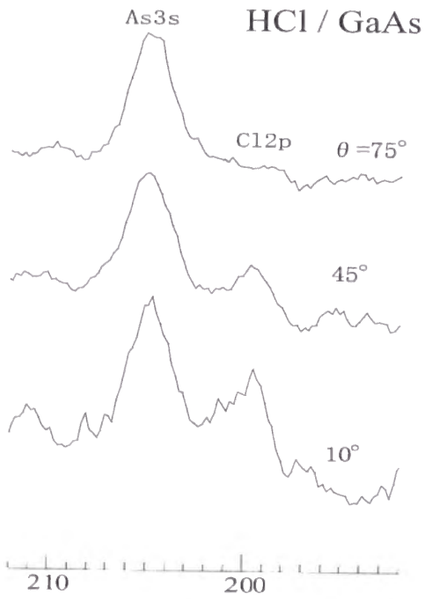

Figure 1-8. Angle-resolved XPS spectra after exposing with HCl (6 L) at -100℃.

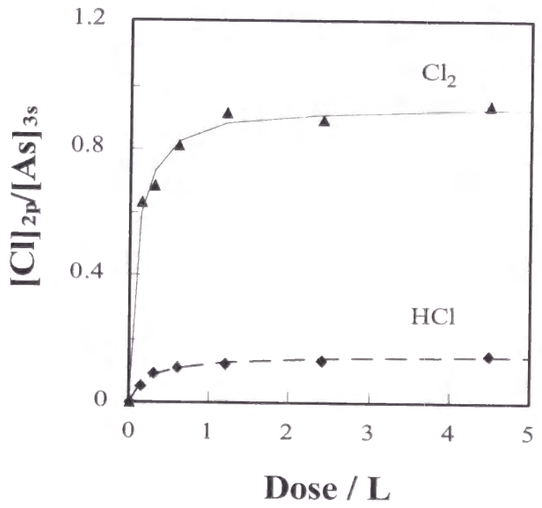

Figure 1-9 Surface population ratios of $[Cl]_{2p}/[As]_{3s}$ monitored by XPS as a function of exposure of HCl and Cl_2 on GaAs substrates at -100℃. XPS peak intensities are measured at Cl2p and As 3s peaks.

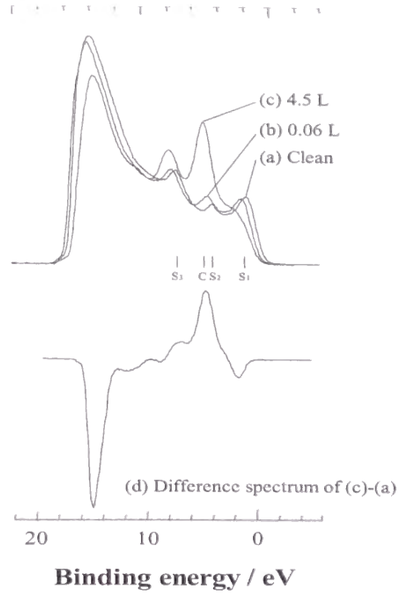

Figure 1-10. UPS spectra changes as a function of exposure of HCl at substrate temperature -100 ℃.

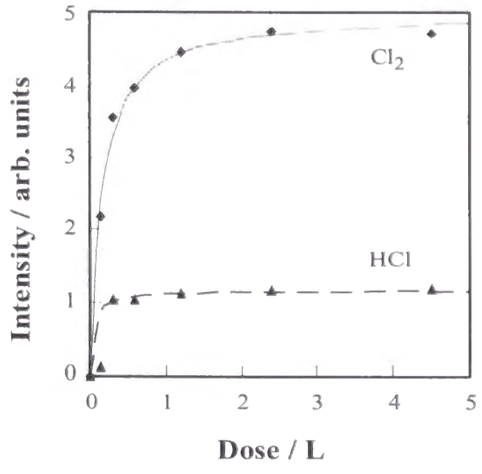

Figure 1-11. UPS peak intensity change at 5 eV as a function of exposure with Cl_2 and HCl on GaAs substrates at -100℃.

Figure 1-10 (upper) shows the UPS spectral change as a function of HCl exposure up to 4.5 L. For the clean substrate, three valence-band-related peaks, S_1, S_2 and S_3 are clearly resolved. The UPS spectrum at 4.5 L is quite different from the gas-phase one reported by Kimura *et al.*[1], which suggests that no parent HCl physisorbs on the GaAs surface. Troost *et al.* [2] assigned S_1, S_2 and S_3 as substrate valence peaks, and C as a chemisorbed peak of the bond between Ga (or As) and the Cl atoms. During the HCl exposure, these three peaks were shifted to higher binding energies until 0.3 L exposure or near the saturated condition. With the HCl exposure intensity of peak C at 5.1 eV increases and reaches an asymptotic value due to chemisorption of HCl. The observed chemical shifts of S_1, S_2 and S_3 are due to the surface band bending caused by adsorption of Cl atoms on the GaAs surface. The lower part of Fig. 1-10 shows an UPS difference spectrum. Peak C at 5.1 eV has a full-width-at-half-maximum (FWHM) of 1.5 eV. The dip at 14.5 eV is due to the decrease of the secondary electrons in the substrate.

Fig. 1-11 shows peak area change of the chemisorbed peak C as a function of HCl exposure. The peak intensity approaches an asymptotic value at the high exposure region due to the saturation effect. In this figure, the broken curve represents a fitting equation for chemisorption on

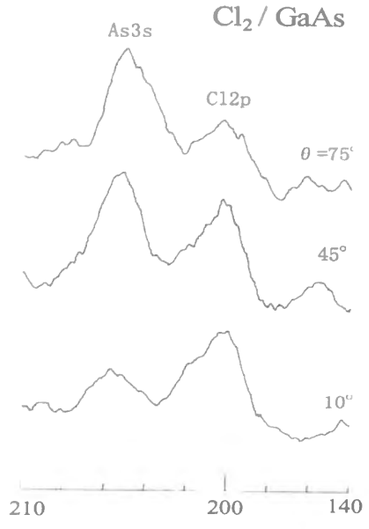

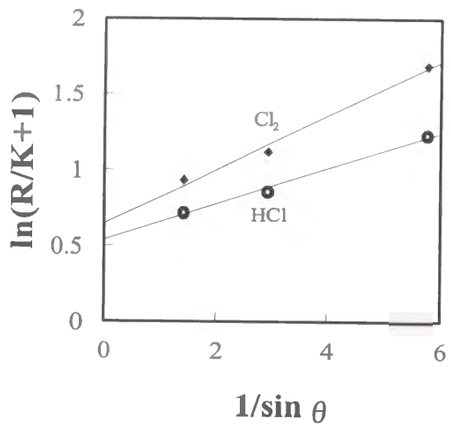

Figure 1-13. ln (R(θ)/K+1) of Eq. 3-1 plotted versus 1/sinθ, which obtained in the ARXPS measurements atθ= 10° , 25° and 45° for HCl (6 L) and Cl₂ (0.6 L).

Figure 1-12. Angle-resolved XPS spectra after exposing with Cl_2 (0.6 L) at -100 ℃.

active sites of a surface according to Chakravarti and Dhar [3],

$$v = \frac{kP^{1/n}}{b + P^{1/n}} \qquad (1\text{-}14)$$

where v is an amount of adsorbate, k and n are constants. P is a degree of exposure. In this experiment, P is taken as the dose rate, n is unity. Thus, Eq. 1-14 equals Langmuir adsorption isotherm.

Cl_2

Figure 1-12 shows examples of ARXPS spectra of GaAs(100) at θ=75°, 45°and 10° at substrate temperature of -100℃ with a Cl_2 adsorbate layer, in which Cl2p and As3s signals are indicated. At θ=75° the Cl2p peak is well recognized. With decreasing θ the intensity of Cl2p peak increases, while the As3s peak intensity decreases. These results suggest that the Cl species form overlayers on the GaAs substrate. According to Fadley[4], signal intensity ratios between overlayer and substrate are given by,

$$\ln\left[\frac{R(\theta)}{K} + 1\right] = \frac{d}{\Lambda_e \sin\theta}, \qquad (1\text{-}15)$$

where R(θ) is the overlayer/substrate ratio at θ, K is defined as a ratio of Cl_2 absolute signal intensity of the overlayer to that of the substrate without the overlayer, d is a thickness of the uniform overlayer. From the data in Fig. 1-13 and Eq. 1-15, the overlayer thickness d is estimated to be 0.45 nm for Cl_2 (0.6 L) and 0.29 nm for HCl (6 L).

The XPS signal intensity of the Cl2p and As3s peaks were monitored as a function of Cl_2 exposure up to 4.5 L at -100℃, where As3s peak was used as a reference. The population ratios $[Cl]_{2p}/[As]_{3s}$ for Cl and As are shown in Fig. 1-9. The ratio approaches an asymptotic value at the high exposure region due to the saturation effect. The asymptotic value for Cl_2 is about six times larger than that for HCl. This result indicates that Cl atoms are highly concentrated near the surface in the case of Cl_2 exposure.

Figure 1-14 shows the UPS spectra change as a function of Cl_2 exposure up to 4.5 L. During the Cl_2 exposure up to at 0.6 L, three peaks S_1, S_2 and S_3 were shifted to higher binding energy. With Cl_2 exposure the intensity of the chemisorbed peak C at 4.9 eV increases and reaches an asymptotic value due

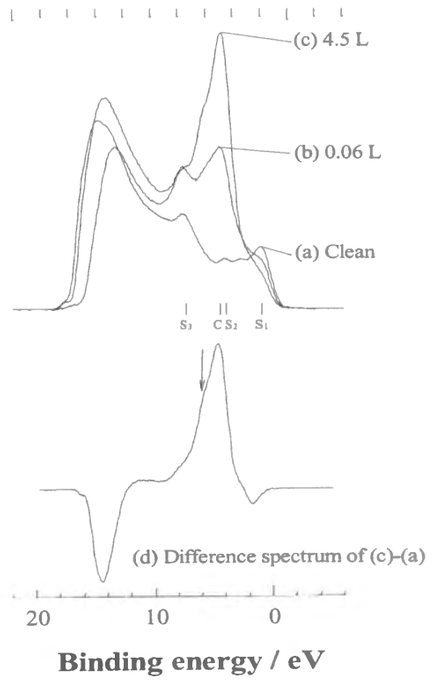

Figure 1-14. UPS spectra change as a function of exposure of Cl_2 at substrate temperature -100 ℃.

to the chemisorption of Cl_2. In Fig. 1-14, the difference spectrum is also shown. The peak C has an FWHM of 2.4 eV for the exposure, which is larger than that (1.5 eV) for the HCl exposure.

Fig. 1-11 shows the peak area change of the chemisorbed peak C as a function of Cl_2 exposure. The peak intensity approaches an asymptotic value at the high exposure region due to the saturation effect. Similar results are obtained in the XPS spectra with HCl exposure of the GaAs as shown in Fig. 1-9. The asymptotic value for Cl_2 is about four times larger than that for HCl. Based on our UPS and XPS measurements (Figs. 1-9 and 1-11), Cl_2 chemisorbs on the GaAs substrate (5±1) times more than HCl.

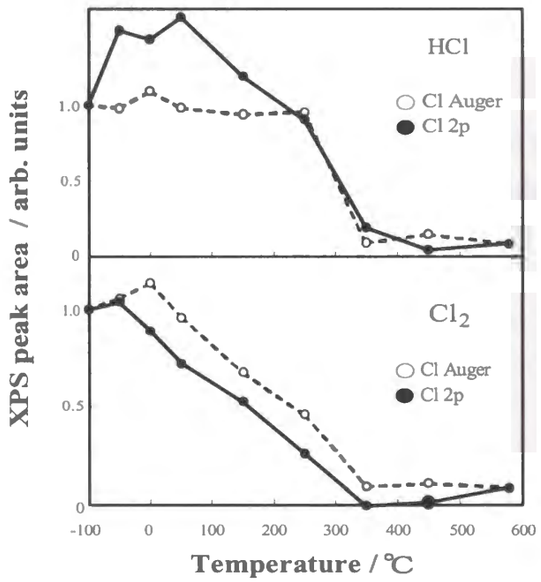

Figure 1-15. XPS intensity change as a function of substra temperature after exposing with HCl and Cl_2 at 2×10^{-8} Torr for 5 min at -100℃.

1.3.2 Thermal effect

HCl

Fig. 1-15 (upper) shows the temperature effect on the XPS peak intensity for the Cl2p and Cl Auger transition after HCl(5.5 L) exposure at -100℃. The Cl2p peak became weak at 100℃ and disappeared at 350℃. For 150 - 250℃,

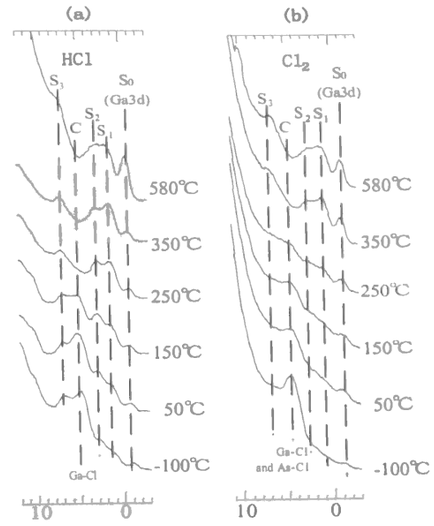

Figure 1-16. Thermal effects on the UPS spectra after GaAs surface is exposed with HCl (6 L) or Cl_2 (0.6 L) at -100 ℃.

Cl-containing species were produced, and then these species desorbed from the surface above 250℃.

UPS spectra at -100℃ in Fig. 1-16a reflect the surface valence states just after exposure with HCl. The four peaks appear, namely, S_0, S_1, C and S_3. When the substrate temperature was increased to 150 - 250℃, the spectral change becomes apparent as shown in Fig 1-16a. Above 250℃ the peak C disappear, S_0 grew larger, and S_2 reappeared, because the GaAs surface was cleaned due to the thermal desorption of the surface species. The S_0 peak is assigned to the Ga3d core state by He II UPS. The similar temperature behavior was observed by XPS and Auger spectra as shown in Fig. 1-15.

Cl_2

Fig. 1-15 (lower) shows the change in the XPS peak area for the Cl2p and Cl Auger transition as a function of substrate temperature, followed by exposure of the GaAs surface up to 5.5 L of Cl_2 at -100℃. Decrease in the Cl2p peak was observed at -50℃ and its intensity was almost lost at 350℃. This

suggests that, etching reactions take place, and then Cl-containing species desorb from the surface in the temperature range of -50℃-350℃.

The UPS spectrum at -100℃ in Fig. 1-16b reflects the surface valence states just after the exposure with Cl_2 (0.6 L). The peak C is observed but the valence-band-related S_0, S_1, S_2 and S_3 are negligible. This spectrum indicates that the surface of the GaAs substrate is covered with Cl atoms completely, and there is no bared surface under this condition. When the substrate temperature was increased to 350 ℃, the chemisorption-induced peak C decreased gradually as shown in Fig 1-16b. Above 350℃ the peak C disappears, and the valence-band-related peaks, S_0-S_3, reappears. which indicates that thermal etching reactions take place and the surface is cleaned. Intensity changes of the Cl XPS and Auger peaks are also observed as shown in Fig. 1-15.

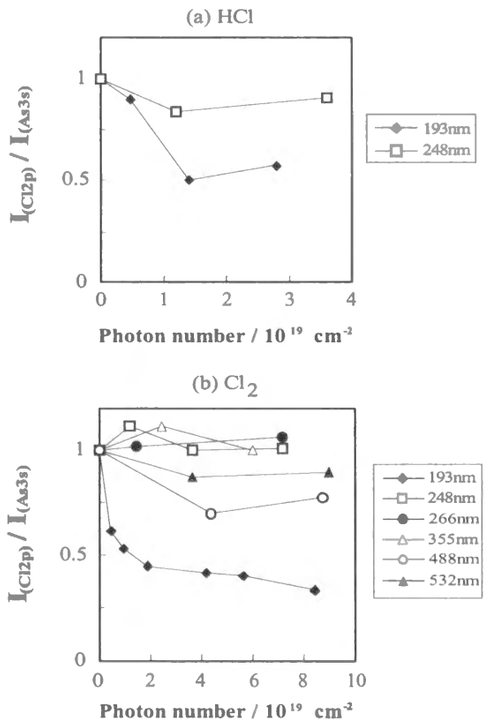

Figure 3-17. Photoirradiation effect for dry etching on I (Cl2p) / I (As3s) in 193 - 532 nm. The laser intensity is 4 mJ/cm ². Initial values for I (Cl2p) / I (As3s) are normalized as unity.

1.3.3 Photoirradiation effect

Figure 1-17 shows the photoirradiation effects on the XPS signal intensities for the GaAs substrates with HCl and Cl_2, using an excimer pulsed laser at 193 nm. Before the laser irradiation, GaAs substrates were exposed with either 0.6 L Cl_2 or 6 L HCl at -100℃, and then heated to 25℃. The XPS intensity ratios of I(Cl2p)/I(As3s) are plotted versus laser photon numbers in Fig. 1-17. The ratios decreased with the photoirradiation of 193 nm. The 248 nm irradiation showed almost no effect on the I(Cl2p)/I(As3s) ratios.

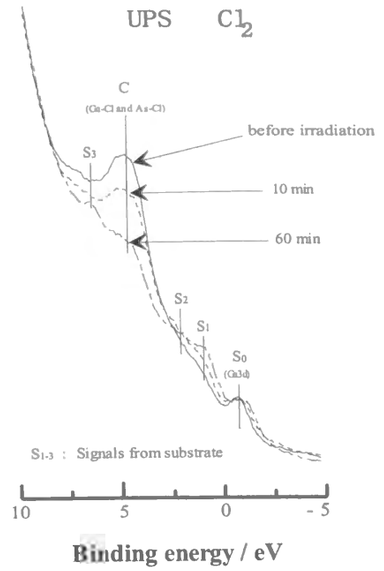

Figure 3-18. 193 nm photoirradiation effects on the UPS of GaAs substrate at 25℃ which is exposed with Cl_2 0.6 L (at -100℃)

After exposure with Cl_2 gas (0.6 L) the GaAs substrates was irradiated with 193 nm laser light, UPS spectra were measured at various photoirradiation times. The spectral change between before and after the irradiation of 193 nm is shown in Fig. 1-18. The intensity of the peak C decreased with the 193 nm laser photoirradiation, while those of Peak S_1, S_2 and S_3 increased. These results indicate that the desorption of Cl atoms or Cl-containing species takes place and bare surface GaAs reappears with the photoirradiation.

The effects of the photoirradiation at 266, 355 and 532 nm were also examined after the Cl_2 exposure, using a pulsed YAG laser. However, no obvious change was observed in the XPS spectra as shown in Fig. 1-17 (lower). The effect of photoirradiation at 488 nm was also examined after the Cl_2 exposure, using a c/w Ar^+ laser. A slight change was observed in the XPS spectra as shown in Fig. 1-17 (lower).

References

[1] K. Kimura, S. Katsumata, Y. Achiba, T. Yamazaki and S. Iwata, Handbook of He I photoelectron spectra of fundamental organic molecules, 29 (1981).

[2] D. Troost, L. Koenders, L.-Y. Fan and W. Mönch, J. Vac. Sci. Technol. **B 5**, 1119 (1987).

[3] D. N. Chakravarti, N. R. Dhar, Kolloid. Z. **43**, 377 (1927).

[4] C. S. Fadley, Progress in Surface Science **16**, 275 (1984).

1.4 Discussion

1.4.1 Comparison of initial conditions

Figures 1-9 and 1-11 indicate that Cl_2 is adsorbed on the GaAs substrate about five times more than HCl. From the data in Fig. 1-13 and Eq. 1-15, the thickness of the Cl overlayer for Cl_2 is estimated to be 4.5Å, while that for HCl is estimated to be 2.9Å These values correspond to roughly one monolayer, because the bonding length of GaAs is 2.7Å. Since both the overlayer thickness values of HCl and Cl_2 on the surface are less than two monolayer, HCl and Cl_2 do not form multilayers on the GaAs at -100℃. In UPS spectra, the peak C for Cl_2 in Fig. 1-14 has a larger FWHM than that for HCl in Fig. 1-10, probably because the peak C consists of two or three components. The main peak is located at 4.9 eV, and a shoulder peak (shown by an arrow in the figure) is recognized at the higher binding energy side. According to UPS measurement reported by Grabandt *et al.*[1], GaCl has a peak at 10.07 eV, and $GaCl_3$ at 12.3 eV in the gas phase. Since the work function of our spectrometer is 5.0 eV, the main peaks of GaCl and $GaCl_3$ in solid phase should appear at 5.1 eV and 7.3 eV, respectively. Thus, the shoulder component of the peak C in Fig. 1-14 may attribute to $GaCl_3$ or $GaCl_2$.

Nooney et al. [2] studied the adsorption of HCl on an undoped GaAs surface using high-resolution electron energy loss spectroscopy. They suggested that HCl molecules dissociate at the Ga dimmer vacancies and then

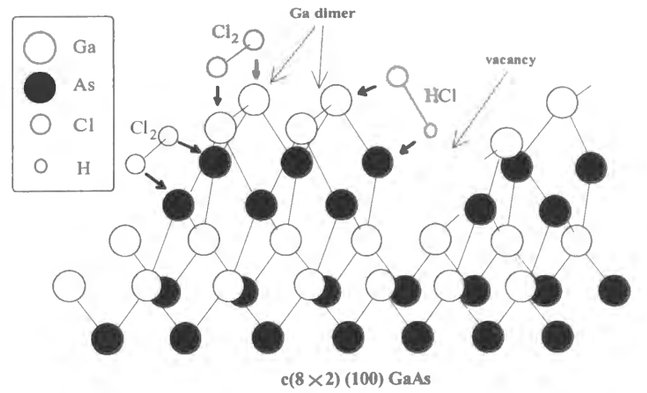

Figure 1-19. Proposed mechanism for dissociative chemsorption of HCl and Cl_2 on Ga-rich (100) GaAs reconstracted surface from reference of Nooney et al (ref. 2).

add across Ga-As backbonds with H bonding to the As, and Cl bonding to the Ga. This chemisorption mechanism is schematically shown in Fig. 1-19.

As described above, Cl_2 chemisorbs and forms $GaCl_x$ and $AsCl_x$ (x=1, 2, 3) on the GaAs surface, while HCl chemisorbs at the Ga dimmer vacancies and forms GaCl and AsH on the surface. Thus, the amount of Cl_2 chemisorbed on the GaAs surface is five times larger than that of HCl. The mechanism for the dissociative chemisorption of Cl_2 is schematically shown in Fig. 1-19.

1.4.2 Thermal effect

Cl_2

Fig. 1-16b shows the results of UPS measurements for the etching of GaAs by Cl_2. In the spectrum which was measured just after exposure with Cl_2 at -100℃, the GaAs substrate peaks (S_0, S_1, S_2, S_3) were not almost discernible, but only the peak C was observed. This spectrum indicates that the GaAs substrate surface is covered with Cl-containing species completely, and that there is no bare surface of the substrate Ga and As atoms under this condition.

With increase of the substrate temperature, the peak C intensity decreased gradually for 50 - 100℃ and rapidly decreased for 250 - 350℃. This behavior agrees with the results of XPS measurements (Fig. 1-15). The decrease of the peak C intensity may correspond to the disappearance of the Ga-Cl and As-Cl bonds on the surface by the desorption of Cl-containing species. Above 350℃, the peaks S_1, S_2 ,S_3 and S_0 (Ga3d peak) reappeared. These changes were also observed in the UPS spectra for the HCl etching. The spectrum at 250℃ for Cl_2 was quite different from that for HCl. In the UPS spectrum for the Cl_2 etching, no structure appeared at 250℃. This may be due to the disruption of the surface order by the excess etching reactions on the surface with Cl_2. The fact that the XPS peak of As3s at θ=10° shows a chemical shift toward higher binding energy indicates that the As-Cl bond is formed on the surface. French et al. [3] suggested that Cl_2 had no selectivity for the adsorption site, and the initial adsorption of Cl_2 might occur on the top Ga atoms (Fig. 1-13), forming GaCl. Actually, they observed the desorption of GaCl at about 270℃. Using their TPD technique, French et al. [3] reported that there were two steps of Cl desorption from the GaAs: the first step was the desorption

of $GaCl_3$ and recombination of Cl_2 in the temperature range of 0 - 150℃. The second step was the desorption of GaCl in the range of 250 - 350℃. French et al.[3] also reported that extra Cl_2 molecules formed a non-homogeneous overlayer on the GaAs surface and that $GaCl_3$ and $AsCl_3$ molecules desorbed as the etching products. Then, the surface was disrupted after desorbing of $GaCl_3$ and $AsCl_3$. Our XPS and UPS results agree well with their results. Since Cl-containing species with increasing substrate temperature, the GaAs surface is disrupted. The extensive etching by Cl_2 proceeds with the desorption of $GaCl_3$ at low temperatures (0 - 150℃) and the clean, reconstructed GaAs c(8×2) surface are observed at 350℃.

HCl

In the case of HCl etching, Ga-Cl and As-H bonds are formed on the surface, and then H_2 and GaCl molecules desorb thermally from the surface. Therefore, the ordered structure of the GaAs surface is maintained. The UPS spectrum at 250℃ in Fig. 1-16a shows the weak S_0 (Ga3d) peak and indicates the structured surface. These results suggest that the GaAs(100) As-rich (2×8)

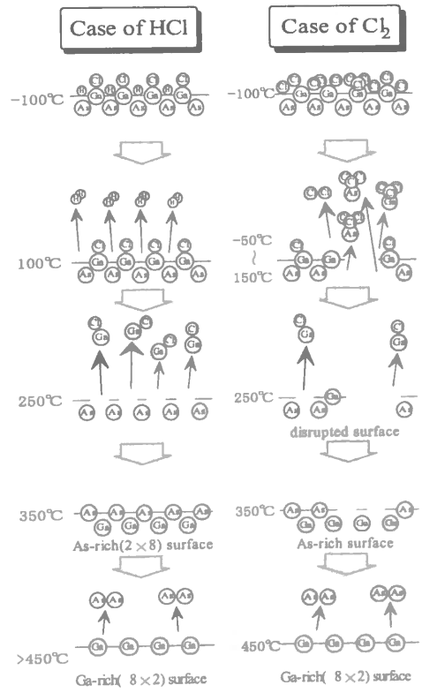

Figure 1-20. Schematic drawings of etching reactions.

surface is hold at 250℃.

In the TPD studies reported by Nooney et al.[2] and French et al.[3], they found that desorption of H_2 at 100℃ and that of GaCl at 270℃, while $GaCl_3$, recombined Cl_2, GaCl and As_2 were observed to desorb at 100℃, 350℃ and 400℃, respectively in the Cl_2/GaAs system. Base on their and our results, the dry etching mechanism is proposed as shown schematically in Fig. 1-20. The desorption process can change dramatically by amount of Cl_2 adsorption in the Cl_2/GaAs system. The mechanism for the Cl_2 reaction in Fig. 1-20 corresponds to the case when Cl atoms adsorbed excessively on the GaAs surface.

From the obtained results, the following facts are revealed.

i) Cl_2 molecules are chemisorbed at -100℃ on GaAs.

ii) HCl molecules are chemisorbed on the GaAs surface and the surface is covered with Ga-Cl and As-H bonds, no more adsorption of HCl takes place on the surface.

iii) Cl_2 molecules are chemisorbed on the GaAs surface and the surface is covered with $GaCl_X$ and $AsCl_X$ (x=1, 2, 3).

1.4.3 Photoirradiation effect

This section reviews the photoexcitation pathways of surface reactions, focusing on photon-surface interactions. When the surface is irradiated by light as shown in Fig. 1-21, at least three conceptually different bond-breaking pathways initiated by the photon absorption can operate, separately or in concert: (1) direct excitation, the light is absorbed within the adsorbate or an adsorbate-substrate complex and leads to non-thermal chemical changes; (2) substrate excitation, the photon absorption

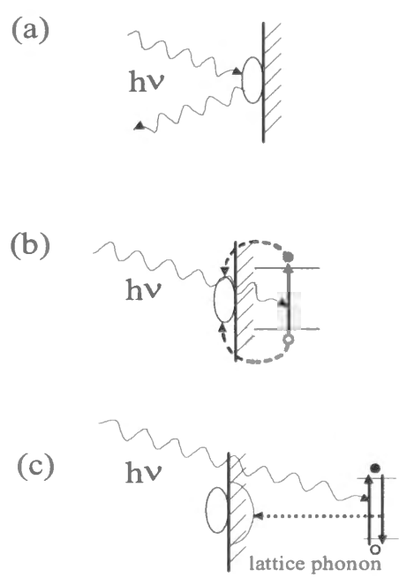

Figure 1-21. Excitation pathways caused by photoirradiation; (a) direct excitation, (b) substrate excitation, and (c) thermal excitation.

occurs in the substrate and the resulting excited electrons or holes induce non-thermal adsorbate chemistry; and (3) thermal excitation, relaxation and randomization of the initial excitation energy results in surface heating and causes thermal chemistry. Varying the wavelength of the incident light can help in resolving these three different pathways. For a molecule that has gaseous photoabsorption only at short wavelength, the photoirradiation at short wavelength induced direct excitation of adsorbed molecule and substrate. Photoirradiation at long wavelength induced the substrate excitation.

Direct excitation

If the initial excitation takes place strictly within the adsorbates (i.e., author can neglect the influence of the substrate on both the initial and final states) the wavelength response should follow that of the gas-phase or condensed-phase adsorbate molecule.

Transitions involving these levels are broadened by as little as 0.1 eV and as much as 1 eV [4-8] and are shifted, both blue-shifted and red-shifted, from their gas-phase energies.

Substrate excitation

One of the important aspects of photochemistry at adsorbate/metal interfaces is the possibility that the incident photons indirectly drive the surface chemistry; the photon absorbs in the metal, exciting electrons and holes which, after transport, promote chemical events at the surface. Increasingly, evidence has accumulated which demonstrates the importance of hot electrons and holes in surface photochemistry.

Author considers the substrate-mediated surface photochemical process as comprised of three distinct and separable (in time) steps:

(a) The optical excitation of electrons in the bulk substrate.

(b) The migration of excited electrons and holes to through the crystal lattices to the surface.

(c) The attachment of these excited electrons or holes to the adsorbate to form an excited state. The first two are identical to the photoemission model, while the last step in photoemission, the escape of electrons from the surface field, is replaced here by the attachment of excited electrons or holes to the adsorbate.

Thermal excitation

What happens to those hot carriers that either do not arrive at the surface or do not attach to the adsorbate-substrate complex ? Those with sufficient energy may be transmitted through the interface (photoemitted); those are not photoemitted will eventually be thermalized and the temperature in the region will increase. Since the UV photon penetration depth in most metals is on the order of 10^{-6} to 10^{-5} cm (several hundred Å) and scattering lengths are slightly shorter (10^{-6} cm), the majority of the created hot carriers will not reach the surface without undergoing inelastic scattering. In a complicated, and so far poorly understood, many-body scattering process, the energy in the nascent electrons (holes) will be lost through electron-electron (hole-electron) collision, electron-plasmon collisions, electron-hole recombination associated with Auger processes, and electron-phonon collisions. After 10^{-12} s, the excitation energy is ultimately shared with the atoms in the solid and is transformed into lattice photons (heat).[9] Since thermal activation generally leads to chemistry, it is important to determine the extent to which thermal effects contribute to the observed photon-driven chemistry.

If a surface photochemical process is the result of surface heating, its rate is then a function of the energy deposited into the substrate. The only wavelength requirement, and one easily met throughout the visible and ultraviolet region, is absorption by the substrate.

Thermal consequence of the pulsed or cw laser irradiation has been discussed by Yardley [10] and Osmundsen *et al.*[11].

According to them, the temperature raised by the pulsed laser light is given by the following equation:

$$\Delta T(\tau) = \frac{2\alpha I_m (1-R)}{K} \frac{(\beta\tau)^{1/2}}{\pi^{1/2}}, \qquad (1\text{-}16)$$

where I_m is the peak power intensity of a laser pulse, α is the fraction of the radiation passing through the substrate that is adsorbed, R is the surface reflectivity at the laser wavelength, and K is the thermal conductivity. $2\alpha I_m (1 - R)$ means the intensity adsorbed at the surface, The thermal diffusivity β is defined by:

$$\beta = \frac{K}{\rho C}, \qquad (1\text{-}17)$$

Table 1-5. Substrate temperature increases by photoirradiation.

wavelength (nm)	Peak laser power Im (W/cm^2)	α	R	τ (s)	ΔT (K)	T_s (K)
		GaAs (173 K)				
193	1.0×10^5	1	0.48	1.6×10^{-8}	8.0	181
248	2.0×10^5	1	0.61	1.6×10^{-8}	12	185
266	2.0×10^6	1	0.53	4.5×10^{-9}	76	250
355	2.1×10^6		0.42	5.5×10^{-9}	107	281
488	6.0×10^2	1	0.43	cw laser (3600)	2.5	176
532	1.7×10^6	1	0.39	6.5×10^{-9}	104	277

where ρ is the substrate density, and C is the specific heat.

The temperature raised by the cw laser light is given by the following:

$$\Delta T(t) = \frac{2\alpha I (1-R)}{K} \frac{(\beta t)^{1/2}}{\pi^{1/2}}. \qquad (1\text{-}18)$$

where I is the cw laser

The substrate temperatures of GaAs substrate under our experimental condition are summarized in Table 1-5. Parameters, used this calculation for Eq. 1-16 and 1-18, are summarized in Table 1-3.

Desorption mechanisms of etching products

The results obtained in this photochemical experiment indicate that photochemical reaction is induced strongly at 193 nm with a pulsed excimer laser. The mechanism of the desorption induced by the 193 nm photoirradiation is considered as follows:

In absorption of these wavelength photons, the photoirradiation effects are classified into three processes as shown in Fig. 1-21:

(a) the direct photoabsorption of adsorbed species on a surface due to its electronic transition,

(b) photoabsorption by the substrate, followed by desorption of adsorbed species with energy release due to the recombination of hole and electron,

(c) photoabsorption of substrate followed by thermal desorption due to relaxation of excited lattice phonon.

193, 248 and 355 nm photons may be absorbed by the substrate. Figure 1-22 shows absorption spectra of GaAs substrate. The solid line in Fig. 1-22 upper indicates the absorption coefficient. If the substrate absorbs the photon near the surface, the carrier will be produced, e.g. exciton, hole and electron, that described before. They move and recombined in a certain lifetime, ~ 10^{-15} s [12][13][14]. At that time, the recombination energy is released. Therefore, Since the region which the recombination energy can be transferred from the origin point to the adsorbate is only several 10 MLs on the top of a surface. The absorption of this region is calculated by following equation and the reflectance shown in Fig. 1-21 lower (dotted line):

$$\xi(\lambda) = (1-R)\{1-\exp(-\alpha d)\}, \qquad (1\text{-}19)$$

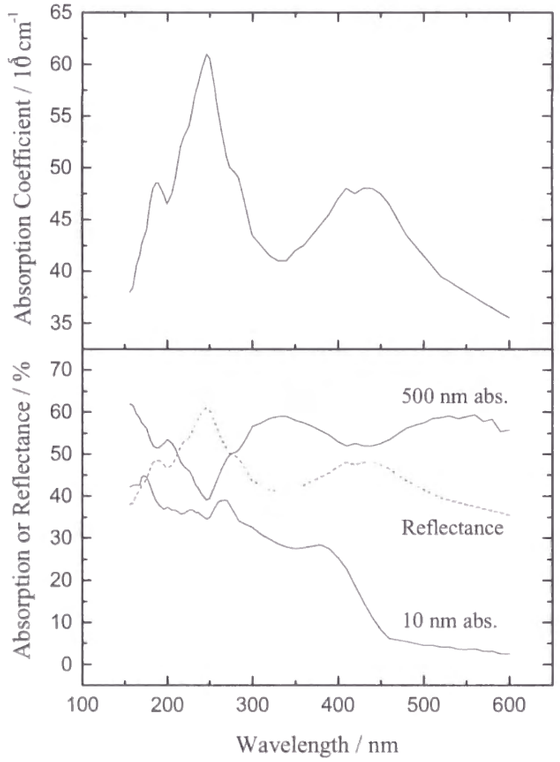

Fig. 1-21. Absorption spectra of GaAs. Upper indicates the absorption coefficient. Lower indicates the reflectance (dotted line), the absorption of 10 nm GaAs layer (lower solid line) and 500 nm GaAs layer (upper solid line).

where α is the absorption coefficient, R is the reflectance, d is the thickness of the layer, λ is the wavelength of the incident photon and ξ is the absorption of the layer. The calculated results are shown in Fig. 1-21 lower. The upper solid line indicates the absorption of the 500 nm thickness layer, and the lower solid line indicates the absorption of the 10 nm thickness layer. Considering the 10 nm thickness layer's results, the absorption of the 193, 248 and 355 nm is almost same value. Therefore, the substrate mediated indirect-excitation is not different among these wavelengths. However, It does not correspond to the experimental results. In the next, the thermal desorption process caused by the temperature increase due to the laser irradiation is considered. The estimated temperature increases of the substrate, induced by the various photoirradiation in this experiment, are shown in Table 1-5. The calculated results of 193, 248 and 488 nm in the table indicate the thermal effect is negligible, since the temperature increases are lesser than 12 K. The cw laser induced temperature increase is also very small (2.5 K). Meanwhile the temperature increase induced by the photoirradiation of 266, 355 and 532 nm are extremely high. The thermal excitation process can not be negligible in the case of these photoirradiations, since at the reached temperature some etching products have to be desorbed from the surface apparently, according to the Fig. 1-15. However, photoirradiation experimental results in Fig. 1-17 are not corresponding to this results, suggesting that the thermal desorption of the products which is induced by the pulsed laser is inefficient because the induced temperature raise is tentative and the reached temperature is not enough for products to desorb immediately. Actually the thermostatic substrate temperature during the photoirradiation indicates only a little increase, ~10 K. It is considered that since the thermal desorption can be happen at every laser pulse duration (~5 ns) and the laser repetition rate is 10 Hz, the desorption rate observed experimentally will be extremely slow. That is the reason why the thermal effect at 266, 355 and 532 nm was not observed. The fact that the desorption was observed only by the 193 nm laser irradiation indicates that the process(a) must occurs by the photoirradiation at 193 nm while the substrate excitation with the pulsed laser does not induce the etching reaction at the other wavelengths.

With the cw irradiation of 488 nm light, slow etching process was observed as shown in Fig. 1-17. This photoirradiation effect is not due to a "direct" photoabsorption process (case (a)) but due to the case (b). The cw irradiation induces carriers near the GaAs surface efficiently, that recombine on the surface to generate energy and break bonds of the surface species.

References

[1] O. Grabandt, R. Mooyman, C. A. Delange, Chem. Phys. **143**, 227 (1990).

[2] M. Nooney, V. Liberman, M. Xu, A. Ludviksson and R. M. Martin, Surf. Sci. **302**, 192 (1994).

[3] C. L. French, W. S. Balch and J. S. Foord, J. Phys. Condensed. Matter **3**, S351 (1991).

[4] Ph. Avouris and R. E. Walkup, Annu. Rev. Phys. Chem. **40**, 173 (1989).

[5] B. Feuerbacher, B. Fitton and R. F. Willis, *Photoemission and the Electronic Properties of Surface*, (1978).

[6] J. W. Gadzuk, Annu. Rev. Phys. Chem. **39**, 395 (1988).

[7] P. Nordlander and J. C. Tully, Phys. Rev. Lett. **61**, 990 (1988); P. Nordlander, :*Desorption Induced by Electronic Transitions - DIEV IV*, 2 (1990).

[8] P. D. Johnson, A. J. Viescans, P. Nordlander and J. C. Tully, Phys. Rev. Lett, **64**, 942 (1990).

[9] G. L. Eesley, Phys. Rev. Lett. **51**, 2140 (1983).

[10] J. T. Yardley, *Laser chemistry: processing at the micro level*, *Laser Handbook*, 405 (1985).

[11] J. F. Osmundsen, C. C. Abele and J. G. Edsen, J. Appl. Phys. **57**, 2921 (1985).

[12] P. A. Wolff., Phys. Rev., **95**, 56 (1954).

[13] J. J. Quinn, Phys. Rev., **126**, 1453 (1962).

[14] J. J. Quinn, Bull. Am. Phys. Soc., **7**, 27 (1962).

1.5 Conclusion

Author have investigated the thermal dry etching reaction mechanism of Cl_2 and HCl on GaAs(100) surface, and photoirradiated effect at UV - VIS region. The following facts on the etching and photodesorption processes were obtained from our experimental results:

i) By the exposure to GaAs surface with HCl gas in low temperature HCl molecules, the chemisorb on the surface as Cl and H atoms near the dimmer vacancies at a monolayer. On the other hand, by the exposure of GaAs to Cl_2 $GaCl_x$ and $AsCl_x$ (x=1, 2, 3) are formed on the surface, at a monolayer.

ii) the etching reaction by HCl is promoted by the desorption of GaCl at 250℃. At this temperature, the surface order is fairly maintained. On the other hand, in the etching by Cl_2, $GaCl_3$ desorbs from the surface at low temperature. The etching reactions by Cl_2 disrupt the GaAs(100) order, of the surface.

The 193 nm laser photoirradiation induces the etching reaction in which Cl-containing species desorb, but 248, 355 and 532 nm laser irradiation shows little effect. The photochemical effect at 193 nm is due to the adsorption of the etching product species.

Chapter 2
Adsorption and photochemical reactions of NO_2 / N_2O_4 on Au surface

2.1 Introduction

The photochemistry of molecules adsorbed on a solid surface has received increasing attention in recent decades since it provides information for adsorbate-surface interactions, including energy and charge transfer, dynamics and kinetics.[1] Nitrogen oxides exhibit a wide variety of structures and have a rich chemistry.[2] Also, many different metastable N_xO_y intermediates [3]can be formed during reactions, and taken together, this has limited the understanding of nitrogen oxides and the development of structure-reactivity relationships. In particular, for interactions with metal atoms, a variety of bonding geometries is usually available. For example, NO_2 is well known as a versatile linkage isomer in coordination compounds [4] and on metal surfaces. [5, 6] However, it is possible to exploit this versatility to cleanly prepared and probe the condensed-phase chemistry of NO_2 and other nitrogen oxides by utilizing suitable substrates, such as Au (111) surface which is very unreactive and thus can be used in many cases to serve as an inert support for condensed phases.

For the surface photochemistry of NO_2, Hasselbrink et al. [7] studied the UV laser-induced desorption of NO from submonolayer NO_2 (actually present as N_2O_4) adsorbed on top of a NO saturated Pd(111) surface. They found two different desorption channels using laser-induced fluorescence, one characterized by non-thermal state populations and the other showing accommodation to the surface. They also carried out polarization experiments, concluding that the photodissociation is initiated by excitation of metal electrons rather than direct photoabsorption by the adsorbate. Dixon-Warren et al. [8] investigated, on the other hand, the photodissociation of NO_2 (N_2O_4) adsorbed on LiF (001), which leads to desorption of NO and NO_2, and determined the translational and internal state distributions of products. They found two different translational energy distributions of NO, and NO_2-coverage dependent translational energy of NO_2. Although they characterized reaction intermediates using IR transmission spectroscopy, they could not reveal the intermediates

because of its low sensitivity and narrow available spectral region, > 1500 cm^{-1}, due to a cutoff of the LiF substrate.

While the motivation of these studies stems from the dynamics of a surface photochemical reaction, the heterogeneous reactions of NO_x species on water ice surfaces have attracted attention in recent years from an environmental chemistry point of view, since the surfaces of polar stratospheric clouds, which mainly consist of water ice, have been implicated as playing a central role in the photochemical mechanism responsible for the yearly occurrence of the ozone hole. [9, 10, 11] Rieley et al. [12] investigated the photochemistry of N_2O_4 adsorbed on ice films formed on a Cu foil using IR reflection absorption spectroscopy (IRAS) for characterization of the adsorption states. They observed the photodesorption of NO_2 alone under near-UV irradiation. Since the wavelength dependence of the NO_2 yield was comparable to the gas-phase absorption cross-section for N_2O_4, they concluded that the photochemistry of N_2O_4 on ice is not significantly different to that of gas-phase N_2O_4. They also studied photodesorption dynamics of NO_2 from N_2O_4 adsorbed on ice surfaces. [13]

Since the photochemical properties of adsorbates are significantly affected by their adsorption states including orientations, *in-situ* characterization of adsorbates by surface spectroscopy could afford deeper insight into a mechanism of surface photochemistry. We have used IRAS for *in-situ* observation of surface species before and during surface photoreaction, [14] because IR spectroscopy has little effect on the electronic states of adsorbates unlike electron spectroscopy such as high-resolution electron energy loss spectroscopy (HREELS). Although a substrate for IRAS study is usually a smooth metal with a high reflection coefficient, various thin films coated on such a metal can also be used. A metal substrate used for surface photochemistry is required to be as inert as possible in order to minimize a change in electronic states due to adsorbates-surface interactions. We have used an Au single crystal as a substrate, since Au is known to be most inactive for gas adsorption among transition metals. [14] The adsorption states of NO_2 on a clean Au (111) surface were already investigated by Koel and his coworker [15, 16] using HREELS, IRAS and temperature programmed desorption (TPD). They found that NO_2 is adsorbed molecularly on the surface to form a surface

chelate at < 170 K (author refers to this species as chemisorbed NO_2), and over the chemisorbed NO_2 layer NO_2 is physisorbed as N_2O_4. They also found that the chemisorbed NO_2 reacts readily with gas-phase NO to form N_2O_3 on the surface.

In this chapter, author reports on the adsorption states of N_2O_4 species on a clean Au (111) surface with IRAS and TPD, and examined its photochemical reaction on the surface.

References

[1] X.-L. Zhou, X.-Y. Zhu and J. M. White, Surf. Sci. Rep., **13**, 73 (1991).

[2] F. A. Cotton and G. Wilkinson, *Advanced Inorganic Chemistry*, Wiley-Interscience, New York (1988).

[3] I. C. Hisatsune, J. P. Devlin and Y. Wada, J. Chem. Phys. **33**, 714 (1960).

[4] M. A. Hitchman, G. L. Rowbottom, Coord. Chem. Rev. **42**, 55 (1982).

[5] B. E. Koel, Chemically Modified Oxide Surfaces, Gordon and Breach Science Publishers, New York (1989).

[6] J. Wang, M. R. Voss, H. Busse and B. E. Koel, J. Phys. Chem. **B102**, 4693 (1998).

[7] (a) E. Hasselbrink, S. Jakubith, S. Nettesheim, M. Wolf, A. Cassuto, G. Ertle, J. Chem. Phys. **92**, 3154 (1990). (b) E. Hasselbrink, S. Nettesheim, M. Wolf, A. Cassuto and G. Ertle, Vacuum **41**, 287 (1990).

[8] St. J. Dixon-Warren, R. C. Jackson, J. C. Polanyi, H. Rieley, J. G. Shapter and H. Weiss, J. Phys. Chem. **96**, 10983 (1992).

[9] S. Solomon, R. R. Garcia, F. S. Rolland and D. J. Wuebbles, Nature **321**, 755 (1986).

[10] O. B. Toon and R. P. Turco, Scient. Amer. **264**, 68 (1991).

[11] O. B. Toon and M. A. Tolbert, Nature **375**, 218 (1995).

[12] H. Rieley, D. P. McMurray and S. Haq, J. Chem. Soc. Faraday Trans. **92**, 933 (1996).

[13] H. Rieley, J. Colboy, D. P. McMurray and S. M. Reeman, J. Phys. Chem. B **101**, 4982 (1997).

[14] S. Sato and T. Suzuki, J. Phys. Chem. **100**, 14769 (1996).

[15] M. E. Bartram and B. E. Koel, Surf. Sci., **213**, 137 (1989).

[16] J. Wang and B. E. Koel, J. Phys. Chem. A **102**, 8573 (1998).

2.2 Experimental

2.2.1 Fourier-transformed infrared absorption spectroscopy

Infrared spectroscopy is probably the most widely used tool in the world today for the identification of chemical compounds. The reasons for the tremendous popularity of the technique are its simplicity, versatility, accuracy, and cheapness. Gaseous, liquid, and solid samples can all be measured spectrometrically with no special sample-handling technique needed on the part of the operator. Functional group information can be gathered easily from an infrared spectrum, and once the spectroscopist has a good idea as to the type of compound that he is measuring, a vast amount of reference data is available in the literature for direct comparison. Thus, unknown materials can usually be rapidly identified. Similarly, individual components of a mixture of known compounds can usually be quantified by infrared spectroscopy by using the available spectrum of each pure component.

In spite of all its apparent benefits, infrared spectroscopy, however, has certain drawbacks. Measurements are slow, and only specially designed spectrometers can measure the complete mid-infrared spectrum in less than a few minutes with acceptable resolution and signal-to-noise ratio. Linked to this time limitation, most infrared spectrometers are not able to measure spectra when the sample has a low baseline transmittance (less than 1%) without taking an excessively long measurement time.

Many problems were being encountered due to the sensitivity of the conventional grating spectrometer that is not adequate. These applications may involve the measurement of very weak bands, the attainment of extremely high resolution, the need for very short measurement times, or monitoring very weak sources of infrared radiation. The development of Fourier transform spectroscopy has allowed many of these difficult measurements to be made much more easily. To understand where the benefits of Fourier transform spectroscopy arise, it is first necessary to understand where the limitations of conventional spectrometers originate.

The fundamental drawback of prism or grating spectrometers is found in the central component - the monochromator. Narrow slits are situated at both the entrance and the exit of the monochromator, which limit the frequency range of the radiation reaching the detector to one resolution width. The purpose of the

entrance slit is to define the beam of light entering the monochromator so that a sufficiently collimated beam of light is incident on the prism or grating. After dispersion of the beam, the second (exit) slit allows only the one small frequency element of interest to reach the detector. The remainder of the beam is reflected from or absorbed by the jaws of the slit and does not reach the detector. The narrower the width of the entrance and exit slits, the higher is the frequency resolution of the spectrometer. However, as the resolution is increased, an even greater proportion of the total radiation from the source is "wasted" on the jaws of the exit slit, and less energy reaches the detector. Even for a low resolution grating spectrometer operating be between 4000 and 400 cm^{-1} at a resolution of 8 cm^{-1}, the proportion of energy reaching the detector at any instant is 8:3600, or about 0.2%. When the resolution is increased to 1 cm^{-1}, the amount of radiation not reaching the detector is 99.97%.

It is therefore easily seen that the monochromator is an inefficient device for measuring infrared spectra over wide frequency ranges at any reasonable resolution. However, until recently, no way of coding the spectral information other than the dispersion by prisms or gratings was considered feasible for the economical measurement of infrared spectra.

At the end of the last century, a different technique had been studied by Michelson, who was the inventor of the interferometer, which now bears his name. The phenomenon of interference of light had been recognized long before this time, but the many significant contributions to the field of optics made by Michelson [1] was the design of an instrument in which two interfering beams are well separated in space so that their relative path differences may be conveniently and precisely varied. Michelson has also been credited as the first person to name such a device an "interferometer."

Infrared reflection absorption spectroscopy (IRAS)

The measurement of a vibrational spectrum for a small amount of adsorbates, which is lesser than 1 monolayer (ML), on a well defined single crystal surface has been the most desirable for surface scientists recently. This demand was caused by the reason that with the great development of a vacuum system, such as UHV, and electron spectroscopy, such as XPS, UPS, AES and EELS (electron energy-loss spectroscopy), the vibrational spectrum of the adsorbate revealed its conformation and reactivity on a clean metal surface.

There are two famous methods for measurements of the vibrational spectrum nowadays, one of them is a high-sensitive Infrared reflection absorption spectroscopy (IRAS), the another is a high-resolution electron energy-loss spectroscopy. In present days, although the latter has relatively high sensitivity and a very wide spectrum range (the lower limit is ~ 100 cm^{-1}), it has an apparent drawbacks that are low resolution (~ 30 cm^{-1}) and only working in the UHV. On the other hand, IRAS works in the ambient air or in the liquid phase, and has a very high resolution which the maximum is ~1 cm^{-1}. Therefore, this method is superior to HREELS on the point of an easy application for various conditions and spectroscopic studies.

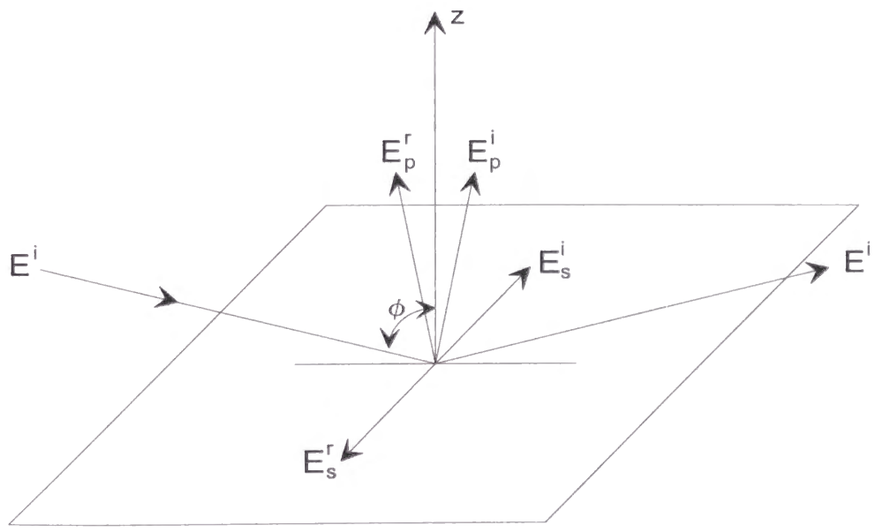

Fig. 2-9. The schematic draw of the infrared reflection on a metal surface.

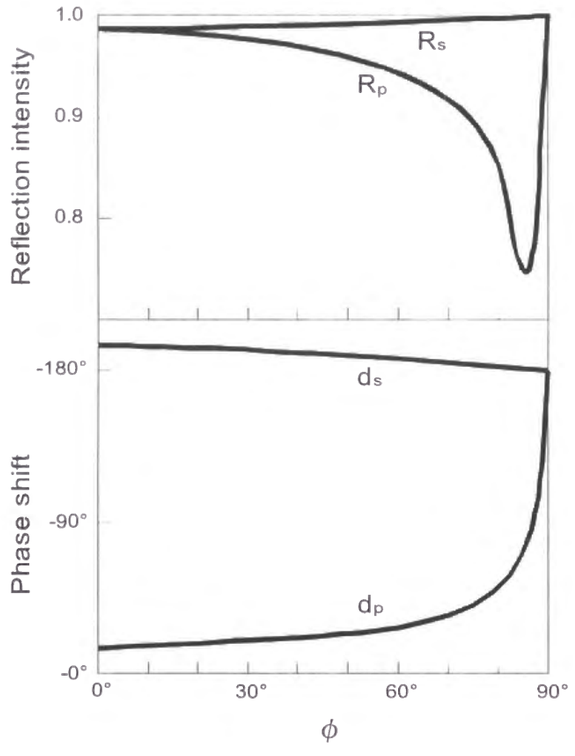

Fig. 2-10. The angler dependence of the incident infrared light to the metal surface (n=3, k=30) on the phase shift and reflectivity. (Ref.[3])

The IRAS measurement is basically different from other transmitted type IR spectroscopy. Now, a basic theory is described below. [2, 3, 4, 5]

The schematic drawing of an infrared reflection on a metal surface is show in Fig. 2-9. In this situation, the clean metal surface having high reflectivity is considerable. As indicated in the figure, the incident angle of the radiation is presented by ϕ as an angle from a surface normal, and incident and reflected lights are in a same plane. Now, the electrical field vector of the incident light, E_I, can be divided to two components, p-polarized one, E_p^I, and s-polarized one, E_s^I. When the complex index of reflection is expressed as $\tilde{n} = n + ik$, in the infrared spectral region $n^2 + k^2 \rangle\rangle 1$ is derived. Therefore, considering the formula of Fresnel, for a reflected infrared light the following equation is concluded:

$$R_p = \frac{(n - \sec\phi)^2 + k^2}{(n + \sec\phi)^2 + k^2}, \qquad (2.1)$$

$$R_s = \frac{(n - \cos\phi)^2 + k^2}{(n + \cos\phi)^2 + k^2}, \qquad (2.2)$$

$$\tan\Delta = \tan(d_p - d_s) = \frac{2k\tan\phi\sin\phi}{\tan^2\phi - (n^2 + k^2)}, \qquad (2.3)$$

where R_p and R_s are the intensity of the p-polarized and s-polarized reflected light, d_p and d_s are the phase shift by reflection of p-polarized and s-polarized light, respectively.

Figure 2-10 shows R_p, R_s, d_p and d_s changes as a function of ϕ. The S-polarized light always keeps only a parallel component for the surface, and changes to 180° at the phase shift in all value of ϕ by a reflection. This means that the electrical field intensity of the surface parallel direction will be zero near the metal surface by the S-polarized light interference. Meanwhile, the p-polarized light is consisted of a surface parallel component, $E_{p//}$ and perpendicular component, $E_{p\perp}$, and its phase shift strongly depends on ϕ. When ϕ is close to 90°, the phase shift of the p-polarized light rapidly change to -180°. Therefore, the electrical field intensity of the surface perpendicular direction caused by the p-polarized light also strongly depends on ϕ. To the contrary, the surface parallel component, $E_{p//}$, is always very small due to a interference of the incident light and reflected light.

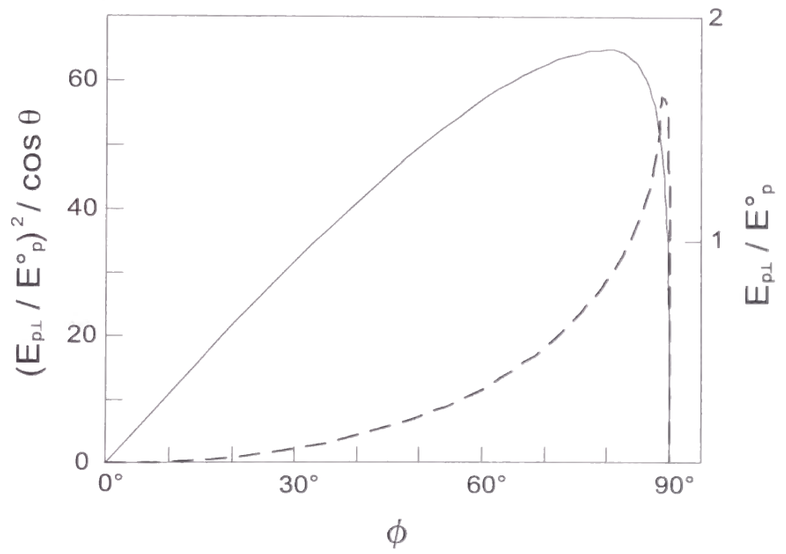

Fig. 2-11. The angler dependence of the electric field perpendicular to the surface, $E_{p\perp}$, and $E_{p\perp}^2/\cos\phi$ for the metal surface (n=3, k=30). (Ref.[3])

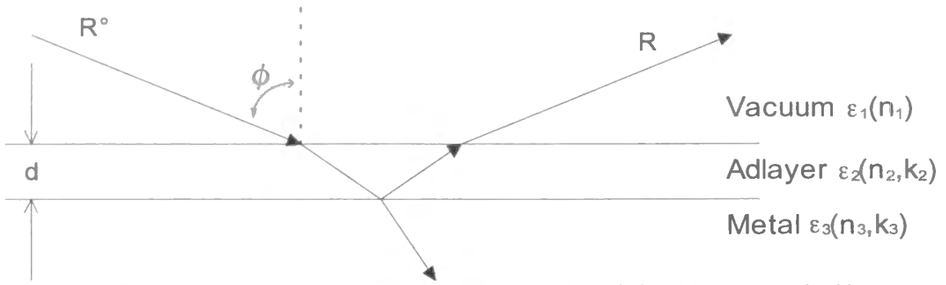

Fig. 2-13. The infrared reflection on the surface (ε_2), which covered with adlayer having the thickness d. (Ref.[2])

Figure 2-11 shows a change of $E_{p\perp}$ as a function of ϕ. It is easily recognized that the large incident angle generates the large electrical field intensity near the surface [6]. Since the beam spot area on the surface is inversely proportional to cos ϕ and the light intensity is proportional to $E_{p\perp}^2$, then the absorption of the adsorbates on the surface, ΔR, should be proportional to $E_{p\perp}^2$ / cos ϕ. As shown in Fig. 2-11, the change of $E_{p\perp}^2$ / cos ϕ has a sharp edge at the high incident angle. Therefore, it is concluded that introducing the p-polarized light at a large incident angle is required to measure a reflective absorption of the adsorbate.

All the discussion above is only for the clean metal surface. If the adlayer is existing on the surface, the three-phases system has to be considered, as shown in Fig. 2-12 [2, 7]. In the figure, ε is an isotropic complex index of

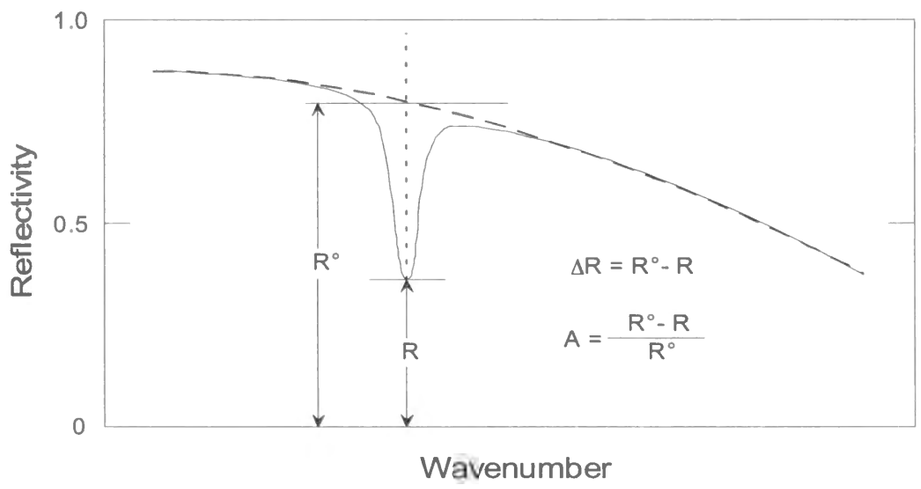

Fig. 2-13. The definition of the change on the reflectivity, ΔR, and absorption coefficient. (Ref. [2])

reflection, $\varepsilon = (n+ik)^2$. Now, ΔR is defined as shown in Fig. 2-13, and then in the condition of $d \langle\langle \lambda$, where d and λ means the thickness of adlayer and the wavelength of the incident light respectively, following equations are given [8]:

$$\frac{\Delta R_s}{R_s} = \frac{8\pi d}{\lambda}\cos\phi\, I_m \frac{(\varepsilon_2-\varepsilon_3)^2}{(1-\varepsilon_3)^2}, \tag{2.4}$$

$$\frac{\Delta R_p}{R_p} = \frac{8\pi d}{\lambda}\cos\phi\, I_m\left(\frac{(\varepsilon_2-\varepsilon_3)^2}{(1-\varepsilon_3)^2}\cdot\frac{1-(1/\varepsilon_2\varepsilon_3)(\varepsilon_2+\varepsilon_3)\sin^2\phi}{1-(1/\varepsilon_3)(1+\varepsilon_3)\sin^2\phi}\right). \tag{2.5}$$

Where now, considering $|\varepsilon_3| \langle\langle |\varepsilon_2| \cong 1$, the change of the s-polarized light intensity, ΔR_s is nearly 0. Meanwhile, about the p-polarized light, assuming $\cos^2\phi > \varepsilon_3^{-1}$, the following equation is derived,

$$\frac{\Delta R_p}{R_p} = \frac{8\pi d\sin^2\phi}{\lambda\cos\phi} I_m\left(-\frac{1}{\varepsilon_2}\right). \tag{2.6}$$

Consequently, whether existing an adlayer or not, the light must be incident to the surface at grazing angle.

As results of these discussions, following general conclusions are given.

i) For requiring high sensitivity, an incident infrared light has to be introduced at a grazing angle (80 - 85°.)

ii) Only the p-polarized component of an incident light electric field vector can interact with the adsorbate on a metal surface.

iii) The vibration spectral absorption of adsorbates, which generates a change of the dipole moment along the surface normal, only can be observable.

Apparatus

All the measurements were carried out in an ultrahigh vacuum chamber system, which is shown in Fig. 2-14. The chamber was equipped with a quadrupole mass spectrometer (ANELVA AQA-200) for desorbed gas analysis, an Ar-ion sputtering gun for cleaning of metal surface, a vertically mounted xyz θ manipulator for controlling the sample direction, and BaF_2 windows (54 mm in diameter) specially made for UHV IRAS[24,25], cut off wavelength of which is around 900 cm^{-1}. The chamber was pumped by a turbomolecular pump (Leybold, 400 L/s) and an ion pump (ANELVA, 270 L/s), and the base pressure was 1×10^{-10} Torr. The sample substrate was held on the sample holder with

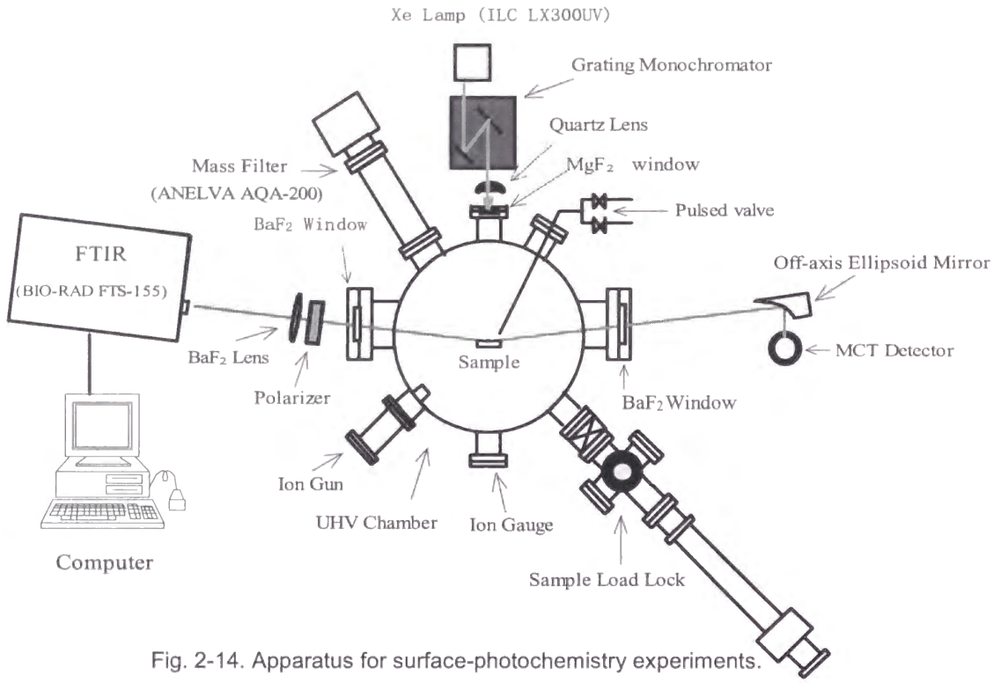

Fig. 2-14. Apparatus for surface-photochemistry experiments.

using Ta wires (0.3mm in diameter). The substrate could be heated by the Ta wire heaters to temperatures higher than 1000 K and cooled to 90 K with a liquid-nitrogen-cooled copper plate. Substrate temperature was measured with a chromel-alumel thermocouple attached to the side of the substrate. Gases were introduced into the chamber through a long nozzle set on a liner-translator, the end of that was ca. 1 cm away from the substrate during dosing processes. A pulsed valve (General Valve) was used to control the dosing amount of a gas.

For IR reflection absorption spectroscopy (IRAS) measurements, IR beam from FTIR (Fourier transform infrared spectrometer, BIO-RAD FTS-155) was introduced into a chamber through a BaF_2 window after p-polarized by a wire grid polarizer since only p-polarized light is effective for IRAS. The reflected IR beam from substrate came to a MCT (Hg-Cd-Te) detector cooled at a liquid N_2 temperature, and then recorded by a computer with passing through some amps and A/D converters electrically. The incidence angle of the IR beam was ca. 85°. The paths of the IR beam were purged with dry air to prevent the effect of an absorption by water vapor at the out side of the chamber, since

such an absorption jams measuring an IR spectrum. All the spectra were recorded with a resolution of 4 cm^{-1} and the average of 200 scans.

TPD (temperature-programmed desorption) spectra were measured with a quadrupole mass spectrometer, which measured the relative amount of molecules desorbed from the substrate, and a programmable temperature regulator (Chino KP-31E) to raise the substrate temperature at a ramp 4 k/s regularly. Both of them were controlled by a computer (NEC PC-9801RX). Since photodesorbing species are mainly NO and NO_2, the mass spectrometric sensitivities for NO and NO_2 are necessary for determination of their ratio. These were measured by an internal standard method using Ar as an internal standard.

Light source for photodissociation

The light source for occurring photochemical reactions on the surface was a paraboloidal-reflector Xe lamp (ILC LX300UV 300W), which was monochromatized by a grating monochromator (RITSU MC-20L) and focused by a quartz lens onto the substrate surface (normal incidence) through a MgF_2 window. A water filter (20 cm long) was used to remove radiative heat. Incident photon flux into the chamber was measured using chemical actinometry. No temperature rise of the substrate was observed during irradiation. When no need to use so high density of the photon flux, the light from the Xe lamp was passed through a band pass filter (300-400 nm, Toshiba UV-D33S.)

2.2.2 Sample preparations

Substrate

A substrate of an Au(111) single crystal (12 mm in diameter, 1.5 mm thick, 99.999 % purity) was purchased from Mateck. The surface of the substrate had been polished by a mechanical polishing machine within a roughness of 0.03μm. Three holes were bored along the edge of the substrate; two of them were passed through by Ta heating wires, and another was attached by thermocouple. The surface was cleaned by repeating Ar ion sputtering at 800 K for 15 min and annealing at 800 - 900 K for 30 min. Ozone was sometimes used for removing hydrocarbons from the surface.

Gas samples

NO_2 used was obtained from Takachiho Kagaku Kogyou. NO_2 was stored in the glass reservoir in the presence of an excess of O_2 to prevent its decomposition to NO and O_2 during storage. The gas mixture was frozen at 77 K and O_2 was pumped away before use. NO_2 was also decomposed in a SUS tube used in a gas handling system during the experiments. The decomposition was, however, greatly suppressed by exposing the inner surface of the tube to NO_2 at a relatively high pressure for a prolonged time. NO was used after adsorption on well-outgased molecular sieve 13X at 77 K. O_3 used for the substrate cleaning in the chamber was generated by passing dry O_2(99.5 % pure) through a silent discharge ozonizer (60 ml/min), and trapped by a cold trap filled with SiO_2 gel at ca. 180 K. H_2O was prepared from distilled water which was degassed in the vacuum line by using freezing-melting procedures repeatedly.

References

[1] (a) A. A. Michelson, Phil. Mag. Ser. 5, **31**, 256 (1891). (b) A. A. Michelson, Phil. Mag. Ser. 5, **34**, 280 (1892).

[2] F. M. Hoffman, Surface Sci. Rep. **3**, 107 (1983)

[3] B. E. Hayden, "Vibrational Spectroscopy of Molecules on Surfaces", Plenum, p. 267 (1987).

[4] S. A. Francis and A. H. Ellison, J. Opt, Soc. Am. **49**, 131 (1959).

[5] G. W. poling, J. Colloid Interface Sci. **34**, 365 (1970).

[6] P. Hollins and J. Pritchard, "Vibrational Spectroscopy of Adsorbates", Springer, 125 and 127 (1980).

[7] R. G. Greenler, J. Chem. Phys. **44**, 310 (1966).

[8] J. D. E. McIntyre and D. E. Aspnes, Surface Sci. **24**, 417 (1971)

2.3 Results

2.3.1 Adsorbed states of NO_2 / N_2O_4 on Au(111)

TPD experiments

A series of TPD experiments on Au (111) was performed as a function of NO_2 exposure. TPD was carried out from 92 K to 400 K. Figure 2-15 shows TPD spectra from NO_2 adsorbed on the Au (111) surface at 92 K. The desorption of NO_2 was detected by monitoring amu = 46. The NO signal was also detected by using amu =30, which is mainly the result of the dissociation of a fraction of NO_2 in the ionizer of mass spectrometer. The subtle mismatch in the line shapes of the NO_2 and NO desorption spectra is the slower pumping speed of the UHV system for NO [1]. This is with the exception of the small desorption feature of NO at 152 K (β peak) which does not trace the desorption of NO_2. This is discussed below. The desorption peak centered at 206 K (γ peak) is attributed to the desorption of NO_2 chemisorbed on the surface and the one at 132 K (α peak) to NO_2 physisorbed on chemisorbed NO_2. A small peak centered at 152 K (β peak) was also observed by Bartram and Koel [1]. They explained that the desorption of NO at 152 K is not the results of NO_2

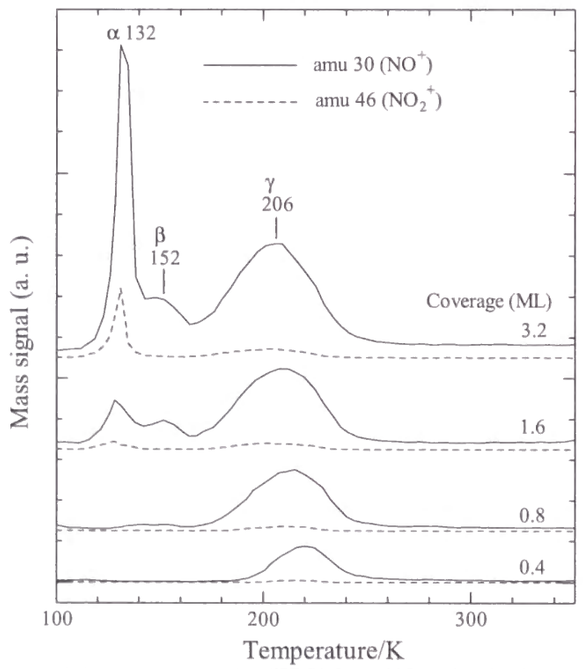

Fig. 2-15. Thermal desorption spectra (TDS) from NO_2 adsorbed on an Au(111) surface as a function of coverage. The temperature ramp was 4 K/s.

decomposition but the decomposition of N_2O_3 on the surface that was formed by the reaction between adsorbed NO_2 and gas-phase NO present in the back ground. The formation of N_2O_3 on the surface will be discussed in later, further more. But author pointed out another possibility that this peak could be attributed to N_2O_4 adsorbed on the vacant Au surface remained after NO_2 chemisorption, taking the IRAS results of the photodissociation experiment discussed in later into account.

The fact that the β peak mainly comprises NO indicates that this N_2O_4 species undergoes thermal decomposition during TPD. Bartram and Koel [1] reported that the exposure necessary for the saturation coverage of chemisorbed NO_2 was ca. 2.0 L (1 L = 10^{-6} Torr·s), and the sticking probability was close to unity for both chemisorbed NO_2 and physisorbed N_2O_4. Based on their results, author takes the saturation coverage of chemisorbed NO_2 as 1 monolayer (ML).

As seen in Fig. 2-15, the NO_2^+/NO^+ ratio for the γ peak is smaller than that for the α peak, indicating that not only NO_2 but also NO was desorbed from chemisorbed NO_2. Corrected with the sensitivity ratio of NO to NO_2 in the mass analysis (ca. 32 in our case), the γ peak was found to involve 26 % of NO in case of Fig. 2-15 (temperature ramp of 4 K/s). NO ratio in γ peak increased with decrease in the temperature ramp of TPD. For the heating rate of 1 K/s, 52 % of the desorbed gases were NO. These results show that the desorption of NO_2 competes with decomposition to NO and adsorbed atomic oxygen. The destination of adsorbed oxygen will be discussed later.

IRAS measurements

IRAS measurement provided the means with which to identify the adsorbate species present on the surface. The use of a grazing incidence geometry in conjunction with a metal substrate affords the opportunity to exploit the metal –surface selection rule [1]. both to simplify the IRAS and to determine the existence of any preferred orientation of molecules with respect to the surface.

Figure 2-16 shows IRA spectra of NO_2 adsorbed on the Au (111) surface at 92 K as a function of exposure from 1 L to 6 L, corresponding to 0.5 - 3 ML. Absorption bands at < 1000 cm^{-1} were not observed due to the cutoff of BaF_2

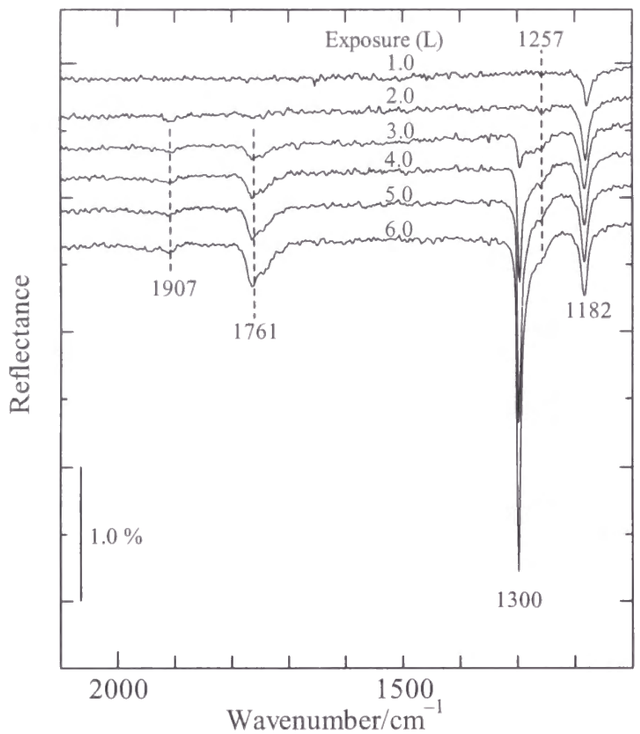

Fig. 2-16. IRA spectra of NO_2 adsorbed on an Au(111) surface at 93 K as a function of exposure. The inset illustrates the adsorption state of chemisorbed NO_2.

windows. Band assignments of adsorbed NO_2 and N_2O_4 are given in Table 2-1 together with those by Koel group [1, 3] and Koch et al. [4] Because IRAS is insensitive to the vibrational modes parallel to the surface (surface selection rule) [5, 6], the asymmetric stretching of chemisorbed NO_2, which is parallel to the surface, cannot be detected by IRAS. A similar surface selection rule has also been reported for HREELS. [7]

The complete absence of the strong asymmetric stretching band of NO_2 around 1600 cm^{-1} indicates the absence of other NO_2 species on the surface. The weak band at 1907 cm^{-1} is attributable to the N-O stretching of N_2O_3 formed by a reaction of chemisorbed NO_2 with gas-phase NO [1, 3], since a trace amount of NO was produced by decomposition of NO_2 during injection. Adsorbed N_2O_3 also exhibits a NO_2 symmetric stretching band at 1274 cm^{-1}. The bands at 1257, 1300, and 1761 cm^{-1} are attributed to condensed N_2O_4 with D_{2h} symmetry as assigned previously. [4, 8, 9] It is widely known that there are some unstable isomers of N_2O_4 in a low temperature inert matrix and in a condensed phase of NO_2. [10-16] Among such isomers, D-isomers, O=N-O-

Table 2-1 Vibrational frequencies (cm^{-1}) and assignments of adsorbed NO_2 and N_2O_4 on Au surfaces.

	chemisorbed NO_2			adsorbed N_2O_4			
mode	HREELS[a]	IRAS[b]	IRAS[c]	HREELS[a]	IRAS[b]	IRAS[d]	IRAS[c]
$\delta(NO_2)$	800	805	n.d.	770	783	785	n.d.
$\nu_s(NO_2)$	1180	1178	1182	1280	1298	1301	1257(first layer) 1300(multilayer)
$\nu_a(NO_2)$	1180		(IRAS inactive)	1755	1735 1760	1750	1761

δ, bending ;ν, stretching. n. d., no data due to the cutoff of the CaF_2 windows.

a) Ref. 1.

b) Ref. 3.

c) This work

d) Ref. 4; Chemisorbed NO_2 was not observed, since the surface was not cleaned.

NO_2, may play an important role in the photochemistry of condensed N_2O_4, because D-isomers can be thermally converted into nitrosonium nitrate, $NO^+NO_3^-$, [13-16] and undergo more rapid photolysis than $N_2O_4(D_{2h})$ in an Ar matrix [17]. D-isomers exhibit IR bands at 1290-1310 cm^{-1} (NO_2 symmetric stretching), 1630-1645 cm^{-1} (NO_2 asymmetric stretching), and 1820-1830 cm^{-1} (N=O stretching) in IRAS as well as in transmission IR. [10-16] Although the band at 1300 cm^{-1} in Fig. 2-16 is very close to the NO_2 symmetric stretching of D-isomers, any other bands attributable to D-isomers were not observed in our experiments. No change was observed in IRAS after adsorbed N_2O_4 was annealed at 120 K, indicating that the 1300 cm^{-1} band is not due to unstable D-isomers.

2.3.2 Photochemistry of N_2O_4 adsorbed on Au(111)

Photodesorbed species

UV irradiation (230-400 nm) of chemisorbed NO_2, which was formed by NO_2 adsorption at 160 K, led to no evolution of gases. IRAS showed no change in the 1184 cm^{-1} band intensity even after prolonged irradiation. Thus, electric quenching is very rapid in the photodissociation of chemisorbed NO_2, probably due to bonding formation of the two oxygen atoms with the Au surface [1].

UV irradiation of multilayer N_2O_4 led to desorption of NO and NO_2 without any other species. Figure 2-17 shows time dependent gas evolution during irradiation at 92 K. At low coverages, a sharp spike of NO desorption was observed at the beginning of illumination. This spike was found to arise from rapid photodissociation of adsorbed N_2O_3 in a separate experiment, in which adsorbed N_2O_3 alone was illuminated. The details of N_2O_3 photodissociation will be reported in the next section. At higher coverages, the initial rapid

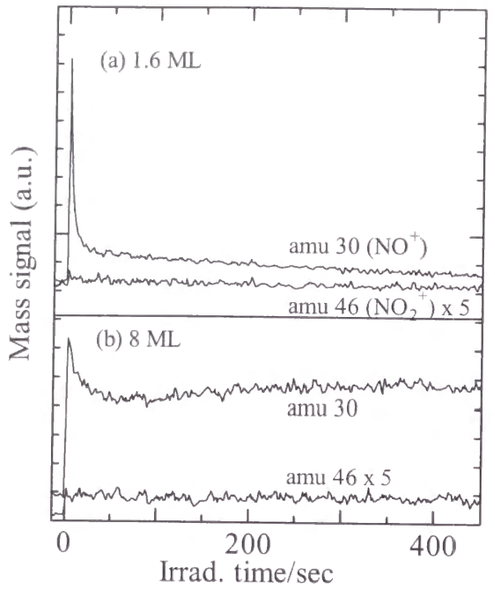

Fig. 2-17. Photodesorption of NO_2 and NO from NO_2 adsorbed on an Au(111) surface at 92 K. A band pass filter (UV-D33S, 230-400 nm) was used for irradiation was 4 K/s.

desorption of NO was significantly suppressed. After complete decomposition of N_2O_3, the photodesorption of NO and NO_2 almost leveled off. A slight increase in NO yield after 1 min irradiation may be due to destruction of the ordered N_2O_4 layer, since ordered N_2O_4 would undergo rapid relaxation. The yields of NO_2 and NO photo-desorbed from multilayer N_2O_4 were determined after the decomposition of N_2O_3 as a function of coverage (Fig. 2-18). The NO_2/NO ratio was nearly unity at low coverages and increased with increasing coverage. The NO_2/NO ratio in the present system is greater than that reported for the N_2O_4/NO/Pd(111) system [18], where at least 90% of the desorbed molecules were NO under 193 nm radiation. The NO_2/NO ratio in adsorbed N_2O_4 photolysis was found to be sensitive to surface species preadsorbed on the substrate. For instance, when the Au surface was covered with n-decane (~1 ML), the photo-desorbed molecules from the physisorbed N_2O_4 layer (1 ML) were predominantly NO at 350 nm. [19] The NO_2/NO ratio in the present system also depended upon substrate temperature as shown in Fig. 2-19. In this experiment NO_2 was adsorbed at < 96 K, and then the substrate was heated to each temperature, followed by photodesorption measurement. No N_2O_4 was desorbed at any temperature. The temperature dependence for NO_2

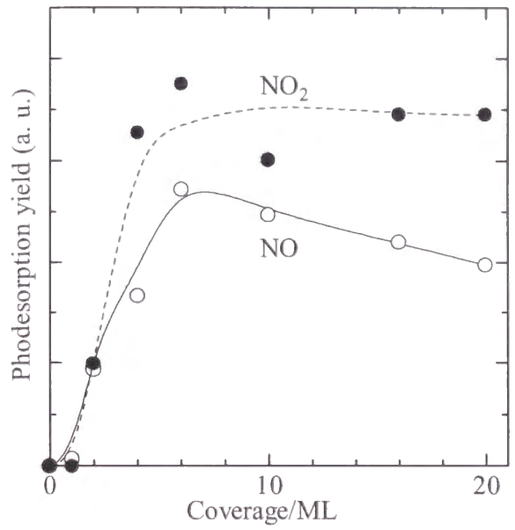

Fig. 2-18. Photodesorption yields of NO_2 and NO as a function of coverage at 93 K. A band pass filter (UV-D33S, 230-400 nm) was used for irradiation.

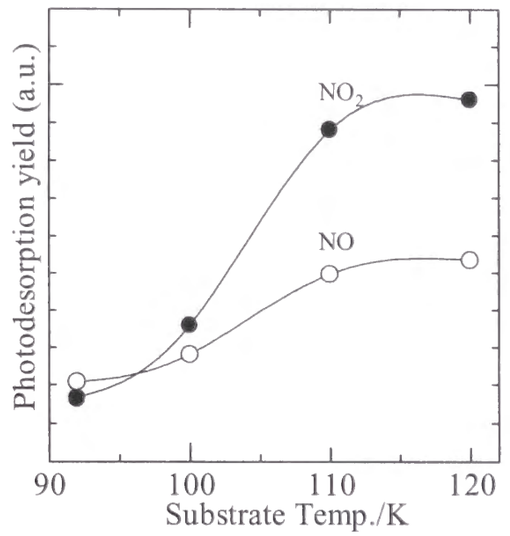

Fig. 2-19. Temperature dependence of the photodesorption yields of NO_2 and NO. The total coverage of adsorbed NO_2 was 3.6 ML. A band pass filter (UV-D33S, 230-400 nm) was used for irradiation.

photodesorption was more remarkable than for NO desorption; NO_2 yield at > 110 K was more than 4 times greater than that at 95 K, while the increase in NO yield was about two-hold. Because the yield of a photochemical reaction is basically independent of temperature, this result indicates that some thermal processes significantly reduce the photodesorption yields at < 110 K. The NO_2 yield could be suppressed by a back reaction, $2NO_2(ad) \rightarrow N_2O_4(ad)$, while the NO yield by a reaction such as $NO + O(a) \rightarrow NO_2(a)$.

Neither atomic nor molecular oxygen was detected in the gas phase during multilayer N_2O_4 photolysis, indicating that adsorbed atomic oxygen or oxygen-containing species other than the already-detected NO_x species must be formed on the surface. Careful examination of IRA spectra after prolonged irradiation led us to conclude that any new NO_x species such as NO_3 or N_2O_5 were not produced by the photolysis. The author have recently investigated the reactivities of ozone and atomic oxygen adsorbed on Au(111) surface, which was produced from adsorbed ozone, and found that a reaction of N_2O_4 with O or O_3 adsorbed on Au surface gives no products at < 100 K, but NO reacts with O to form $NO_2(a)$. [19] For the NO-covered Pd(111) surface, Hasselbrink et al. [18] reported no formation of adsorbed oxygen after irradiation and ascribed

this result to a reaction of adsorbed atomic oxygen with pre-adsorbed NO. They found, however, adsorbed atomic oxygen when N_2O_4 was directly adsorbed on a clean Pd(111) surface. [18]

To detect adsorbed oxygen in our system, TPD was carried out after the photodissociation of multilayer N_2O_4. As shown in Fig. 2-20, O_2 desorption was observed at around 507 K in TDS, indicating the formation of adsorbed atomic oxygen during the photolysis. While it is widely known that Au surface is unable to adsorb O_2, Canning et al. [20] reported that atomic oxygen produced by a hot Pt filament is promptly adsorbed on Au surfaces at room temperature to form oxide layer, from which O_2 is desorbed at > 500 K. It is therefore reasonably concluded that atomic oxygen produced by the photodissociation of multilayer N_2O_4 remains on the Au surface without reacting with the NO_x species. In passing, Fig. 2-15 shows that chemisorbed NO_2 is partly decomposed to NO without O_2 evolution during TPD. Also in this case O_2 desorption was observed at 507 K, when the adsorption-desorption cycle of chemisorbed NO_2 was repeated a few times at < 400 K to accumulate atomic oxygen on the surface. Requisite for the accumulation of atomic oxygen would arise from consumption

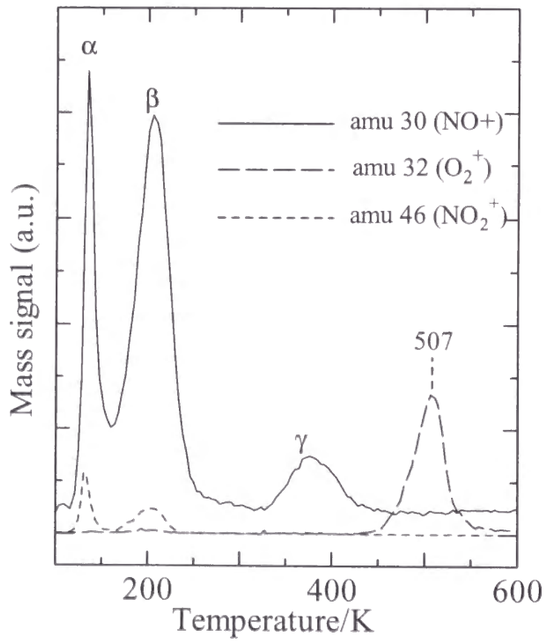

Fig. 2-20. TDS after 8-min photolysis of NO_2 (2 ML) adsorbed on an Au(111) surface at 93 K. A band pass filter (UV-D33S, 230-400 nm) was used for irradiation. The origin of the δ peak is not clear, but IRAS showed that the species giving the δ peak is not present on the front surface of the substrate.

of atomic oxygen by its reactions with residual gases such as CO in the UHV chamber during TPD. In fact, CO was found to react with atomic oxygen on the Au surface even at 95 K. [19]

Photodissociation Cross Sections

Figure 2-21 shows changes in the IRAS bands of chemisorbed NO_2, N_2O_3, and first-layer and multilayer N_2O_4 (2.5 ML total coverage) during irradiation at 350 nm. At the beginning of illumination, the 1900 cm^{-1} band assigned to N_2O_3 disappears within 1 min due to its rapid photodecomposition, while the 1182 cm^{-1} band (chemisorbed NO_2) increases slightly corresponding to the conversion of N_2O_3 into chemisorbed NO_2. The 1296 cm^{-1} band (multilayer N_2O_4) also increased slightly upon illumination, but the reason for this is obscure at the present. As seen in Fig. 2-21, the 1261 cm^{-1} band (first-layer N_2O_4) remains unchanged even under prolonged irradiation like chemisorbed NO_2. This result indicates that the quenching of photoexcited states is significant for first-layer N_2O_4 due to its direct contact with the surface.

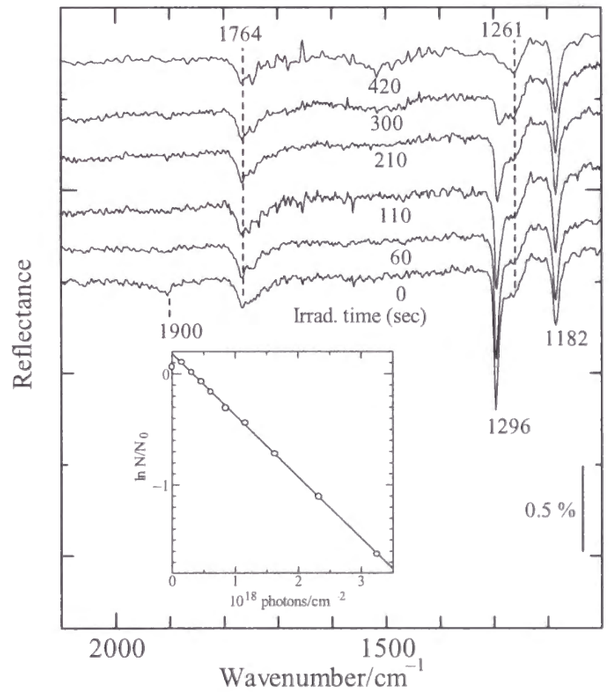

Fig. 2-21. Change in IRA spectrum during the photolysis at 350 nm. The initial coverage of adsorbed NO_2 was 2.5 ML. The inset is the semilogarithmic plots of the residual amount of multilayer N_2O_4 for determination of a cross section (see text).

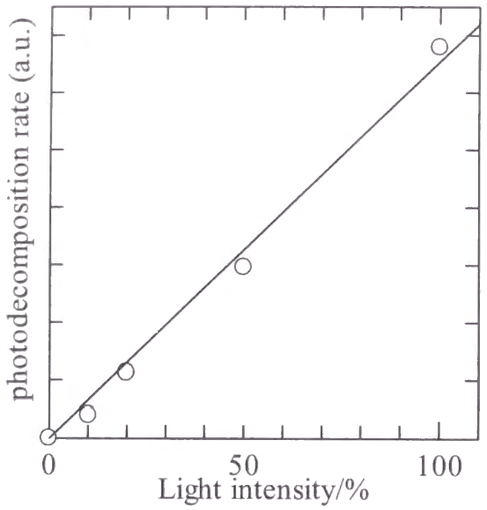

Fig. 2-22. Light intensity dependence of the decreasing rate of multilayer N_2O_4 under irradiation at 350 nm. Neutral density filters were used to control light intensity. The initial coverage of adsorbed NO_2 was 2.5 ML, and the substrate temperature 92 K.

The time dependence of the 1296 cm^{-1} band absorbance assigned to the NO_2 symmetric stretching of multilayer N_2O_4 follows a simple exponential law except for initial 1 min. This indicates that the amount of residual multilayer N_2O_4, N, is given as [21]

$$N = N_0 \exp(-\sigma n_{hv}) \qquad (2.7)$$

where N_0 is the initial amount of multilayer N_2O_4, σ the cross section, and n_{hv} the number of photons irradiated. From the absorbance of the NO_2 symmetric stretching at 1296 cm^{-1}, N/N_0 was determined. The inset of Fig. 2-21 shows the plots of ln N/N_0 versus n_{hv}. The cross section is determined from the slope to be 5.6×10^{-19} cm^2. This value is larger than the cross section, ca. 1.3×10^{19} cm^2, determined for the N_2O_4/NO/Pd(111) system [18] at 351 nm, but close to the absorption cross section, 5.7×10^{19} cm^2, of gas-phase N_2O_4 at 350 nm [22, 23]. Thus, the quantum yield of the present system is found to be remarkably high. Light intensity dependence of the photodissociation cross section of multilayer N_2O_4 was measured at 350 nm with neutral density filters. The decreasing rate of the 1296 cm^{-1} band absorbance was virtually proportional to light intensity as shown in Fig. 2-22. Wavelength dependence of the photodissociation cross section was measured with monochromatic light. as shown in Fig. 2-23. Similar wavelength dependence of the photodissociation cross section was reported for the N_2O_4/NO/Pd(111) system using 248, 308, and 351-nm lasers.[18] The

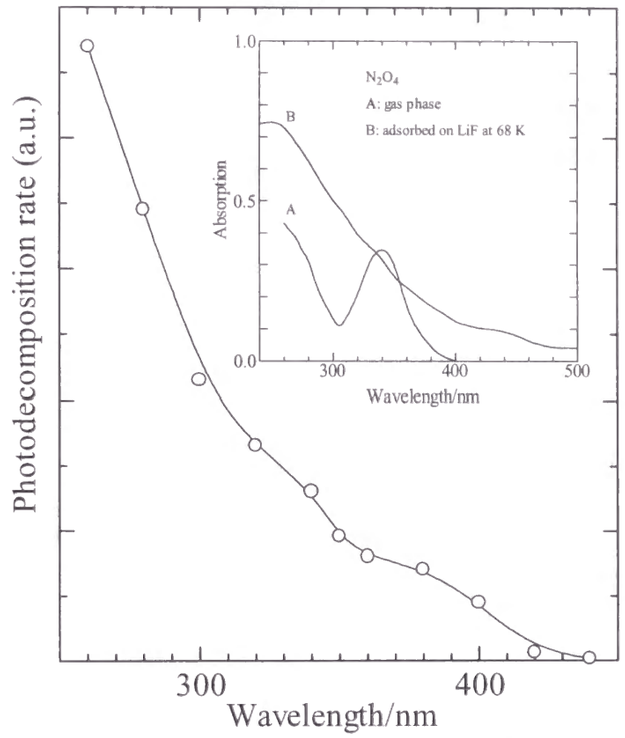

Fig. 2-23. Wavelength dependence of the photodissociation cross section of multilayer N_2O_4 at 93 K. The total coverage of adsorbed NO_2 was 3 ML. The inset shows the absorption spectra of (a) gas-phase N_2O_4(ref. 22) and (b) N_2O_4 adsorbed on LiF at 68 K(Ref. 24).

inset of the figure shows the absorption spectra of gas-phase N_2O_4 [22] and NO_2 (N_2O_4) adsorbed on LiF at 68 K [24]. The observed wavelength dependence of the cross section is very similar to the absorption spectrum of N_2O_4 adsorbed on LiF, except for the absorption edge. Although this similarity seems to imply direct photoabsorption by multilayer N_2O_4, there exists a possibility of photoexcitation of the Au surface, since light absorption by a metal also increases with increasing photon energy.

To examine such a surface effect, the photodissociation of adsorbed N_2O_4 was carried out on a thin film of water ice (~5 ML) formed on the Au surface. Gas-phase water was adsorbed at 130 K in this experiment in order to minimize surface roughness and grain boundaries. Although photoinduced electrons were found to pass through water layers formed on a Ni(111) surface at 50 K, 5 ML water layers were enough to prevent electron transmission. [25] IRAS showed that NO_2 is adsorbed on the ice film as N_2O_4, which is very similar in adsorption state to multilayer N_2O_4 on the Au surface. Figure 2-24 shows the

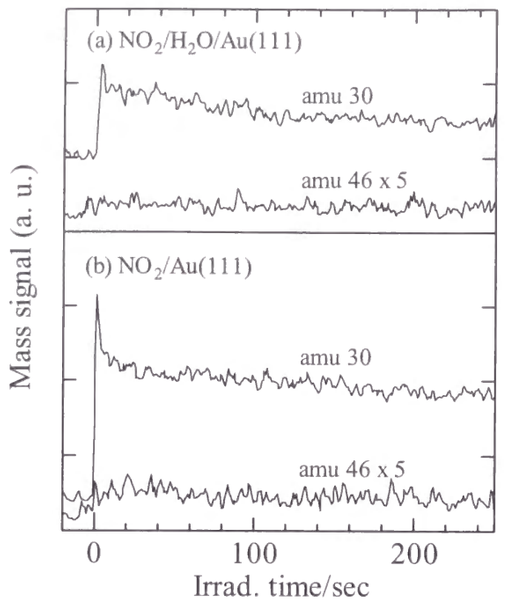

Fig. 2-24. Effect of a thin ice film (~5 ML) covering the Au(111) surface on the photodesorption of NO_2 and NO from adsorbed NO_2 (2.5 ML) at 93 K under irradiation at 350 nm; (a) on the ice film and (b) on the bare Au surface.

time-dependent mass signals of photo-desorbing gases from N_2O_4 on the ice surface at 92 K together with the corresponding profile for the $N_2O_4/NO_2/Au(111)$ system. For Fig. 2-24(b) the initial sharp peak of NO desorption is due to the rapid photodecomposition of N_2O_3 adsorbed on Au(111) surface as described before. From comparison of the two photodesorption profiles except for the initial N_2O_3 dissociation, author is confident that the photodesorption yields of NO and NO_2 from multilayer N_2O_4 on the Au(111) surface are greater than those from N_2O_4 adsorbed on the ice surface. IRAS observation also confirmed greater photolysis rates of N_2O_4 on the Au surface than on the ice surface. Since the surface of an insulator such as water ice is thought to give little effects on the yield of a surface photoreaction, this result suggests the enhancement of N_2O_4 photodissociation by effects of the Au surface.

References

[1] M. E. Bartram and B. E. Koel, Surf. Sci., **213**, 137 (1989).

[2] H.A. Rearce and N. Sheppard, Surf. Sci. **98**, 5974 (1994).

[3] J. Wang and B. E. Koel, J. Phys. Chem. A **102**, 8573 (1998).

[4] T. G. Koch, A. B. Horn, M. A. Chesters, M. R. S. McCoustra and J. R. Sodeau, J. Phys. Chem. **99**, 8362 (1995).

[5] R. G. Greenler, R. R. Rahn and J. P. Schwartz, J. Catal., **23**, 42 (1971)

[6] W. Suetaka, *Surface Infrared and Raman Spectroscopy*, Prenum Press: New York and London, p13 (1995).

[7] H. Ibach and D. L. Mills, *Electron Energy Loss Spectroscopy and Surface Vibrations*, Academic Press: New York, (1982).

[8] R. N. Wiener and E. R. Nixon, J. Chem. Phys. **26**, 9.6 (1957).

[9] A. Givan and A. Loewenschuss, J. Chem. Phys. **93**, 866 (1990).

[10] W. G. Fateley, H. A. Bent and Jr., B. Crawford, J. Chem. Phys. **31**, 204. (1939).

[11] I. C. Hisatsune, J. P. Devlin and Y. Wada, J. Chem. Phys. **33**, 714 (1960).

[12] E. L. Varetti and G. C. Pimentel, J. Chem. Phys. **55**, 3813 (1971).

[13] A. Givan and A. Loewenschuss, J. Chem. Phys. **90**, 6135 (1989).

[14] A. Givan and A. Loewenschuss, J. Chem. Phys. **91**, 5126 (1989).

[15] A. Givan and A. Loewenschuss, J. Chem. Phys. **93**, 7592 (1990).

[16] A. Givan and A. Loewenschuss, J. Chem. Phys. **94**, 7562 (1991).

[17] H. Bandow, H. Akimoto, S. Akiyama, T. Tezuka, Chem. Phys. Lett. **111**, 496 (1984).

[18] (a) E. Hasselbrink, S. Jakubith, S. Nettesheim, M. Wolf, A. Cassuto, G. Ertle, J. Chem. Phys. **92**, 3154 (1990). (b) E. Hasselbrink, S. Nettesheim, M. Wolf, A. Cassuto and G. Ertle, Vacuum **41**, 287 (1990).

[19] unpublished results.

[20] N. D. S. Canning, D. Outka and R. J. Madix, Surf. Sci. **141**, 240 (1984).

[21] X.-L. Zhou, X.-Y. Zhu and J. M. White, Surf. Sci. Rep., **13**, 73 (1991).

[22] T. C. Hall and F. E. Blacet, J. Chem. Phys. **20**, 1745 (1952).

[23] H. S. Johnston and R. Graham, Can. J. Chem. **52**, 1415 (1974).

[24] W.Bach and H. D. Breuer, Discuss. Faraday Soc. **58**, 237 (1974).

[25] T. L. Gilton, C. P. Dehnbostel and J. P. Cowin, J. Chem. Phys. **91**, 1937 (1989).
[26] S. Sato, T. Senga and M. Kawasaki, J. Phys. Chem. B **103**, 5063 (1999).

2.4 Discussion

2.4.1 Formation mechanisms of N_2O_4 on the Au(111) surface

In our IRAS measurements (Fig. 2-16), the 1257 cm^{-1} band grew only at low coverages (< 2 ML), and therefore, this band could be assigned to N_2O_4 directly adsorbed on Au surface (author refers to this species as first-layer N_2O_4). When the substrate temperature was elevated after NO_2 adsorption, the 1257 cm^{-1} band remained after disappearance of the 1300 cm^{-1} band and disappeared at around 160 K. Therefore, the β peak in TPD is attributable to first-layer N_2O_4. The IRA spectrum of first-layer N_2O_4 resembles the IR transmission spectrum of gas-phase N_2O_4, in which the band intensities of symmetric and asymmetric NO_2 stretching are comparable, indicating random configuration of first-layer N_2O_4. NO_2 is physisorbed (condensed) on both chemisorbed NO_2 and first-layer N_2O_4 as N_2O_4 (author refers to physisorbed N_2O_4 as multilayer N_2O_4). For multilayer N_2O_4, the O-N-O symmetric stretching band, which vibrational mode is parallel to the C_2 axis (N-N bond axis), grow s solely with increasing coverage as shown in Fig. 2-16. Similar results have been obtained for the Au foil [1] and the water ice surfaces [2] as well as for the chemisorbed NO_2/Au(111) system[3]. Based on the surface selection rule of IRAS[4, 5], author can conclude that multilayer N_2O_4 is aligned preferentially with the C_2 axis perpendicular to the surface. All discussed above for the state of N_2O_4 adsorption were schematically drawn in Fig. 2-28.

The sticking probability of NO_2 to form multilayer N_2O_4 was significantly

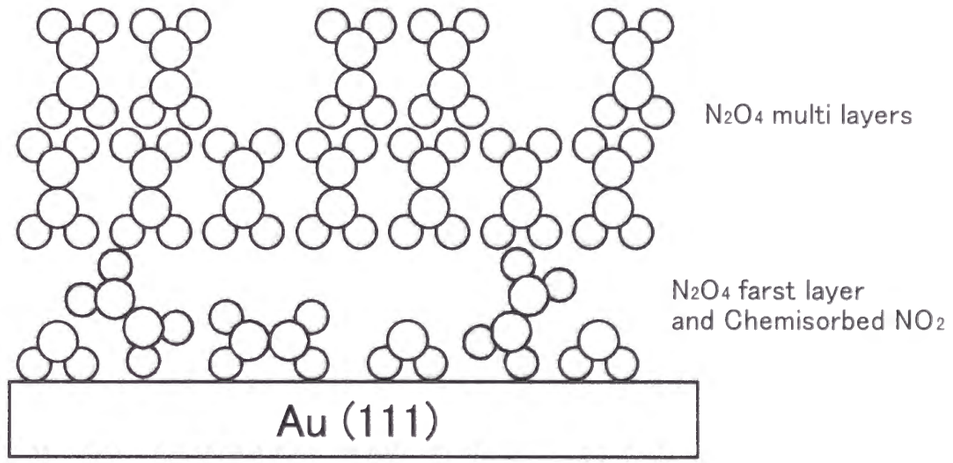

Fig. 2-28 Schematic drawing of the adsorbing N_2O_4 state on the Au (111) surface.

attenuated at > 110 K, although those for chemisorbed NO_2 and first-layer N_2O_4 were still close to unity. At 120 K the sticking probability of multilayer N_2O_4 was about one tenth of that observed at 90 K. When the substrate was heated after formation of multilayer N_2O_4 at 91 K, however, multilayer N_2O_4 bands did not disappear at 120 K. It was seemed that multilayer N_2O_4 formed at low temperature (91 K) is crystallized in increasing temperature to 120 K, on the other hand, N_2O_4 formed at high temperature (120 K) is vaporized soon due to the low binding energy to the surface.

2.4.2 Photodissociation mechanisms of adsorbed N_2O_4

Whether or not a surface photoreaction on a metal surface occurs by substrate photoexcitation can be determined by a polarization probe method, in which the polarization-dependent yield is measured as a function of the incident angle of light. [9] Hasselbrink et al. [10] applied this method to the N_2O_4/NO/Pd(111) system at 193 and 248 nm and concluded that the photoabsorption by the metal is the dominant primary step in the photodissociation. The enhancement of photoreactions on metal surfaces is usually ascribed to photoelectron capture. Photoelectron emission from Pd, however, could not occur at > 220 nm, since the work function of clean Pd is 5.6 eV. Hasselbrink et al. [10], therefore, assumed that electrons created by the light of energies less than the work function penetrate the potential barrier at the metal/adsorbate interface through tunneling and induce the photolysis. The optical absorption coefficient of Pd changes, however, only by a factor of 1.5 in the wavelength region from 351 to 193 nm. This change, therefore, cannot explain the observed pronounced increase (more than 10 hold) of the cross section with increase in photon energy. Weik et al. [11] have proposed a hot electron cascade mechanism to explain the wavelength dependence of the O_2 photodesorption from O_2 adsorbed on Pd(111) surface.

Au surfaces absorb photons more efficiently than Pd surfaces in the UV region. Photoabsorption by an evaporated Au film has been reported to be 64 % at 360 nm (normal incidence). [12] Although the absorption of Au(111) surface in the UV region is not available, it would be close to the evaporated-film value. Similar to Pd surfaces, photoelectron emission from an Au surface could not occur in the wavelength region of our present experiments, since the

work function of Au is 5.3 eV, which corresponds to a photon wavelength of 234 nm. In addition, the formation of chemisorbed NO_2 results in a work function increase of 1.6 eV. [6] Tunneling electron transfer from the Au surface to multilayer N_2O_4 may be responsible for the large cross section of multilayer N_2O_4 photodissociation. A change in the absorption by an evaporated Au film in the wavelength region from 250 to 400 nm is, however, so small (only a 9 % increase [12]) that the observed wavelength dependence of the cross section cannot be explained in terms of the photoelectron of the Au surface. The wavelength dependence could be ascribed to the hot electron mechanism proposed by Weik et al.[11], but there are other possibilities. A large increase in the work function upon NO_2 adsorption on Au(111) surface [6] implies that significant electron transfer from the substrate to chemisorbed NO_2 occurs. When NO_2 is adsorbed on chemisorbed NO_2, electron transfer would occur from chemisorbed NO_2 to multilayer N_2O_4. Such electron transfer could increase the photo-absorption cross section of multilayer N_2O_4. To determine whether direct absorption occurs or not, the polarization probe experiment was conducted and discussed in Chapter 4.

Sisk et al. [13] studied in detail the dynamics of gas-phase N_2O_4 photolysis by a photolysis-induced fluorescence method and concluded that N_2O_4 is photodecomposed as

$$N_2O_4 + h\nu \rightarrow NO_2^* (B^2B_1, \nu_2=3\text{-}4) + NO_2 (X^2A_1) \quad (2.8)$$

(λ =351 nm)

$$N_2O_4 + h\nu \rightarrow NO_2^* (^2B_1) + NO_2^* (^2B_2) \quad (2.9)$$

(λ =248 nm).

Their proposed energy diagram for N_2O_4 photolysis predicts that there are no photodissociation channels of N_2O_4 to direct formation of NO at > 300 nm. If multilayer N_2O_4 is similar to N_2O_4(g) in photochemical character, then NO would be mainly produced by photodissociation of intermediate NO_2(ad). Such a mechanism is implausible for NO photodesorption from multilayer N_2O_4. First, photo-production of NO from intermediate NO_2(ad) would depend quadratically on light intensity, contrary to the experimental result, if the cross section of NO_2(ad) is not so different from that of NO_2(g). Secondly, IRAS could not detect NO_2(ad) during the photolysis. The stretching bands of NO_2 are so strong that

NO_2(ad) could be detected by IRAS even at coverages as low as 0.1 ML. Thirdly, the electronic states of multilayer N_2O_4 may be different from those of N_2O_4(g), as evidenced by the fact that the absorption spectrum of N_2O_4 adsorbed on LiF is quite different from that of N_2O_4(g). We assume, therefore, that N-O bond breaking occurs first in multilayer N_2O_4 photolysis to form N_2O_3, which undergoes spontaneous photodissociation to produce NO_2 and NO. Since the photodissociation cross section of adsorbed N_2O_3 is one order of magnitude greater than that of multilayer N_2O_4 (described in Chapter 4), the light intensity dependence is virtually linear in this case, and the population of N_2O_3 during photolysis becomes too small to detect by IRAS.

Hasselbrink et al. [10] found that the NO yield is linear on laser fluence and the mean translational energy of the desorbing NO is independent of laser energy at 193, 248, 308, and 351 nm in the N_2O_4/NO/Pd(111) system. Based on these results, they speculated the formation of nitrosonium nitrate, $NO^+NO_3^-$, in the dark, because this ionic form has often been observed in condensed N_2O_4 layers. [14-17] If $NO^+NO_3^-$ is present in adsorbed N_2O_4, neutralization of NO^+ by electron capture would result in NO desorption with simultaneous tunnel back of an electron from NO_3^- to the metal surface resulting in formation of NO_2. Givan and Lowenschuss [16] reported that $NO^+NO_3^-$ is produced upon temperature cycling only from less ordered N_2O_4 layers, in which D-isomers are involved, but not from well ordered N_2O_4 (D_{2h}) layers. For our N_2O_4/NO_2/Au(111) system, IRAS showed clearly that multilayer N_2O_4 is dominantly ordered with the C_2 axis perpendicular to the surface. Furthermore, neither $NO^+NO_3^-$ nor NO_3^- was detected on the surface before and during the photolysis. Failure in detecting $NO^+NO_3^-$ due to insufficient sensitivity of IRAS can be ruled out, since $NO^+NO_3^-$ has been detected by IRAS previously. [14-17] Therefore, the concentration of $NO^+NO_3^-$, if present, would be so small that it plays no important role in our system. It was also reported that matrix isolated D-isomers are mainly converted into N_2O_4 (D_{2h}) under illumination, but not to $NO^+NO_3^-$. [18]

References

[1] R. N. Wiener and E. R. Nixon, J. Chem. Phys. **26**, 9.6 (1957).

[2] H. Rieley, D. P. McMurray and S. Haq, J. Chem. Soc. Faraday Trans. **92**, 933 (1996).

[3] J. Wang and B. E. Koel, J. Phys. Chem. A **102**, 8573 (1998).

[4] R. G, Greenler, R. R. Rahn and J. P. Schwartz, J. Catal. **23**, 42 (1971).

[5] W. Suetaka, *Surface Infrared and Raman Spectroscopy*, Prenum Press: New York and London, p13 (1995).

[6] M. E. Bartram and B. E. Koel, Surf. Sci. **213**, 137 (1989).

[7] H. Ibach and D. L. Mills, *Electron Energy Loss Spectroscopy and Surface Vibrations*, Academic Press: New York, 1982.

[8] S. Sato, T. Senga and M. Kawasaki, J. Phys. Chem. B **103**, 5063 (1999).

[9] X.-L. Zhou, X.-Y. Zhu and J. M. White, Surf. Sci. Rep., **13**, 73 (1991).

[10] (a) E. Hasselbrink, S. Jakubith, S. Nettesheim, M. Wolf, A. Cassuto, G. Ertle, J. Chem. Phys. **92**, 3154 (1990). (b) E. Hasselbrink, S. Nettesheim, M. Wolf, A. Cassuto and G. Ertle, Vacuum **41**, 287 (1990).

[11] F. Weik, A. de Meijere and E. Hasselbrink, J. Chem. Phys. **99**, 682 (1993).

[12] *Chronological Scientific Tables*, Ed. by National Astronomical Observatory, Maruzen: Tokyo, p. 521 (1997).

[13] W. N. Sisk, C. E. Miller and H. S. Johnston, J. Phys. Chem. **97**, 9916 (1993).

[14] E. L. Varetti and G. C. Pimentel, J. Chem. Phys. **55**, 3813 (1971).

[15] A. Givan and A. Loewenschuss, J. Chem. Phys. **90**, 6135 (1989).

[16] A. Givan and A. Loewenschuss, J. Chem. Phys. **91**, 5126 (1989).

[17] A. Givan and A. Loewenschuss, J. Chem. Phys. **93**, 7592 (1990).

[18] H. Bandow, H. Akimoto, S. Akiyama, T. Tezuka, Chem. Phys. Lett. **111**, 496 (1984).

2.5 Conclusion

NO_2 is adsorbed on a clean Au(111) surface at < 120 K to form chemisorbed NO_2, N_2O_4 in direct contact with the surface (first-layer N_2O_4), and physisorbed N_2O_4 in multilayers. Multilayer N_2O_4 is oriented with the C_2 axis predominantly perpendicular to the surface. While chemisorbed NO_2 and first-layer N_2O_4 undergo neither photodissociation nor photodesorption, multilayer N_2O_4 is photodecomposed to NO_2 and NO at < 430 nm. The photodissociation cross section of multilayer N_2O_4 at 350 nm was determined to be 5.6×10^{-19} cm^2, which is close to the absorption cross section of gas-phase N_2O_4. When the Au surface was covered with a thin water ice film (~5 ML), the yields of NO_2 and NO dropped significantly as compared to the bare surface, suggesting that the photodissociation is enhanced by substrate excitation or by electron transfer from the surface to the adsorbates. The wavelength dependence of the cross section is very similar to the absorption spectrum of N_2O_4 adsorbed on LiF at 68 K. The yield of the photodissociation is almost linear on light intensity. No intermediate species such as NO_2(ad), N_2O_3(ad), or $NO^+NO_3^-$ were detected by IRAS during the photolysis. These results indicate that multilayer N_2O_4 is photodecomposed to NO_2, NO, and atomic oxygen without formation of stable intermediates.

Chapter 3
Adsorption and photochemical reactions of NO_2 / N_2O_3 on Au surface

3.1 Introduction

Photochemical reactions of molecules adsorbed on solid surfaces depend strongly on chemical and physical properties of the surfaces. [1-3] In general, a photoexcited state on a metal surface is quenched rapidly due to its coupling to the electron bath in the substrate, even when reactants are not chemically bonded to the surface. In some cases, however, cross sections of adsorbed molecules are comparable to or greater than those in the gas phase, because photo-induced electron transfer from the metal surface to the adsorbates occurs. [3, 4-7] In Chapter 2, the author found that the photodissociation cross section of N_2O_4 adsorbed on the NO_2-covered Au(111) surface is as large as those in the gas- and condensed phase. [7] Since the yield of the N_2O_4 photodissociation was significantly reduced when the surface was covered with a thin water-ice film, we concluded that the N_2O_4 photolysis is enhanced by photoexcitation of the Au surface. The spectral profile of the photodissociation cross sections is, however, not similar to the absorption spectrum of an Au surface, but rather resembles that of N_2O_4 adsorbed on a LiF crystal. Based on these results, the author has proposed an electron transfer mechanism from the Au surface to the adsorbed N_2O_4. [7]

In this chapter, the author report on the rapid photodissociation of N_2O_3 adsorbed on an Au(111) surface. N_2O_3 is formed by reaction of chemisorbed NO_2 with gaseous NO at < 130 K. [8][9] The photodissociation cross section will be determined by using a Xe arc lamp and monochromator.

References

[1] T. J. Chuang, H. Seki and I. Hussla, Surf. Sci. **158**, 525 (1985)

[2] D. S. King and R. R. Cavanagh, Adv. Chem. Phys. **76**, 45 (1989)

[3] X.-L. Zhou, X.-Y. Zhu and J. M. White, Surf. Sci. Rep. **13**, 73 (1991)

[4] P. R. Antoniewicz, Phys. Rev. B **21**, 3811 (1980)

[5] J. W. Gadzuk, L. J. Richter, S. A. Buntin, D. S. Kingand and R. R. Cavanagh, Surf. Sci. **235**, 317 (1990)

[6] J. A. Miesewich, T. F. Heinz and D. M. Newns, Phys. Rev. Lett. **68**, 3737 (1992)

[7] S. Sato, T. Senga and M. Kawasaki, J. Phys. Chem. B **103**, 5063 (1999)

[8] M. E. Bartram and B. E. Koel, Surf. Sci. **213**, 137 (1989)

[9] J. Wang and B. E. Koel, J. Phys. Chem. A **102**, 8573 (1998)

3.2 Experimental

All measurements were carried out in an ultrahigh vacuum system, which has been described in Chapter 2. An Au(111) single crystal (12 mm in diameter, 1.5 mm thick, 99.999% purity) used as a substrate was cleaned by repeating Ar-ion sputtering at 800 K and annealing at 900 K. Ozone was sometimes used for surface cleaning. Gases were analyzed with a mass spectrometer (ANELVA AQA-200). For IR reflection absorption spectroscopy (IRAS) measurements, An IR beam from FTIR (BIO-RAD FTS-155) was p-polarized by a wire grid polarizer and then introduced into a chamber through a BaF_2 window, whose cutoff wavelength is around 900 cm^{-1}. The incident angle of the IR beam was ~85°. The paths of the IR beam were purged with dry air to reduce the effects of moisture. IRA spectra were recorded with 4 cm^{-1} resolution and 200 scans. The light source was a paraboloidal-reflector Xe lamp (ILC LX300UV, 300 W), which was monochromatized by a grating monochromator (RITSU MC-20L) and focused by a quartz lens onto the sample through an MgF_2 window. Incident photon flux into the chamber was measured with chemical actinometry. To reduce light intensity neutral density filters (Toshiba) were used.

NO_2 was stored in a glass reservoir in the presence of an excess of O_2 to prevent its decomposition to NO and O_2 during storage. The gas mixture was frozen at 77 K and O_2 was pumped away before use. NO was used after adsorption on a well-outgassed molecular sieve 13X at 77 K. Gases were introduced into the chamber through a long nozzle, the end of which was ca. 1 cm away from the substrate. A pulsed valve (General Valve) was used to control exposures of gases to the surface.

3.3 Results

3.3.1 Characterization of Adsorption States

N_2O_3 chemisorbs on an Au surfaces at > 150 K and undergoes thermal decomposition as it desorbs at 210 K. [1] So, we first prepared "chemisorbed" NO_2 on an Au(111) surface at 160 K. Then, N_2O_3 was prepared on the Au(111) surface at < 100 K by the reaction of gaseous NO with the chemisorbed NO_2. [1] [2-3] Figure 3-1 shows IRA spectra of chemisorbed NO_2 and N_2O_3. The band at 1184 cm^{-1} is assigned to the NO_2 symmetric stretching of chemisorbed NO_2. This band decreases in intensity upon NO exposure with growth of the new bands at 1274 and 1900 cm^{-1} and remains even the new bands are saturated after 2 L exposure of NO. These new bands are assigned to NO stretching and NO_2 asymmetric stretching of N_2O_3, respectively. The intensities of these bands at saturation were found to depend on the initial coverage of the chemisorbed NO_2. Figure 3-2 shows a linear relation between the relative coverages of chemisorbed NO_2 and adsorbed N_2O_3, in which relative coverage is defined as IRAS intensity ratios at various conditions to the saturation intensity. Figurer 3-2

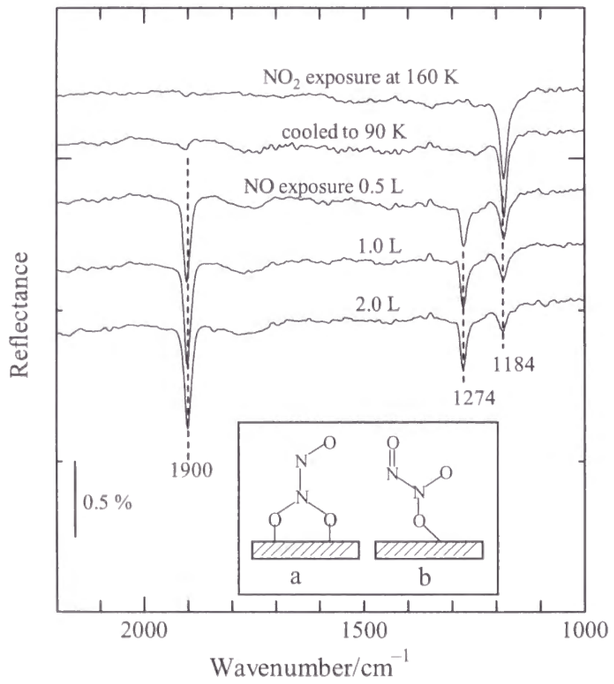

Figure 3-1. IRA spectra of adsorbed N_2O_3 formed by the reaction of NO_2 chemisorbed on Au(111) with gas-phase NO at 90 K. Chemisorbed NO_2 is prepared at 160 K. The inset shows two different adsorption states of N_2O_3 (See text).

shows that N_2O_3 is formed only for coverage of NO_2, >0.5, indicating that a part of chemisorbed NO_2 does not react with NO. Actually in Figure 3-1, the 1184 cm^{-1} band of chemisorbed NO_2 remains even after saturation of the N_2O_3 bands. It is worthy to note that the total intensity of the 1184 and 1274 cm^{-1} bands does not change with NO exposure.

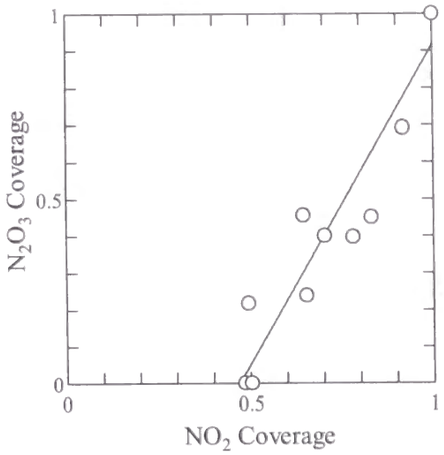

Figure 3-2. Relation between the relative coverages of chemisorbed NO_2 and adsorbed N_2O_3. The coverages were calculated from the absorption intensities of IRAS bands.

When the substrate is heated, adsorbed N_2O_3 undergoes thermal decomposition at > 110 K as shown in Figure 3-3. Thermal decomposition is completed at < 160 K with the complete recovery of chemisorbed NO_2. In agreement with these results, NO desorbed during temperature programmed desorption with a peak maximum at 148 K, while NO_2 did not. The N-N bond breaking of adsorbed N_2O_3 occurs at temperatures as low as 160 K. The N-N bond dissociation energy is close to

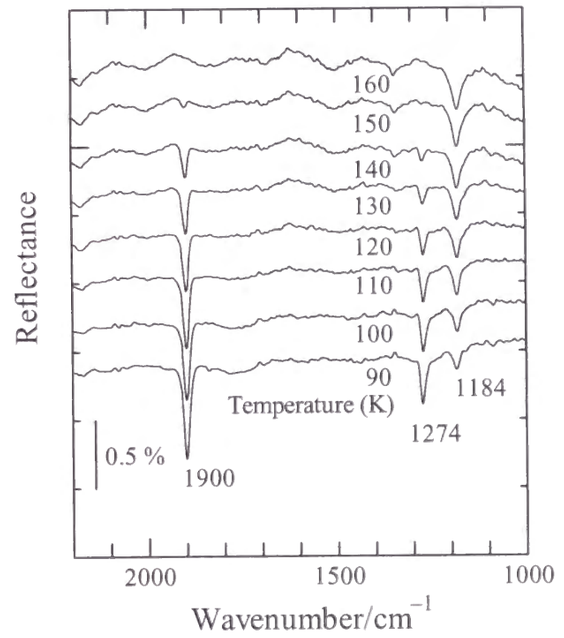

Figure 3-3. Change in the IRA spectrum of adsorbed N_2O_3 as a function of substrate temperature.

Table 3-1. Vibrational frequencies (cm^{-1}) of N_2O_3 adsorbed on Au(111) and N_2O_3 in CH_2Cl_2[a]

	N_2O_3 in CH_2Cl_2	N_2O_3/Au(111)		
Mode	IR (transmission)[b]	HREELS[b]	IRAS[c]	IRAS[d]
$\nu(O_2N\text{-}NO)$	253	250		n. d.
$\rho(O_2NNO)$	614	450-650		n. d.
$\delta(NO_2)$	772	800	806	n. d.
$\nu_s(NO_2)$	1291	1180	1182	1274
$\nu_a(NO_2)$	1600	1270	1272	(IRAS inactive)
$\nu(NO)$	1849	1890	1897	1900

[a] ν, stretching; ρ, rocking; δ, bending; n.d., no data due to the cutoff of the BaF_2 windows. [b] Reference [4]. [c] Reference [3]. [d] This work. The NO_2 asymmetric stretching of chemisorbed NO_2 cannot be observed by IRAS because IRAS is sensitive only to vibrational modes perpendicular to the surface because of the surface selection rule. Refs. [5-6].

that of N_2O_3 in CH_2Cl_2, since the N-N stretching frequencies of both N_2O_3 molecules are close to each other as shown in Table 3-1.

3.3.2 Photodissociation of adsorbed N_2O_3

Photodissociation of adsorbed N_2O_3 at 350 nm was so efficient that NO photodesorption measured by the mass spectrometer was almost completed within 30 s as shown in Figure 3-4. The initial rise of the NO yield was almost proportional to light intensity. For IRAS measurements, light intensity was reduced by the use of a 5 % neutral density filter to reduce the photolysis rate. IRA spectra of adsorbed N_2O_3 during photolysis are shown in Figure 3-5. The bands at 1900 and 1274 cm^{-1} assigned to N_2O_3 decreased with irradiation time, while the band at 1184 cm^{-1} assigned to chemisorbed NO_2 increased due to the conversion of adsorbed N_2O_3 into chemisorbed NO_2 and gaseous NO. No other bands were detected during irradiation. The residual amount of N_2O_3 is given by N;

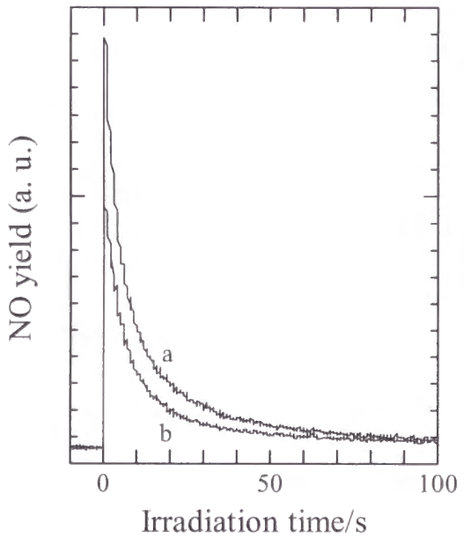

Figure 3-4. Temporal profile of NO yield during the 350 nm photolysis of adsorbed N_2O_3 at 93 K. a, no filter; b, 70 % neutral density filter.

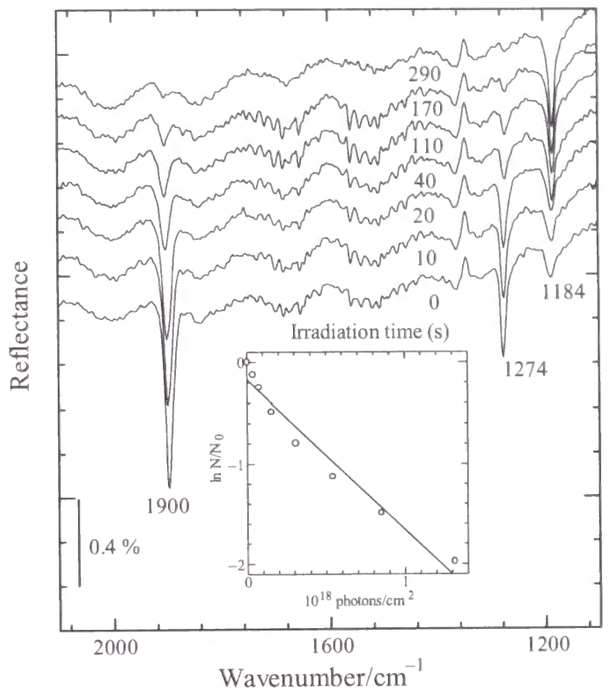

Figure 3-5. IRAS change during the 350 nm photolysis of adsorbed N_2O_3 at 93 K. A 5 % neutral density filter was used to reduce light intensity. The inset is the semilogarithmic plots of residual N_2O_3 during the photolysis.

$$N = N_0 \exp(-\sigma n_{h\nu}), \qquad (3.1)$$

where N_0 is the initial amount of N_2O_3, σ the photodissociation cross section, and $n_{h\nu}$ the number of photons irradiated.[3] The semilogarithmic plots of the absorbance of the 1900 cm^{-1} band are shown in the inset of Figure 3-5. The plots are not exactly linear with irradiation time; the cross section seems to decrease with decreasing coverage of N_2O_3. In fact, the cross section becomes small when the initial coverage of N_2O_3 was reduced. The reason for this is not clear, but probably the electron transfer process is quenched by the chemisorbed NO_2 surrounding N_2O_3. The average cross section is determined from the slope to be 3.0×10^{-17} cm^2. This value is one of the highest cross sections ever reported for surface photochemical reactions on metal substrates [2].

The wavelength dependence of the NO yield is shown in Figure 3-6. The photodesorption of NO occurred to some extent even at 700 nm due to an n $\rightarrow$ π^* transition [7]. The inset of Figure 3-6 shows the UV-region absorption spectra of N_2O_3 in the gas phase, an aqueous solution and a n-hexane solution [7]. The absorption maximized at around 250 nm is attributed to a $\pi \rightarrow \pi^*$ transition. The absorption of N_2O_3 increases upon dissolution into the solvents, and its peak shifts toward the longer wavelengths. A maximum cross section increases from 9.6×10^{-18} cm^2 at 225 nm for gaseous N_2O_3 to 1.6×10^{-17} cm^2 at 240 nm for N_2O_3 in an aqueous solution. The maximum cross section observed for the photodissociation of adsorbed N_2O_3 is, however, much larger than the absorption cross section of N_2O_3 in the gas-phase and the solutions. Furthermore, the absorption for the latter declines sharply toward longer wavelengths and becomes nearly zero at 350-400 nm. The large cross section of adsorbed N_2O_3, therefore, may be ascribed to substrate photoexcitation.

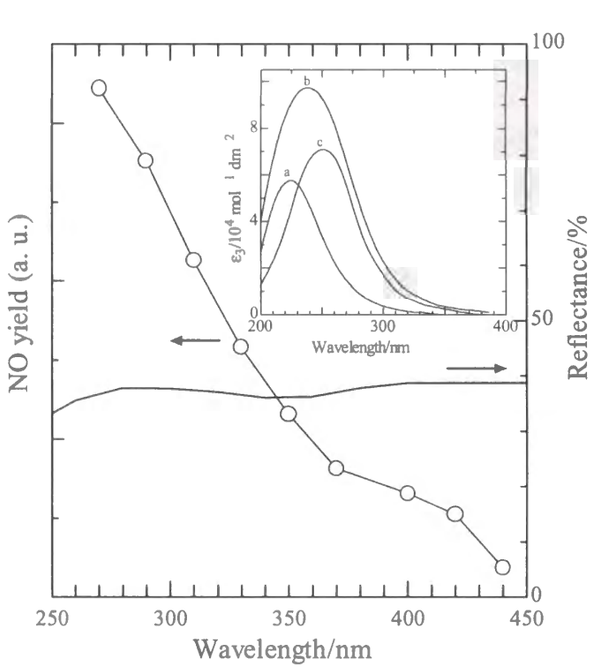

Figure 2-6. Wavelength dependence of initial NO yield in the photolysis of adsorbed N_2O_3 at 93 K and the reflectivity of an evaporated Au film. (Ref. [*8*]) The inset is the absorption spectra of N_2O_3 in the gas phase (a), an aqueous solution (b), and a n-hexane solution (c). (Ref.[7])

Although photoelectron emission from an Au surface does not occur under irradiation at < 234 nm due to its large work function (5.3 eV), photo-induced electron transfer from the surface to adsorbates can occur by tunneling through the metal/adsorbate barrier.

References

[1] S. Sato, T. Senga and M. Kawasaki, J. Phys. Chem. B 103, 5063 (1999)

[2] T. J. Chuang, H. Seki and I. Hussla, Surf. Sci 158, 525 (1985)

[3] X.-L. Zhou, X.-Y. Zhu and J. M. White, Surf. Sci. Rep. 13, 73 (1991)

[4] J. A. Miesewich, T. F. Heinz, D. M. Newns, Phys. Rev. Lett. 68, 3737 (1992)

[5] P. R. Antoniewicz, Phys. Rev. B 21, 3811 (1980)

[6] J. W. Gadzuk, L. J. Richter, S. A. Buntin, D. S. Kingand and R. R. Cavanagh, Surf. Sci. 235, (317) 1990

[7] A.W. Shaw and A. J. Vosper, J. Chem. Soc. Dalton Trans. 961 (1972)]

[8] *Chronological Scientific Tables*, Ed. by National Astronomical Observatory, Maruzen: Tokyo, p. 521 (1997)

3.4 Discussion

3.4.1 Formation mechanisms of N_2O_3 on the Au(111) surface

Koel and his coworkers [1-2] studied the adsorption states of chemisorbed NO_2 and adsorbed N_2O_3 on an Au(111) surface by HREELS and IRAS. They assigned the HREELS and IRAS bands of adsorbed N_2O_3 with reference to the IR transmission spectrum of N_2O_3 in CH_2Cl_2. Their band assignments are listed in Table 2-1 together with our IRAS results. Their assignments are in good agreement with the IR transmission spectrum of N_2O_3 in CH_2Cl_2 except for the 1180 and 1274 cm^{-1} bands, which were assigned to symmetric and asymmetric stretching of chemisorbed NO_2, respectively. Since our result indicates that a part of chemisorbed NO_2 remain unreacted with gaseous NO, it is reasonable to assign the 1180 cm^{-1} band to the NO_2 symmetric stretching of chemisorbed NO_2 and the 1274 cm^{-1} band to the NO_2 symmetric stretching of N_2O_3. The absence of the NO_2 asymmetric stretching mode of N_2O_3 in IRAS and HREELS is due to the surface selection rule [3-5].

For adsorbed N_2O_3, Koel and his coworkers [1-2] had originally proposed the adsorption state (a) as shown in the inset of Figure 2-25. Recently, they have revised it to the adsorption state (b), since the symmetric and asymmetric NO_2 stretching bands are comparable in intensity, while the NO stretching band is stronger than the NO_2 stretching bands. Their recent revision seems to be inadequate, since the NO_2 stretching vibration may be restricted when NO_2 is bound to the surface like the adsorption state (a). In addition, the strong NO stretching band of N_2O_3 could arise from charge transfer from Au surface to NO, because chemisorbed NO_2 is bonded so strongly to the Au surface. Actually. chemisorbed NO_2 undergo neither photodissociation nor photodesorption. [6] Since the chelating NO_2 on the Au(111) surface would remain unchanged after formation of N_2O_3, the adsorption state (a) is much more likely than the adsorption state (b).

3.4.2 Photodissociation mechanisms of adsorbed N_2O_3

Whether or not a surface photoreaction on a metal surface occurs by substrate photoexcitation can be determined by a polarization probe method, in which the polarization-dependent yield is measured as a function of the incident angle of light. [7] Hasselbrink et al.[8, 9] applied this method to the

photodissociation of N_2O_4 adsorbed on a NO-saturated Pd(111) surface at 193 and 248 nm and concluded that the photoabsorption by the metal is the dominant primary step in the photodissociation. Because photoelectron emission from a Pd surface does not occur at > 220 nm due to its work function (5.6 eV), they attributed the photodissociation to electron transfer from the surface to the adsorbate. We have found a large cross section in the photodissociation of N_2O_4 adsorbed on a NO_2-covered Au(111) surface.[6]

The yield of the N_2O_4 photodissociation was significantly reduced when the surface was covered with a thin water-ice film so that we concluded enhanced photolysis due to photo-induced electron transfer from the surface to adsorbed N_2O_4. Similar photo-induced electron transfer from a metal surface to adsorbates has been reported for NO adsorbed on Cu(111), using the two-photon photoemission spectroscopy. [10]

The absorption spectra of Pd and Au, however, cannot explain the wavelength dependence of the N_2O_4 photodissociation yields as discussed in Chapter. 2. [6] That is also the case for the present N_2O_3/Au(111) system. As shown in Figure 3-6, the reflectivity of an evaporated Au film [11] varies to a small extent in the wavelength range observed, while the N_2O_3 photodissociation yield changes drastically. Therefore, a simple mechanism involving electron attachment would be ruled out and we propose a mechanism involving enhancement of the direct absorption of adsorbed N_2O_3 by electron transfer from the surface. Shaw and Vosper [12] observed that the visible absorption of N_2O_3 in organic solvents increases with decrease in the ionization potential of the solvent. For instance, the absorption maximum of N_2O_3 was 97 $mole^{-1}dm^2$ at 730 nm in carbon tetrachloride, while it was 275 $mole^{-1}dm^2$ at 690 nm in m-dimethoxybenzene. Their results indicate that electron donation from the solvent to N_2O_3 enhances the absorption of N_2O_3. Although the absorption maximum in the UV region could not be measured due to strong absorption of the solvents, it is sure that the UV absorption also increases with the donor ability of the solvent, judging from significant increase in the tail of the $\pi \rightarrow \pi^*$ transition in the visible region. [12] For NO_2/Au and N_2O_3/Au, Bartram and Koel [1] observed a large increase in work function (1.6 eV) upon NO_2 adsorption on the Au(111) surface and the lowering of the work function (-0.8 eV) upon

formation of adsorbed N_2O_3. The increase in work function indicates electron transfer from Au surface to chemisorbed NO_2, and the decrease in work function after N_2O_3 formation would arise from electron transfer from NO_2 to NO in adsorbed N_2O_3, which can reduce the shielding effect of NO_2. The strong NO stretching of adsorbed N_2O_3 may indicate this electron transfer toward NO. It is, therefore, reasonably assumed that electron transfer from Au surface to adsorbed N_2O_3 greatly enhances its absorption in the UV region as well as in the visible region. Thus, the wavelength dependence of the photodissociation of N_2O_3 adsorbed on the Au(111) surface is similar in shape to the absorption spectrum of N_2O_3 in the gas phase or in a solvent as observed in the present study.

References

[1] M. E. Bartram and B. E. Koel, Surf. Sci. **213**, 137 (1989)

[2] J. Wang and B. E. Koel, J. Phys. Chem. A **102**, 8573 (1998)

[3] T. G. Koch, A. B. Horn, M. A. Chesters, M. R. S. McCoustra and J. R. Sodeau, J. Phys. Chem. **99**, 8362 (1995)]

[4] R. G. Greenler, R. R. Rahn and J. P. Schwartz, J. Catal. **23**, 42 (1971)

[5] H. Ibach and D. L. Mills, *Electron Energy Loss Spectroscopy and Surface Vibrations*, Academic Press: New York, (1982)

[6] S. Sato, T. Senga and M. Kawasaki, J. Phys. Chem. B **103**, 5063 (1999)

[7] X.-L. Zhou, X.-Y. Zhu and J. M. White, Surf. Sci. Rep., **13**, 73 (1991)

[8] E. Hasselbrink, S. Jakubith, S. Nettesheim, M. Wolf, A. Cassuto, G. Ertle, J. Chem. Phys. **92**, 3154 (1990)

[9] E. Hasselbrink, S. Nettesheim, M. Wolf, A. Cassuto and G. Ertle, Vacuum **41**, 287 (1990)

[10] I. Kinoshita, A. Misu, T. Munakata, J. Phys. Chem. **102**, 2970 (1995)

[11] *Chronological Scientific Tables*, Ed. by National Astronomical Observatory, Maruzen: Tokyo, p. 521 (1997)

[12] A. W. Shaw and A. J. Vosper, J. Chem. Soc. Dalton Trans. 961 (1972)

3.5 Conclusion

The author report rapid photodissociation of N_2O_3 adsorbed on an Au(111) surface. N_2O_3 was formed by reaction of chemisorbed NO_2 with gaseous NO at < 130 K. N_2O_3 was formed only for coverage of NO_2, >0.5, indicating that a part of chemisorbed NO_2 does not react with NO. The adsorbed N_2O_3 is oriented predominantly perpendicular to the surface.

Photodissociation of adsorbed N_2O_3 at 350 nm generated only desorbing NO species. The photodissociation was so efficient that NO photodesorption measured by the mass spectrometer was almost completed within 30 s. The average cross section is 3.0×10^{-17} cm^2. This value is one of the highest cross sections ever reported for surface photochemical reactions on metal substrates. The maximum cross section observed for the photodissociation of adsorbed N_2O_3 is much larger than the absorption cross section of N_2O_3 in the gas-phase and the solutions. The photodissociation is enhanced by substrate excitation or by electron transfer from the surface to the adsorbates. Electron transfer from Au surface to adsorbed N_2O_3 greatly enhances its absorption in the UV region as well as in the visible region. The wavelength dependence of the photodissociation of N_2O_3 adsorbed on the Au(111) surface is similar in shape to the absorption spectrum of N_2O_3 in the gas phase or in a solvent. The author proposes a mechanism involving enhancement of the direct absorption of adsorbed N_2O_3 by electron transfer from the surface.

Chapter 4

Photochemical reaction dynamics of N_2O_4 on Au

4.1 Introduction

In Chapter 2, the author investigated for photochemical reactions of N_2O_4 on the Au surface. The information about both adsorption state and photodesorbing species was obtained from results. Now, then the author would like to report about the reaction dynamics of N_2O_4 on the Au surface by using the laser spectroscopic method, the resonance-enhanced multi photoionization time-of-flight technique (REMPI-TOF). The experimental results about the translational, vibrational and rotational energy of desorption species will be discussed in this chapter.

Laser photochemical reaction dynamics at surface

The rapid growth currently taking place in the field of surface photochemistry [1-13] is driven by potential technological applications [14-22], such as photochemical etching and deposition, which are relevant to the fabrication of new materials and devices, as well as by scientific interest in fundamental questions concerning the mechanisms of energy transfer between the radiation field, electronic and vibrational substrate excitations, and various degrees of freedom of adsorbed molecules. A powerful way to obtain insight into the dynamics of molecular processes at surfaces involves the determination of translational and internal energy distributions of desorbed product species. Combined with theoretical modeling, this approach has led to quite detailed understanding of the dynamics of such processes as molecule-surface scattering, sticking (through detailed balance), and thermal and reactive desorption [23-30]. Since many photochemical surface reactions result in desorbing species (i.e., substrate or adsorbate molecules, their dissociation fragments, or reaction products), the same techniques can be applied to investigate the dynamics of surface photochemistry.

Photochemical surface reactions are initiated by the absorption of photons by the adsorbate or the substrate, and followed by various energy transfer and relaxation processes that eventually lead to nuclear motion along the reaction coordinates. The goal of experimental and theoretical investigations in this area is to obtain a detailed understanding of all the elementary steps involved. In addition to the excitation mechanism, this includes the dynamics of molecular motion during the reaction. Knowledge of the dynamics is crucial for the understanding of the reaction as a whole, since it represents the link between potential energy surfaces, coupling strengths and relaxation rates on the one hand, and measurable final state distributions of desorbing products on the other.

Desorbed diatomic or polyatomic products can contain large amounts of information in the final state distributions of the various translational and internal degrees of freedom. These include the angular distribution, the translational, vibrational, and rotational energy distributions, the spatial alignment of angular momentum vectors, and populations of electronic states such as spin-orbit states and lambda doublets. Knowledge of such projections of the final state distribution onto the various degrees of freedom does not exhaust the information contained in the full final state distribution, however, since much can be learned from correlations between two or more degrees of freedom, e.g., the angle-resolved velocity distribution, or the translational energy distribution as a function of rotation or vibrational state, to name just a few.

Despite this apparent wealth of information, there exists no straightforward way of quantitatively utilizing it to gain direct insight into the reaction mechanism and dynamics. One can often draw qualitative conclusions by comparing the product energy distributions with thermal distributions at the surface temperature or with gas phase photolysis results, or by examining how variations in the experimental conditions affect the final state distributions. However, a more quantitative analysis generally requires postulating a model for the reaction mechanism, performing a dynamical simulation (quantum mechanical or classical) for this model, and comparing the calculated final state distributions to the observed ones. Although knowledge of important model parameters (relating to structure, potential energy surfaces and relaxation rate) is in most cases very limited, this approach has been taken for a number of systems [31-52]. The majority of these studies involves photodissociation of physisorbed molecules on insulating substrates, for which better known gas

phase potential energy surfaces are a good starting point and quenching by the substrate can be neglected.

In principle, the validity of a dynamical model can be checked by adjusting any unknown parameters to see if agreement between calculated and measured final state distributions can be obtained, in which case the fitted parameters can provide useful information about the desorption / reaction mechanism. Clearly, the results of such a procedure are meaningful only if the number of adjustable parameters is kept small enough to avoid overrating of the data. In the absence of additional information, such as reliable theoretical potential energy surfaces, this requirement tends to conflict with the rather large number of unknown parameters encountered in all but the simplest models. Interestingly, however, extremely simple models often prove sufficient to explain many features of the observed final state distributions, thus providing physical insight and serving as a starting point for more sophisticated dynamical models.

Two major classes of detection methods can be distinguished: mass spectrometric time-of-flight (TOF) techniques and laser spectroscopic methods. The former can provide translational (angular and velocity) distributions, whereas the latter are used to obtain both translational and internal state distributions. Compared with laser spectroscopy, mass spectrometry is not only a simpler, but also a more versatile technique, since all molecules can be detected in this way. As a consequence, there is much more data available about translational distributions of photodesorbed molecules than there is about internal state distributions. In contrast to TOF measurements, internal state resolved studies of surface photochemistry have for some time been limited to a single desorbed species (NO) [33][53-76], mostly because of its relative ease of detection due to conveniently located electronic excited states. Recently, a second product molecule (CO) has been studied in this way [77-85] and vibrationally (but not rotationally) resolved spectra of CD_3 and spin-orbit resolved spectra of atomic iodine photofragments have been obtained [86-88]. The author detected NO fragment with REMPI technique in this experiment.

References

[1] T. J. Chuang, Surf. Sci. **178**, 763 (1986)

[2] W. Ho, Comments Condens. Mater. Phys. **13**, 293 (1988)

[3] Ph. Avouris and R. E. Walkup, Annu. Rev. Phys. Chem. **40**, 173 (1989)

[4] W. Ho, in: Desorption Induced by Electronic Transitions, DIET IV, Eds. G. Betz and P. Varga (Springer, Berlin, 1990) p. 48; Res. Chem. Interm. 17, 27 (1992)

[5] J. M. White, in: Chemistry and Physics of Solid Surfaces VIII, Eds. R. Vanselow and R. Howe (Springer, Berlin, 1990) p. 29

[6] J. C. Polanyi and H. Rieley, in: Dynamics of Gas-Surface Interactions, Eds. C. T. Rettner and M. N. R. Ashfold (Royal Society of Chemistry, Cambridge, 1991) p. 329

[7] H. –L. Dai and W. Ho, Eds., Laser Spectroscopy and Photochemistry on Metal Surfaces, Advances in Physical Chemistry Series (World Scientific, Singapore, 1995)

[8] E. Hasselbrink, Appl. Phys. A **53**, 403 (1991)

[9] X. –L. Zhou, X. –Y. Zhu and J. M. White, Surf. Sci. Rep. **13**, 73 (1991)

[10] L. J. Richter and R. R. Cavanagh, Prog. Surf. Sci. **39**, 155 (1992)

[11] R. R. Cavanagh, D. S. King, J. C. Stephenson and T. F. Heinz, J. Phys. Chem. **97**, 786 (1993)

[12] J. W. Gadzuk, in: Laser Spectroscopy and Photochemistry on Metal Surfaces, Eds. H. L. Dai and W. Ho, Advances in Physical Chemistry Series (World Scientific, Singapore, 1995)

[13] W. Ho, in: Laser Spectroscopy and Photochemistry on Metal Surfaces, Eds. H. –L. Dai and W. Ho, Advances in Physical Chemistry Series (World Scientific, Singapore, 1995)

[14] R. M. Osgood and H. H. Gilgen, Annu. Rev. Mater. Sci. **15**, 549 (1985)

[15] D. J. Ehrlich and J. Y. Tsao, Eds., *Laser Microfabrication*: Thin Film Processes and Lithography (Academic Press, San Diego, CA, 1989)

[16] I. P. Herman, Chem. Rev. **89**, 1323 (1989)

[17] D. P. Kern, T. F. Kuech, M. M. Oprysko, A. Wagner and D. E. Eastman, Science **241**, 936 (1988)

[18] D. Bäuerle, Appl. Phys. B **46**, 261 (1988)

[19] C. I. H. Ashby, in :*Thin Film Processes II*, Eds. J. L. Vossen and W. Kern (Academic Press, Boston, MA, 1991) p.783
[20] J. G. Eden, in: *Thin Film Processes II*, Eds. J. L. Vossen and W. Kern (Academic Press, Boston, MA, 1991) p. 443
[21] Sz. Fujita and Sg. Fujita, Appl. Surf. Sci. **79/80**, 41 (1994)
[22] M. C. Shih, M. B. Freiler, R. Scarmozzino and R. M. Osgood, Jr., J. Vac. Sci. Technol. B **13**, 43 (1995)
[23] J. A. Barker and D. J. Auerbach, Surf. Sci. Rep. **4**, 1 (1985)
[24] G. Comsa and R. David, Surf. Sci. Rep. **5**, 145 (1985)
[25] M. C. Lin and G. Ertl, Annu. Rev. Phys. Chem. **37**, 587 (1986)
[26] D. S. King and R. R. Cavanagh, in: Molecule Surface Interactions, Ed. K. P. Lawley (Wiley, New York, 1989) p. 45
[27] P. L. Houston and R. P. Merrill, Chem. Rev. **88**, 657 (1988)
[28] H. Zacharias, Int. J. Mod. Phys. B **4**, 45 (1990)
[29] J. A. Prybyla, T. F. Heinz, J. A. Misewich and M. M. T. Loy, Surf. Sci. **230**, L172 (1990)
[30] S. F. Shane, H. A. Michelsen and R. N. Zare, in: Laser Spectroscopy and Photochemistry on Metal Surfaces, Eds. H. –L. Dai and W. Ho, Advances in Physical Chemistry Series (World Scientific, Singapore, 1995)
[31] E. Hasselbrink, Chem. Phys. Lett. **170**, 329 (1990)
[32] J. W. Gadzuk, Phys. Rev. B **44**, 13466 (1991)
[33] T. Mull, B. Baumeister, M. Menges, H. –J. Freund, D. Weide, C. Fischer and P. Andresen, J. Chem. Phys. **96**, 7108 (1992)
[34] B. Baumeister and H. –J. Freund, J. Phys. Chem. **98**, 11962 (1994)
[35] E. Hasselbrink, in: Lasser Spectroscopy and Photochemistry on Metal Surfaces, Eds. H. L. Dai and W. Ho, Advances in Physical Chemistry Series (World Scientific, Singapore, 1995)
[36] M. Messina and R. D. Coalson, J. Chem. Phys. **95**, 8977 (1991)
[37] J. C. Polanyi and R. J. Williams, J. Chem. Phys. **88**, 3363 (1988)
[38] M. I. McCarthy and R. B. Gerber, J. Chem. Phys. **93**, 887 (1990)
[39] H. Guo and G. C. Schartz, J. Chem. Phys. **94**, 379 (1991)
[40] M. I. McCarthy, R. B. Gerber, K. A. Trentelman, P. Strupp, D. H. Fairbrother, P. C. Stair and E. Weitz, J. Chem. Phys. **97**, 5168 (1992)

[41] J. M. Watson, I. NoorBatcha and R. R. Lucchese, J. Chem. Phys. **96**, 7771 (1992)
[42] Z. –H. Huang and H. Guo, J. Chem. Phys. **96**, 8564 (1992)
[43] Z. –H. Huang and H. Guo, J. Chem. Phys. **96**, 2110 (1992)
[44] V. J. Barclay, J. C. Polanyi, Y. Zeiri and R. Kosloff, J. Chem. Phys. **98**, 9185 (1993)
[45] R. Kosloff and Y. Zeiri, J. Chem. Phys. **97**, 1719 (1992)
[46] Z. –H. Huang and H. Guo, J. Chem. Phys. **98**, 3395 (1993)
[47] J. –Y. Fang and H. Guo, J. Chem. Phys. **101**, 1231 (1994)
[48] M. Hintenender, F. Rebentrost, R. B. Gerber and R. Kosloff, J. Chem. Phys. **102**, 578 (1995)
[49] T. Seideman, J. Chem. Phys. **99**, 4766 (1993)
[50] F. M. Zimmermann and W. Ho., J. Chem. Phys. **101**, 5313 (1994)
[51] C. Springer, M. Head-Gordon and J. C. Tully, Surf. Sci. **320**, L57 (1994)
[52] F. Dzegilenko, E. Herbst and T. Uzer, J. Chem. Phys. **102**, 2593 (1995)
[53] W. C. Natzle, D. Padowitz and S. J. Sibener, J. Chem. Phys. **88**, 7975 (1988)
[54] L. M. Cousins, R. J. Levis and S. R. Leone, J. Phys. Chem. **93**, 5325 (1989)
[55] J. Heidberg, W. Class, H. –C. Langowski, M. Suhren and M. Warskulat, in: Desorption Induced by Electronic Transitions, DIET IV, Eds. G. Betz and P. Varga (Springer, Berlin, 1990) p. 213
[56] D. Weide, P. Andresen and H. –J. Freund, Chem. Phys. Lett. **136**, 106 (1987)
[57] F. Budde, A. V. Hamza, S. Jakubith, D. Weide, P. Andresen and H. –J. Freund, Surf. Sci. **218**, 467 (1989)
[58][71] P. M. Ferm, F. Budde, A. V. Hamza, S. Jakubith, D. Weide, P. Andresen and H. –J. Freund, Surf. Sci. **218**, 467 (1989)
[59] T. Mull, M. Menges, B. Baumeister, G. Odörfer, H. Geisler, G. Illing, R. M. Jaeger, H. Kuhlenbeck, H. –J. Freund, D. Weide, U. Schüller, P. Andresen, F. Budde, P. Ferm, V. Hamza and G. Ertl, Phys. Scr. **41**, 134 (1990)
[60] M. Menges, B. Baumeister, K. Al-Shamery and H. –J. Freund, J. Chem. Phys. **101**, 3318 (1994)
[61] I. J. Richter, S. A. Buntin, R. R. Cavanagh and D. S. King, J. Chem. Phys. **89**, 5344 (1988)

[62] K. Mase, K. Fukutani and Y. Murata, J. Chem. Phys **96**, 5523 (1992)
[63] St. J. Dixon-Warren, J. C. Polanyi, H. Rieley, J. G. Shapter and H. Weiss, J. Phys. Chem. **96**, 10983 (1992)
[64] R. Schwarzwald, A. Mödl and T. J. Chuang, Surf. Sci **242**, 437 (1991)
[65] L. J. Richter, S. A. Buntin, D. S. King and R.R. Cavanagh, J. Chem. Phys. **96**, 2324 (1992)
[66] K. Mase and Y. Murata, Prog. Theor, Phys. Suppl. **106**, 349 (1991)
[67] K. Fukutani, Y. Murata, R. Schwarzwald and T. J. Chuang, Surf. Sci. **311**, 247 (1994)
[68] D. Burgess, Jr., R. R. Cavanagh and D. S. King, J. Chem. Phys. **88**, 6556 (1988)
[69] S. A. Buntin, L. J. Richter, D. S. King and R. R. Cavanagh, J. Chem. Phys. **91**, 6429 (1989)
[70] E. Hasselbrink, S. Jakubith, S. Nettesheim, M. Wolf, A. Cassuto and G. Ertl, J. Chem. Phys. **92**, 3154 (1990)
[71] J. A. Prybyla, T. F. Heinz, A. Kalamarides, M. M. T. Loy and J. A. Misewich, Surf. Sci. **283**, 143 (1993)
[72] F. Budde, T. F. Heinz, A. Kalamarides, M. M. T. Loy and J. H. Glownia, Phys. Rev. Lett. **64**, 1537 (1990)
[73] H. Ferkel, L. Hdggson, J. T. Singleton, P. M. Blass, H. Reisler and C. Wittig, J. Chem. Phys. **100**, 9228 (1994)
[74] C. Ning and J. Pfab, Chem. Phys. Lett. **216**, 87 (1993)
[75] Y. Murata and K. Fukutani, in: Laser Spectroscopy and Photochemistry on Metal Surfaces, Eds. H. –L. Dai and W. Ho, Advances in Physical Chemistry Series (World Scientific, Singapore, 1995)
[76] R. C. Jackson, J. C. Polanyi and P. Sjövall, J. Chem. Phys. **102**, 6308 (1995)
[77] F. M. Zimmermann, L. L. Springsteen, M. Asscher, P. L. Houston and W. Ho, to be published
[78] S. A. Buntin, R. R. Cavanagh and L. J. Richter, J. Chem. Phys. **98**, 7651 (1993)
[79] P. M. Chu, S. A. Buntin, L. J. Richter and R. R. Cavanagh, J. Chem. Phys. **101**, 2929 (1994)

[80] P. M. Chu, S. A. Buntin, L. J. Richter and R. R. Cavanagh, Surf. Sci. **321**, 127 (1994)
[81] A. Peremans, K. Fukutani, K. Nase and Y. Murata, Surf. Sci. **283**, 189 (1993)
[82] K. Al-Shamery, I. Beauport, H. –J. Freund and H. Zacharias, Chem. Phys. Lett. **222**, 107 (1994)
[83] J. Kutzner, G. Lindeke, K. H. Welge and D. Feldmann, J. Chem. Phys. **90**, 548 (1989)
[84] K. A. Trentelman, D. H. Fairbrother, P. G. Strupp, P. C. Stair and E. Weitz, J. Chem. Phys. **96**, 9221 (1992)
[85] D. H. Fairbrother, K. A. Briggman, P. C. Stair and E. Weitz, J. Chem. Phys. **102**, 7267 (1995)
[86] J. Kutzner, G. Lindeke, K. H. Welge and D. Feldmann, J. Chem. Phys. **90**, 548 (1989)
[87] K. A. Trentelman, D. H. Fairbrother, P. G. Strupp, P. C. Stair and E. Weitz, J. Chem. Phys. **96**, 9221 (1992)
[88] D. H. Fairbrother, K. A. Briggman, P. C. Stair and E. Weitz, J. Chem. Phys. **102**, 7267 (1995)

4.2 Experimental

4.2.1 Resonance enhanced multi-photoionization technique on surface photochemistry

Basic mechanisms of the surface excitation

Photon irradiation of a surface inevitably results in some degree of surface heating, which can open up pathways for thermally activated (pyrolytic) surface reactions [1-2]. When investigating photon induced surface processes, both thermal and photochemical mechanisms should therefore be considered. Knowledge of the peak surface temperature helps to determine if thermal processes are likely to play a role. In the case of continuous wave (cw) irradiation, the temperature rise can be easily measured [2-3]. Nanosecond laser pulses, on the other hand, cause a transient surface temperature rise that requires sophisticated measurement techniques with nanosecond or picosecond time resolution [4-6]. In practice, one therefore often relies on laser heating models [6-8] to calculate the temperature rise. If the thermophysical properties of the substrate do not appreciably depend on temperature, analytical solutions [7-9] to the heat diffusion equation can be used, otherwise numerical simulations [6, 10] are necessary. The calculation method by using the heat diffusion equation is described in the section 4.2.4. For laser induced thermal desorption (LITD), the expected desorption yield can then be estimated from the peak surface temperature if the kinetic parameters are known [9]. The rate of a thermally activated reaction depends exponentially on the inverse temperature, which is reflected in the dependence of the LITD yield on the absorbed fluence and the substrate base temperature. This strongly super linear fluence dependence (as long as no saturation occurs due to surface depletion) is in sharp contrast to the linear fluence dependence that is expected (and observed) for most single-photon photochemical reactions, and is used to distinguish thermal from photochemical mechanisms [11, 12]. One has to keep in mind, however, that photochemical mechanisms involving multi-photon processes or multiple electronic excitations also lead to a super linear fluence dependence [13-16]. In addition to the fluence dependence, the product state distributions can help distinguish between pyrolytic and photolytic channels, especially if both mechanisms are operating simultaneously and the resulting distributions are bimodal as a consequence [11, 12, 17]. In the absence of

appreciable barriers to adsorption [18], thermally desorbed molecules are usually characterized by thermal energy distributions with temperatures comparable to [17, 19] or lower than [20-22] the surface temperature at the time of desorption (see Ref. [23] for a review). On the other hand, translationally or internally highly excited molecules (as compared to the surface temperature) are usually indicative of photochemical mechanism, in particular if the energy distributions are independent of the absorbed fluence [17, 24, 25]. However, it is important to keep in mind that in the presence of an adsorption barrier, thermal desorption can also lead to translationally or internally highly excited products [26, 27]. Translationally very cold desorbing photofragments, although not typical, have also been observed [28]. Dynamical models of thermal surface processes have recently been reviewed by Lombardo and Bell [29], and Brivio and Grimley [30].

Distinguishing thermal effects from photochemical mechanisms is rather straightforward for visible and UV light exciting the absorbing system electronically than for irradiation in the infrared. Any reaction induced by such an excitation before thermalization of the energy occurs is considered photochemical. Reaction inducing photons may be absorbed by adsorbate molecules directly, in which case one speaks of a “direct” excitation mechanism, or by the substrate, defining an “indirect” or “substrate mediated” excitation mechanism. In a direct mechanism, adsorbed molecules are either excited by resonant valence excitation without changing the molecule’s charge state, such as in the case of $Mo(CO)_6$ photodissociation on Si(111)7x7 [31-33], or they are photoionized, resulting in a positively charged excited state, as proposed for CO/Pt(111) [14][34]. If the hole created by direct valence excitation of an adsorbed molecule is efficiently screened (or filled) by substrate electrons, the excited state can also correspond to a negatively charged molecule. Another conceivable direct excitation mechanism is the photoexcitation of the adsorbate-substrate bond, e.g., transition of an electron from a bonding to an anti-bonding orbital. Such an excitation could have charge transfer character and thereby also lead to charged excited states.

In substrate mediated photoprocesses, electronic excitations (electrons, holes, or excitons) created in the substrate by photon absorption travel to the surface and induce reaction by localizing on the adsorbate or the adsorbate-

substrate complex. This implies that only excitations created within a distance from the surface of the order of the excitation's inelastic mean free path (which can be several 100 Å) are photochemically effective [33]. In most cases, photon absorption creates energetic electron-hole pairs via band gap excitation as the initial electronic excitations. These photogenerated carriers (electrons or holes) are thought to be responsible for many photoprocesses on semiconductor surfaces [33,35-38]. Similarly, many photochemical reactions on metal surfaces have been attributed to photoexcited or "hot" electrons, such as NO photodesorption from Pt(111) [39-41], O_2 photodesorption and photodissociation on Pd(111) [42], and SO_2 photodesorption from Ag(111) [43]. Energetic carriers can transfer their energy to adsorbed molecules by localizing on the molecule (forming temporary positive or negative ion states [37,39,41]) or on the molecule-surface bond, or by electronic- electronic energy transfer without charge transfer [44-46]. If dissociation of an adsorbed molecule is induced by electron transfer from the substrate to an adsorbate affinity level, one speaks of charge-transfer photodissociation (CT/PDIS) or photoinduced dissociative electron attachment (DEA) [33, 47-52]. Although less frequently invoked in discussions of substrate mediated mechanisms than electron attachment, electron transfer from the adsorbate to the substrate through capture of a photoexcited substrate hole is another possible excitation mechanism for photoinduced processes on metal or semiconductor surfaces [37].

Direct excitation mechanisms can often be distinguished from substrate mediated mechanisms by comparing the photon energy dependence of the reaction yield with that of the substrate's absorbance or the adsorbate photochemistry in the gas phase [33][37]. A number of recent studies have also used the polarization and angle-of-incidence dependence to investigate this question, claiming that the results are incompatible with direct excitation [40, 41, 47, 53-55]. It has been pointed out, however, that the conclusions were based on an incorrect analysis of the data [56]. If carried out correctly, the adopted approach can identify a direct mechanism if the transition moment is perpendicular to the surface (because, in contrast to substrate mediated mechanisms, the photoyield is then predicted to be zero at normal incidence), but for substrates with a large imaginary part of the dielectric function ε_2 (such

as metals, as well as semiconductors at photon energies exceeding the direct band gap), the method can not distinguish between a substrate mediated mechanism and a direct excitation with a transition moment parallel to the surface [37][56].

However, polarization and angle-of-incidence dependencies have been employed in two alternative methods to clearly distinguish between substrate mediated and direct excitation mechanisms. One involves the polarization dependence of the photoyield at normal incidence, and was applied to O_2 photodesorption / dissociation on Ag(110) [57][58]. Making use of the known adsorption geometry and the twofold symmetry of the (110) surface, a substrate-mediated mechanism could be established for this system. The other method compared the incidence-angle dependence of the photoyield of SO_2 photodesorption from a quartz prism, irradiated from the backside [59]. The desorption yield exhibited a cusp at the angle for total internal reflection and could be nicely fit with the calculated squared electric field at the surface, which clearly established a direct excitation mechanism. After evaporation of a 300 Å thick Ag film onto the prism, the SO_2 photodesorption signal was not only substantially reduced, but could no longer be fit by the calculated electric field. Instead, the photoyield followed the absorbance in the Ag film, revealing a substrate-mediated mechanism.

Another importance characteristic of substrate mediated, photoexcited carrier mechanisms is the independence (or at most weak dependence) of the final state energy distributions on the photon energy [36, 41, 42], and SO_2 photodesorption from Ag(111) [43, 52, 54, 60, 61], as long as the limit imposed on the energy disposal by the available energy (photon energy less binding energy) remains high enough to not appreciably affect the distributions. In direct photoexcitation processes, on the other hand, the desorbed products are much more likely to retain some memory of the energy of the incident photons [60][62]. This difference can be rationalized by the fact that in metals, photoexcited electrons quickly lose their energy to other electrons ("hot electron cascades" [70]) resulting in a broad distribution of excitation energies, and semiconductors, electron-phonon scattering eventually leads to photoexcited, but "thermalized" carriers at the band edges [52, 60], depriving the electron distribution of any information about the photon energy. Since only those

carriers that are resonant with adsorbate state or adsorbate-substrate bonds induce photochemistry, the final state distributions are mostly determined by the electronic structure of the adsorbate-substrate system, not the photon energy. In direct photoexcitation, on the other hand, the photon energy determined which vibrational/rotational/translational sublevels of the electronic excited state are accessed, affecting the final state distributions.

Following either direct or indirect excitation, the adsorbate-substrate complex is in an electronically excited state. The mechanism by which this electronic energy is thought to couple to nuclear motion in the reaction coordinates can be illustrated with the model for desorption from a metal surface [80][81]. In this model (see Fig. 4-1), the adsorbate-substrate complex first undergoes a sudden (Franck-Condon) transition to the excited state,

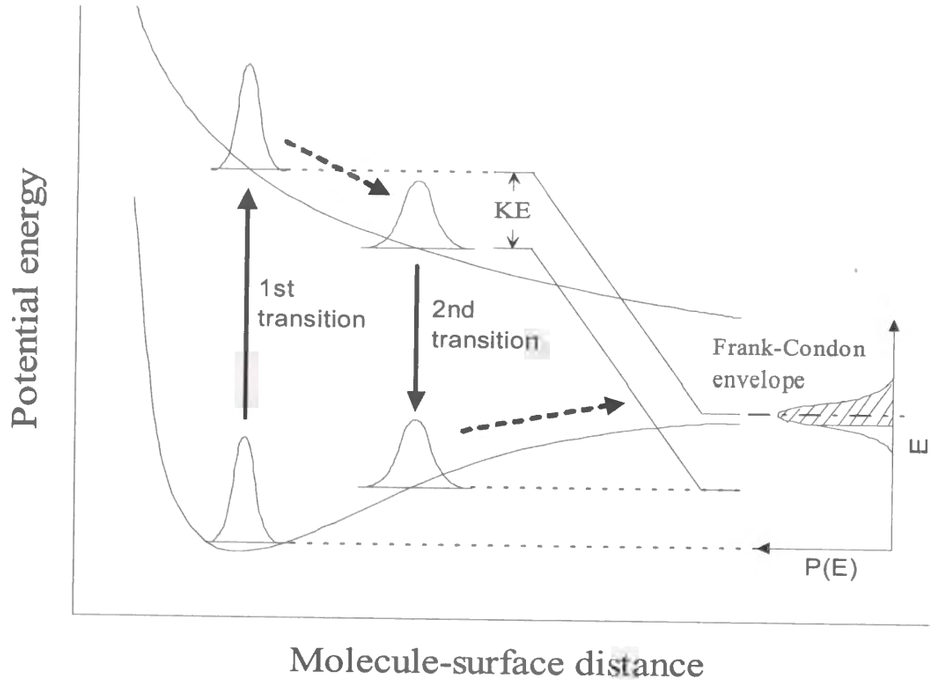

Fig. 4-1 Schematic of a Menzel-Gomer-Redhead (MGR) desorption process. A Frank-Condon transition is thought to excite the system from the ground state potential energy surface (PES) to an electronically excited state, where it evolves subject to the forces of the excited state PES, gaining kinetic energy KE, until a second Frank-Condon transition brings it back to the ground state PES (quenching). Gaussian wave packets schematically indicate the nuclear probability density at various stages of the process. The final energy distribution P(E) for a given residence time in the excited state is sketched on the right. Components of the wave function that project onto continuum states (hatched) in the quenching transition correspond to desorbing particles, others remain trapped.

followed by adiabatic time evolution on the excited state potential energy surface (PES). Because the excited state PES will in general not have a minimum at the ground state equilibrium configuration of the nuclei (the chemical bond is expected to be substantially perturbed in the excited state), the adsorbate nuclei will accelerate in response to the resulting forces. Although in the original MGR model the excited state was assumed to be purely repulsive, the model can be readily generalized to apply to different excited state potential energy surfaces [65].

As a result of the geometry change the nuclei gain kinetic energy, and in addition, the nuclear wave packets broaden or contract. Depending on the electronic structure of the surface, nonradiative energy transfer to the substrate many quickly quench the electronic excited state, creating an electronic substrate excitation in the process. In the MGR picture, this electronic quenching is modeled as a second Frank-Condon transition back to the ground state PES. Since the wave packet has moved while in the excited state, it finds itself displaced from the equilibrium configuration upon returning to the ground state. Therefore, in addition to the kinetic energy gained during acceleration on the excited state PES, the system has also gained some potential energy. The final state of the MGR model is actually characterized by a distribution of energies, which is given by the Franck-Condon envelope (i.e., the curve defined by the Franck-Condon factors for the various final states) of the second transition. If the total energy gained in the reaction coordinate exceeds the adsorption energy, desorption occurs. In Fig. 4-1, the hatched portion of the final energy distribution represents the continuum states, i.e., states with sufficient energy to desorb. A wave packet dynamics calculation of photodesorption based on this sudden-switching model can be found in Ref. [66].

It was first pointed out by Antoniewicz [65] that the excited state PES for desorption in a MGR-type model does not have to be repulsive in the desorption coordinate. An excited state potential energy curve that is attractive at the ground state equilibrium distance will accelerate the molecule toward the surface. If quenching occurs after sufficient energy has been gained, the molecule will be reflected from the surface and desorb. In cases where the attractive force in the excited state is due to the image potential of a temporary

positive ion, this scenario for desorption of neutrals is referred to as Antoniewicz mechanism. In contrast to a repulsive MGR picture, the de-excitation (neutralization) step is essential in this model, since the positive ion cannot overcome the image attraction on the excited state curve. This mechanism has been extensively applied to model electron stimulated desorption of physisorbed species [67-69].

In the above model, transitions between the electronic ground and excited states occur suddenly, and we therefore refer to it as the "sudden-switching" model. It describes an idealized situation in which the system suddenly switches to a different potential energy surface and the nuclear wave function remains unchanged during the switch, i.e., the energy eigenstates of the new Hamiltonian are coherently excited, with probabilities given by the Franck-Condon factors (squared overlap integrals between the initial wave function and the new eigenstates).

Due to the step-function-like switch to a new Hamiltonian, the model concept of such a sudden transition implies that all frequencies are involved in the transition. This is a reasonable approximation for direct excitation by ultrashort (~ a few fs) lasers pulses with a transform limited spectral width that exceeds the energy width of the Frank-Condon envelope for the transition [70]. If the excited state is very short-lived, lifetime broadening can also supply the necessary energy width to populate different levels within the Frank-Condon envelope. For direct excitation of a long-lived excited state by a monochromatic laser, however, the sudden approximation as described above is not applicable. Amore realistic description of monoenergetic excitation would have to project the appropriate energy component out of the "sudden-switching" wave function. If a broad distribution of excitation energies is available (such as incoherent broadband light irradiation, or excitation by a broad distribution of "hot" substrate electrons), the result is an incoherent mixture of these energy eigenstates, weighted by their Frank-Condon factors.

In the second (quenching) transition of the MGR model, such a projection of the wave function onto a particular energy component is not necessary, since a range of final energies can be accessed without violating energy conservation. This is due to the electronic substrate excitation created in the quenching process, which will have an energy distribution (also given by

the Frank-Condon envelope) to compensate for the energy spread introduced by the sudden transition in the nuclear degrees of freedom (i.e., the total energy is constant). However, a less simplistic model should obviously not use a fixed residence time in the excited state, but should rather consider a quenching rate (a transition probability, which may depend state, but should rather consider a quenching rate (a transition probability, which may depend on the nuclear coordinates), resulting in a distribution of residence times. Observed quantities such as the final state energy distributions are then given by the predictions of the sudden switching model, averaged over this distribution of excited-state residence times [71].

The substrate plays two important roles in surface photochemistry: Not only does it modify the electronic structure and inter-atomic potentials in much the same way as it does in other surface reactions, i.e., it aligns and orients reactants, brings them in close contact with each other, weakens certain bonds, etc., but in addition it opens new energy transfer channels, for both excitation (i.e., substrate mediated mechanisms) and for quenching. Excited state quenching can compete with reaction by effectively depriving the system of the photochemical energy needed to overcome activation barriers. In this way, the quenching efficiency (on the time scale for bond cleavage) determines the reaction probability and can influence the product energy distributions.

Efficient quenching can, of course, occur only if the substrate has excited states available that match the excitation energy of the adsorbate excitation to be quenched. For this reason, insulating materials such as LiF are popular choices for substrates. Their wide band gap energy can effectively preclude excited state quenching for excitation energies below the band gap energy, assuming the bulk substrate excitation spectrum is not appreciably modified by additional electronic states within the gap (which can be due to the presence of the surface itself, adsorbates, impurities or other defects).

There are different mechanisms by which electronic excitation energy can be transferred from the adsorbate to the substrate. Excited states of the adsorbate involving occupied orbitals above or unoccupied orbitals below the Fermi level can be efficiently quenched by resonant electron tunneling to or from degenerate substrate states, respectively. Characteristic time scales for resonant tunneling processes can be estimated from the widths of electronic

adsorbate levels that lie in resonance with a substrate band, as determined from photoemission or inverse photoemission studies. Such resonance widths (which actually give only lower limits for the lifetime, since photoemission peaks of localized states can be broadened due to vibrational excitation of the final state, the vibrational width being given by the Franck-Condon envelope), are typically on the order of a few hundred meV to 1 eV for chemisorbed molecules [72-74]. This is in good agreement with resonance widths obtained in electronic structure calculations [75], which do not suffer from the ambiguities introduced by vibrational or inhomogeneous broadening. Widths of ~1 eV correspond to resonance lifetimes on the order of 10^{-15} s. If an excited orbital is not resonant with any substrate levels (by being located in a gap of the substrate, e.g., below the valence band of a metallic substrate), the resonant tunneling channel is blocked. In this case, quenching can occur through non-resonant electron tunneling processes, in which energy is transferred to a substrate electron. Such relaxation processes involving more than one electron, called Auger processes, are much slower (~10^{-13} s) than resonant tunneling [76, 77]. Excited states for which resonant quenching channels are blocked are therefore relatively long-lived and, as a consequence, likely to result in bond breaking [76]. Excited states with the same charge as the ground state (intermolecular excitations) can be quenched via electric field coupling to the substrate [78], or by simultaneous electron tunneling from the excited adsorbate level to the substrate and from the substrate to the valence hole on the adsorbate. Lifetimes of such neutral excited states of adsorbate molecules on metal or oxide surfaces are also on the order of a few femtoseconds [79, 80]. If the excited state PES is steep enough, dissociation or desorption can compete with all these quenching mechanisms, since the time scale for bond cleavage on a repulsive surface is on the order of 10^{-14} s. It should also be noted that de-excitation by emission of a photon cannot normally compete with quenching or bond breaking because typical fluorescence lifetimes (~10^{-8} s) are much longer than quenching or bond-breaking time scales.

The presence of multilayers of adsorbate often opens up an additional channel for photoinduced desorption, called "photoejection" [46, 81]. Molecules desorbed through this channel are characterized by very high translational

energies. It is interpreted as direct electronic to vibrational, rotational and translational energy transfer. Specifically, an electronically excited adsorbate molecule (following direct photon absorption) is thought to be quenched to the ground state by a close encounter with another adsorbate molecule. If the intermolecular potential energy curve in the excited state is much less repulsive than that of the electronic ground state, the two curves may cross at a point accessible to the interacting pair of molecules. Internal conversion to the ground state at this point would place the system high up on the repulsive part of the ground state potential, which may lead to ejection of at least one of the molecules if the quenching takes place near the topmost adsorbate layer. Considering the full multidimensional potential surfaces, the rotational and vibrational degree of freedom can take up a portion of the electronic energy in a similar fashion.

Experimental measurement techniques for a time-of-flight spectrum

A typical apparatus for state resolved surface photochemistry experiments consists of an ultrahigh vacuum system, a photochemical light source and a detection system for desorbed products. The sample crystal is mounted inside the vacuum chamber with standard provisions for sample temperature control, surface cleaning, surface characterization, and gas dosing. Pulsed lasers are usually chosen as photochemical light sources because pulsed desorption is of advantage in conjunction with laser spectroscopic detection (using pulsed detection lasers), and because their good time resolution makes them ideally suited for time-of-flight (TOF) measurements. Arc lamp experiments can provide useful complementary information (wavelength dependence) bearing on the excitation mechanism. Two classes of detection schemes are commonly used: Detection using mass spectrometers can provide angular and TOF information, whereas laser spectroscopic detection schemes can in addition probe specific internal states of the desorbing molecules.

If desorption is induced by laser pulses with a short enough pulse width, velocity distributions of desorbed particles can be determined by measuring the distribution of flight times between desorption and detection. Since the pulse widths of most pulsed lasers is of the order of 10-20 ns or shorter, during which

time a typical desorbing molecule will move only tens of microns, the velocity resolution of such TOF measurements is usually limited by the finite spatial extent of the detector. The most commonly used detector consists of a quadrupole mass spectrometer (QMS)[82] with a spatially very localized ionizer (to define the flight distance) and time-resolved pulse counting electronics. This set-up has the advantage that the mass information is clearly separated from the velocity information (which is important if several species of different mass desorbed), and that it can detect neutral species as well as ions (by turning off the ionizer). Care has to be taken to properly subtract the drift time through the ion optics and the quadrupole mass filter from the total measured flight time. When analyzing the spectra, it has to be kept in mind that not all detected species are necessarily desorbed products, since cracking fragments produced in the ionizer contribute to the signal. In contrast to laser spectroscopic techniques, QMS detection is easily applicable to all desorbed species.

A simpler method to measure velocity distributions is use a (modified) time-of-flight mass spectrometer (TOF-MASS) [82], which measures the drift time of ionic species between ionization and detection. In mass spectrometer mode, the ions are accelerated into a field-free drift tube, giving all of them approximately the same translational energy, such that the species' masses can be determined from the flight time. Velocity distributions can be obtained by applying no (or, if the mass is known, a small) accelerating voltage in front of the drift tube. Since no mass filter is used, this method can be more sensitive than detection by a QMS. In its simplest form, it is applicable only to the detection of desorbed ions [83]. In conjunction with a pulsed ionizer, the TOF-MS may also be used for velocity measurements of neutrals desorbed by a cw light source. If ionization is achieved with a tunable laser through resonance enhanced multiphoton ionization (REMPI), the technique can provide internal state information as well [84, 85]. Mass spectrometric detection methods are reviewed in Ref. [82].

If a mass spectrometer is used with an electron impact ionizer to detect neutral particles, the detector signal is proportional to the number density of mass selected particles in the ionization region. A measured TOF spectrum therefore represents the particle density at the detector as a function of flight time. The same is true for quantum state specific TOF spectra measured using

laser spectroscopic techniques. In order to derived the simple transformation that extracts the velocity distribution from the TOF spectrum, it is crucial to note that for such "density" detectors the signal as a function of flight time does not represent the distribution (A distribution in the variable x is a function f(x) for which dN = f(x) dx, i.e., the area underneath any given section of the curve is proportional to the number of particles in that x-interval.) of flight times, since the signal S(t) is proportional to the number density $\rho(r, t)$, which is a distribution in space, not in time (The number density ρ is the spatial distribution in Cartesian coordinates. The quantity $r^2\rho(r)$ is the distribution in the flight distance r, since for desorption from a point into the solid angle element $d\Omega$, we have $dN = \rho(r)\, r^2\, d\Omega\, dr$.) To see that the "density" signal does not represent the distribution of flight times (the TOF distribution) one needs to realize that faster molecules spend less time in the ionizer than slow molecules and are therefore less likely to be detected. We therefore refer to the signal S(t) as the TOF spectrum, not the TOF distribution. The TOF distribution is given by the flux $I = v\rho$ (density ρ weighted by velocity v), i.e., the number of molecules that pass through a certain area per unit time. The TOF distribution (flux versus time) $I(t)=v\rho(t) \propto t^{-1}S(t)$ is straightforwardly converted to a velocity (or speed; the term "velocity" technically applies to the vector quantity v, with the speed v as a its modulus. However in accord with common usage, we do not always make this distinction, and use both terms "velocity" and "speed" for v) distribution $P_v(v)$ by setting $I(t)dt = P_v(v)dv$, and using the Jacobian $|dv/dt| = r/t^2$, where r is the flight distance:

$$P_v(v) = \frac{t^2}{r} I(t) \propto \frac{1}{v} S(t), \qquad (4.1)$$

with t = r/v [86]. Similarly, one obtains for the translational energy distribution

$$P_E(E_t) = \frac{t^3}{m} I(t) \propto \frac{1}{E_t} S(t), \qquad (4.2)$$

with $t = r(m/2E_t)^{1/2}$.

Translational energy distributions are often characterized by the mean translational energy $\langle E_t \rangle$ and a "reduced width" w describing the distribution's spread [87]. These and other quantities can be conveniently determined from

the experimental density signal S(t) by numerical integration if one introduces the moments of the (normalized) velocity distribution $P_v(v)$

$$M_n = \int v^n P_v(v)dv = \frac{r^n \int t^{-(n+1)} S(t)dt}{\int t^{-1} S(t)dt}. \qquad (4.3)$$

In terms of these moments, the mean translational energy can be expressed as

$$\langle E_t \rangle = \int_0^\infty E_t P_v(v)dv = \frac{1}{2} m M_2, \qquad (4.4)$$

the mean velocity is given by ⟨v⟩=M1, and the reduced width w is calculated using

$$1 + \frac{w^2}{2} = \frac{\langle E_t^{\,2} \rangle}{\langle E_t \rangle^2} = \frac{M_4}{(M_2)^2}. \qquad (4.5)$$

In this context, we should point out a frequent source of confusion related to "flux weighting". Formulas describing velocity distributions or TOF spectra change their prefactor by one power of the velocity v if they refer to a flux rather than a density of molecules. Such additional factors of v are an issue at the outset (when the distribution is produced, e.g., by effusion), or during detection (flux versus density detection), or both. These two sources of factors of v are completely independent, and should not be confused with each other. For example, consider a gas of non-interacting molecules in thermal equilibrium at temperature T. The velocity distribution of the molecules in a given volume is a "density" Maxwell-Boltzmann distribution

$$P_v(v)dv = 4\pi \left(\frac{m}{2\pi kT} \right)^{3/2} v^2 \exp\left(-\frac{mv^2}{2kT} \right) dv, \qquad (4.6)$$

$$P_E(E_t)dE_t = \frac{2}{\sqrt{\pi}kT} \left(\frac{E_t}{kT} \right)^{1/2} \exp\left(-\frac{E_t}{kT} \right) dE_t, \qquad (4.7)$$

also called a "v^2 Maxwell distribution" in the terminology of Ref. [88]. As a thought experiment, consider preparing such a distribution for a TOF measurement by suddenly removing the walls of the gas's container at t = 0. TOF spectra recorded at a distance large compared to the dimensions of the container will then be of the functional form

$$S(t) \propto \frac{1}{t^3} \exp(-b/t^2) \qquad (4.8)$$

(with $b=mr^2/2kT$) for a density detector, and

$$I(t) \propto \frac{1}{t^4} \exp(-b/t^2) \qquad (4.9)$$

for a flux detector.

On the other hand, author may prepared a different distribution by opening the shutter of a small aperture in the gas's container for a brief interval at t=0. Because the probability per unit time of escaping through the aperture is now proportional to a molecule's velocity component normal to the aperture, an additional factor of the speed v appears in the speed distribution of the escaping particles (For the non-interacting molecules considered, the expansion of the gas through the aperture into the vacuum is purely effusive; no supersonic expansion takes place.)

$$P_v(v)dv = \frac{1}{2} \left(\frac{m}{kT} \right)^2 v^3 \exp\left(-\frac{mv^2}{2kT} \right) dv, \qquad (4.10)$$

$$P_E(E_t)dE_t = \frac{E_t}{(kT)^2} \exp\left(-\frac{E_t}{kT} \right) dE_t. \qquad (4.11)$$

This distribution is called a "flux weighted" Maxwell-Boltzmann distribution (or "v^3 Maxwell distribution" [88]). For a density detector, it corresponds to the TOF spectrum

$$S(t) \propto \frac{1}{t^4} \exp(-b/t^2), \qquad (4.12)$$

and for flux detector, the TOF distribution is

$$I(t) \propto \frac{1}{t^5} \exp(-b/t^2). \qquad (4.13)$$

The density (v^2) Maxwell-Boltzmann distribution is characterized by $\langle E_t \rangle$=1.5kT and $w=(4/3)^{1/2} \approx 1.155$, while the flux weighted (v^3) Maxwell-Boltzmann distribution has $\langle E_t \rangle$=2kT and w=1. Thermal desorption from a surface with unit striking probability results in a flux weighted Maxwell-Boltzmann distribution [88]. The same functional form is obtained (for very different reasons) in MGR-type photodesorption in the short lifetime limit [71]. Mean translational energies of desorbed species are therefore conventionally expressed as $\langle E_t \rangle / 2k_B$, which for a flux weighted Maxwell-Boltzmann distribution reduces to the translational temperature T_t.

Distinguishing between "density" and "flux weighted" distributions is necessary only if there are two different ways of defining the set of molecules to be described. For example, in the case of a gas in thermal equilibrium, one may be interested in the velocity distribution of all the molecules found in a certain volume (v^2-MB distribution), or of those molecules that impinge on a certain area per unit time (v^3-MB distribution). In the case of photodesorption there is no such ambiguity, since we obviously want to know the velocity distribution of all those molecules that desorb. For this reason, there is only one meaningful velocity distribution in photodesorption, which is a well defined quantity ($P_v(v)=dN/dv$, where N(v) refers to the number of molecules desorbed by a certain number of photons, with a velocity less than v. Usually, this distribution is then normalized by dividing it by the total number of desorbed molecules.) regardless of how it is measured (flux or density detection), and can be extracted from measured TOF spectra using Eq. (4.1). Reference to measured "velocity flux distributions" or "flux weighted velocity distributions" frequently found in the literature are thus neither necessary nor very illuminating. Terms such as "flux weighted velocity distribution" and "flux weighted mean translational energy" are actually quite confusing and should be avoided, since they are meant to refer to Pv(v) and $\langle E_t \rangle$ respectively, while the label "flux weighted" misleadingly implies another factor of v in addition to those already present in Eqs. (4.1) and (4.4). Only when a measured velocity distribution is compared with a thermal distribution is it necessary to specify whether the "density" or "flux" Maxwell-Boltzmann distribution [Eq. (4.6) or (4.10)] is used for comparison.

An empirical formula that is frequently used to fit experimental velocity distributions is the so-called "modified" Maxwell-Boltzmann distribution

$$P_v(v)dv \propto v^3 \exp\left(\frac{m(v-v_0)^2}{2kT}\right)dv\,, \qquad (4.14)$$

which can be interpreted as a thermal distribution at temperature T, superimposed on a stream velocity v_0 (as produced by a supersonic free jet expansion), and reduces to Eq. (4.10) for v_0=0. The purpose of the stream velocity is to make the reduced width of the distribution [which in Eq.(4.10) is fixed at w=1] an adjustable quantity. The fitting parameter v_0 takes on negative

values for distributions that are wider than a thermal distribution, obscuring the interpretation of v_0 as a stream velocity (since the "stream" of desorbing particles is then directed toward the surface).

In practical case, the desorbing molecules come from all of the area on the surface that is irradiated of the dissociation laser. If the solid angle of the detection at the focussing point of the probe laser, which ionizes the molecule coming from the irradiated area, is not small, the observed TOF spectrum will be broadened, compared to the Maxwell-Boltzmann distribution, due to the differences of the flight distance of the desorbing molecules that desorb from various points on the surface. In this case, the compensation has to be considered.

The schematic draw of the area around the probe point and substrate is shown in Fig. 4-2. The irradiated area is assumed to be a circle in a present work. The flight distance, r is expressed as below,

$$r = \sqrt{r_0^{\,2} + d^2}\,, \qquad (4.15)$$

where r_0 is the minimum flight distance, d is the distance from the center of the irradiated area, O. The molecules having same d value have same flight distances, therefore the number of the molecules having a certain flight distance depends on the r. However, the number of molecule which can reach to the focussing point is also governed by the eject angle θ. The angular distribution of the desorbing molecular is assumed to be a $\cos^2\theta$ distribution. Then, the molecular number is given by,

$$N(d,\theta) = 2\pi d\cos\theta\,. \qquad (4.16)$$

Since $\cos\theta = r_0/d$ and $d = \sqrt{r^2 - r_0^{\,2}}$ according to Eq(4.15), Eq(4.16) is transferred to,

$$N(r) = 2\pi\sqrt{r^2 - r_0^{\,2}}\,\frac{r_0}{r}\,. \qquad (4.17)$$

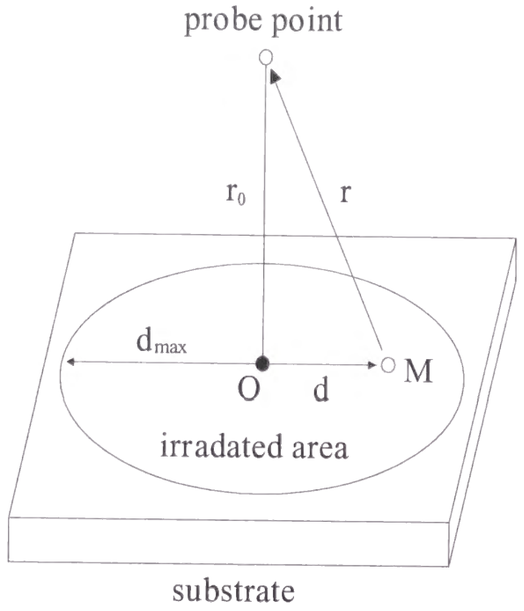

Fig. 4-2 The schematic draw of the area around the probe point and substrate. A circle indicates an area irradiated of the dissociation laser. O is the center of the irradiated area. M means Molecule. r is the flight distance. r_o is the minimum flight distance. d is the distance from the center of the area. d_{max} is the radius of the irradiated area.

With t = r/v, S(t) is the function of r. the compensated spectrum F(t) is given by,

$$F(t) = \int_0^{r\,max} S(t,r) \cdot N(r) dr \,, \tag{4.18}$$

where L_{max} is a maximum distance of L, which given by the following equation with a radius of the irradiated area, d_{max},

$$r_{max} = \sqrt{r_o^{\,2} + d_{max}} \,. \tag{4.19}$$

Since the calculation of F(t) is very complicated, in the present work, therefore, the author divides r in ten parts and calculates the each S(t,r)N(r), then sums all the spectra. The summed spectra corresponding to F(t), is approximately described blow,

$$F(t) \propto \sum_{i=1}^{10} \left(\frac{r_i}{t}\right)^4 \exp\left(-\frac{m}{2kT}\left(\frac{ri}{t}\right)^2\right) \cdot 2\pi\sqrt{r^2 - r_0^{\,2}} \cdot \left(\frac{r_0}{r}\right)^2, \tag{4.20}$$

where r_i is given as,

$$r_i = i\frac{d_{max}}{10} \text{ (i=1, 2, 3,…,10).} \tag{4.21}$$

All experimental results in present work are well fitted with the. Eq. (4.20).

Resonance-enhanced multiphoton ionization technique

Comparing other light sources, a distinctive feature of the laser source is so extreme-high density of photon flux at a certain wavelength, that nonlinear optical processes are obviously appeared. The multi photon ionization is one of such processes and the phenomenon that molecules are excited up to their ionization potential and result in ionic molecules. The detection method of ions is so high sensitive as well as photon detection, that various photospectroscopies can be applied. Particularly, the resonance enhanced multiphoton ionization technique by using a resonance effect is the most sensitive spectroscopy among laser photospectroscopies in the visible and ultra-violet light region [89], and widely used for the investigation of electron excited states [90].

Considering a generation of a REMPI spectrum through the two photon ionization process, if the molecular ionization potential, IP_o, satisfies the following condition, $2h\nu \geq IP_o$, then the molecular will be ionized and generate ion current ,i. The magnitude of i is represented as below,

$$j(\nu) \propto N_o \sigma^{(2)}(\nu) I^2(\nu) \,, \tag{4.22}$$

where N_0 is the amount of the ground state, S_0, $I(\nu)$ is the intensity of laser light, and $\sigma^{(2)}(\nu)$ is the probability of the two photon absorption transition from S_0 to ionization continuum. Sweeping the wavelength of the laser light, when $h\nu$ is close or equal to the transition energy from S_0 to S_e, E_{0e} (= E_e - E_0), $j(\nu)$ increase remarkably. Therefore, if to detect $j(\nu)$ with scanning $h\nu$, a REMPI spectrum, corresponding to the absorption spectrum of the transition $S_e \leftarrow S_0$ can be obtained. The increase of Ion current is caused by the increase of the resonance effect on the $\sigma^{(2)}(\nu)$. The reason is considered in two ways. One is the explanation of the direct two photon absorption transition based on the nonlinear interaction between a molecular and a electric field of radiation. In this explanation, $\sigma^{(2)}(\nu)$ is expressed in the following description,

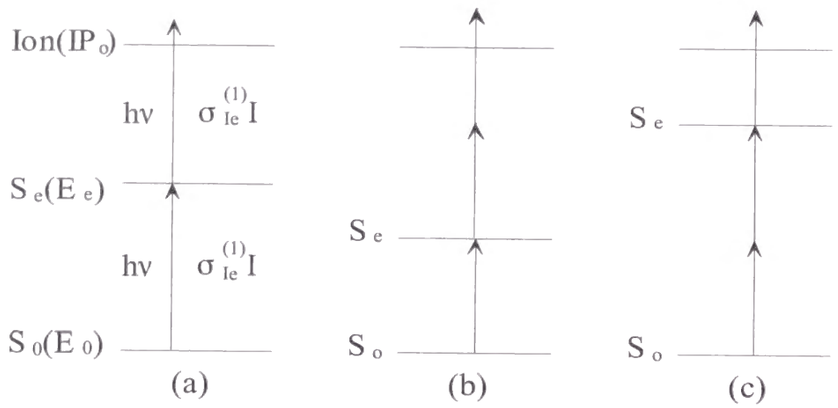

Fig. 4-3 The REMPI processes: (a) (1+1) REMPI, (b) (1+2) REMPI, (c) (2+1) REMPI. See in the text.

$$\sigma^{(2)}(\nu) \propto \left| \frac{\mu_{Ie} \cdot \mu_{e0}}{E_{0e} - h\nu - i\Delta_e} \right|^2, \qquad (4.23)$$

where μ_{Ie} and μ_{e0} are transition moments of $I_{on} \leftarrow S_e$ and $S_e \leftarrow S_0$, respectively, Δ_e is the width of the spectrum line. Therefore, when $h\nu = E_{0e}$, $\sigma^{(2)}(\nu)$ has a maximal value. At this point, since S_e is dealed as a virtual intermediate state on a coherent multi-photon process, it is not necessary to consider that the excitation to Se is happen actually. On the other hand, another explanation, the stepped excitation process, is considered that the excitation to S_e occurs actually. As shown in Fig. 4-3, the primary photon energy causes $S_e \leftarrow S_0$ transition and the molecule will be excited state. If the molecule absorbs the secondary photon before quenching, the transition to the ionization continuum is caused on the molecule. Thus, the following expression about this process is derived from Eq. 4.20 since this process is incoherent,

$$j(\nu) \propto N_0 \left\{ \sigma_{e0}^{(1)}(\nu) I(\nu) \right\} \times \left\{ \sigma_{I0}^{(1)}(\nu) I(\nu) \right\}, \qquad (4.24)$$

where $\sigma_{e0}^{(1)}$ and $\sigma_{I0}^{(1)}$ is the cross section of the transition $S_e \leftarrow S_0$ and $I_{on} \leftarrow S_e$, respectively. Generally speaking that the absorption band of the transition to the ionization continuum is a broad band, $\sigma_{I0}^{(1)}$ is almost independent of ν. Therefore, $j(\nu)$ indicates the change of $\sigma_{e0}^{(1)}$. This treating is based on the kinetics of the process (a). Commonly, the analysis of the multi photon process

on the quantum mechanism is not so simple but it is possible to treat it on the semi-quantitative analysis. [90, 91]

Figure 4-3a shows the process called as the one-photon resonanced two-photon ionization process, which denote (1+1)MPI in an abbreviation. The more high order process, such as (1+2)MPI and (2+1)MPI, is also possible to observe (shown in Fig.4-3b and c.) In (2+1)MPI the resonanced intermediate state has to be the two-photon allowed transition from S_0, therefore the spectrum of the (2+1)MPI is available to observe the unique state only allowed for two photon resonanced excitation. However, since the increasing number of photon required to the transition decreases the possibility of the transition, it is necessary to make a lot of effort to increase the photon density in the excitation region.

Generally, the MPI photospctroscopy has many advantages as described blow:

1) Negligible for the ability of fluorescence emissivity.
2) More sensitive compared with the laser induced fluorescence (LIF) technique due to the efficiency of a detection solid angle, since generating ions are extracted to the detector.
3) Adaptable to the detection of higher order transition due to its high sensitivity.
4) Adaptable to the observation of the transition in the vacuum ultra-violet region by using the visible light multi-photon process.
5) Adaptable to the two color laser experiment and the time of flight mass spectroscopy.

By using these advantages, this photospctroscopy is available to investigate the low pressure gas phase reaction and molecular beam reaction.[92] Recently, the detection for a liquid phase and solid phase reaction are also being examined.[93] Further more, MPI technique is not available to only one color laser detection to investigate the excited state of a molecule, but also two color laser detection [94]. By using this technique, it is possible to perform various photospectrometries.

Pulse lasers emit very high density photon flux at a moment. For example, when the general dye laser emits 1 mJ at a pulse which has a pulse width of 10×10^{-9} ns, the corresponding laser power P is 10^5 W. As the

wavelength λ of the laser light is 500 nm, the photon flux η at a second is given as following,

$$\eta = \frac{P}{h\nu} = \frac{P\lambda}{hc}. \qquad (4.25)$$

Therefore, the calculated photon flux η equals 2.5×10^{24} photons. As the laser beam cross section denote S, the beam intensity I is represented as I = P/S. The photon flux density at a unit area, n_p, is described as below;

$$n_p = \frac{P\lambda}{hcS}. \qquad (4.26)$$

If S=0.03 cm^2, the calculated np =8.3×10^{25} photon flux / s·cm^2. Since the photon flux density can be replaced to the photon density, it means that 138 mol of photons pass through a unit area at a second. As using a focusing lens, the photon density increases to more than 10^{27} photons / s·cm^2. The continuous wave (cw) laser can emit high average output, but the density is not so high that cw lasers are unsuitable for MPI method. Commonly, the nanosecond pulse laser, such as N_2 laser, excimer lasers and the second and third harmonic light of the Nd:YAG laser, is used for pumping a dye laser.

The laser cross section does not has an uniform intensity. The center of the laser cross section has a maximum of the intensity, and the surrounding area has a lower intensity, usually. Assuming that the intensity distribution on the laser cross section has a Gaussian profile as shown in Fig. 1-22. In this case, the beam diameter is represented as a beam waist diameter D_0. Therefore, $\frac{1}{2}D_0$ is defined as a beam radius at the point that the beam intensity is $1/e^2$ (=0.135) times of the maximum intensity. When the laser light which has the wavelength λ is focused by the lens L as a parallel beam. The beam waist at the focussing point F, denote as $2\omega_0$ is given as following,

$$2\omega_0 = \left(\frac{4\lambda}{\pi}\right)\left(\frac{f}{D_0}\right), \qquad (4.27)$$

where f indicates the focussing distance. In this case, when the distance from F, x, is large enough, i.e. $x > \pi\omega_0^2/\lambda$, it is considered that the laser beam is dispersed at the solid angle θ from F. Similarly, the focussing depth is described as a following equation,

$$d_0 = \left(\frac{8\lambda}{\pi}\right)\left(\frac{f}{D_0}\right)^2. \qquad (4.28)$$

For example, if λ = 500 nm, D_0 = 4 mm and f = 200 nm, then it is estimated that ω_0 = 32 μm and d_0 = 3.2 mm. If f = 100 mm, then ω_0 = 16 μm and d_0 = 0.8 mm.

The amount of photons at a pulse of laser light can be estimated by using the power meter to obtain the total energy and calculating with the Eq. (4.28). In the Gaussian beam cross section profile, 99 % of the total beam power is included in the inside of the circle that has a diameter of the beam west. Therefore, as focussing with the lens, the photon density is given as;

$$n_p = \frac{P\lambda}{2\pi hc\omega_0^2}, \qquad (4.29)$$

As recognized above, the shorter is the focussing distance, the densified is the photon flux in the focussing region.

By the way, Eq. (4-27 and 29) are assumed that the laser beam is a parallel beam which has a diameter D_0. Actually, however, the laser output beam is dispersed in the certain degree, 0.5 – 10 mRad, that is determined by the beam waist of the oscillator. Therefore, the estimated value of ω_0 and d_0 should be considered as a tentative value, and more precisely and desirably, the value has to be determined by measuring the real spot size of focussing laser. Irradiating the laser pulse to a glass plate covered with evaporated aluminum or a thermo-sensitive paper at the place F, the irradiated spot can be measured by using a scaled microscope. Measuring a change of the spot size as a function of the laser intensity by using ND filter, ω_0 is estimated by using the following equation;

$$I(r) = I(0)\exp\left(\frac{-2r^2}{\omega_0^2}\right), \qquad (4.30)$$

where I(0) is the center value of the Gaussian profile, and r is the radius on the profile.

There are some problems on normalizing the MPI spectrum with the laser intensity. One of them is the saturation of the ion current. For example, in a (1+1) MPI process, the dependence of the laser intensity should indicate a two-photon process, basically. However, in case of very low concentration of molecules, it may be occurred that all of them in the focussing field can be

ionized if the laser intensity is enough strong. In this case, the ion current will be saturated and the dependence will not indicate a two-photon process. This tendency is more apparent in the case of more high order multi photon process. Extremely, it can be observed that all of the peak intensities are same or the peak width is broader abnormally. Therefore, as dealing with the intensity of lasers, the saturation of the ion current has to be avoided, i.e. the laser intensity should be saved properly or a long focussing lens should be used.

Thus, it is important that the checking the peak dependence of the laser intensity in all of the spectrum region used in the experiment is advanced to the experiment by using a log plot of the peak intensity - laser intensity in order to investigate the order of dependence.

Ion detector

The ion detecting system of MPI method is shown in Fig. 4-5. The system is equipped in the ultra-high vacuum chamber and consisted of an electrostatic lens (Einzel lens), detector and extractor. When the sample gas which is injected by a pulse molecular beam nozzle or desorbed from the substrate is at the focussing point of the probe laser, O, molecules are ionized and accelerated to the extractor E by electrical field, approximately 3.0 kV, and then come into the drift tube which works as a electrostatic lens. The drift tube focuses the molecule to the detector D, since the focussing point has a spatial extent in the certain space and the molecule has various velocity and direction in the translational motion. The molecule drifts in the electrostatic lens tube and reaches to the ion detector D. A ceratron or microchannel plate is commonly used for the ion detector. The former is easy to maintenance and cleaning, but not so high-sensitive. Meanwhile, the later is available for a high-sensitive detection system, but it is fragile and weak for the gas contamination. The signal of the ion from the ion detector is amplified electrically and recorded by a computer passing through a boxcar integrator and A/D converter. The ion flies at a uniform motion in the electrostatic tube for a certain time t, which is determined by the following equation,

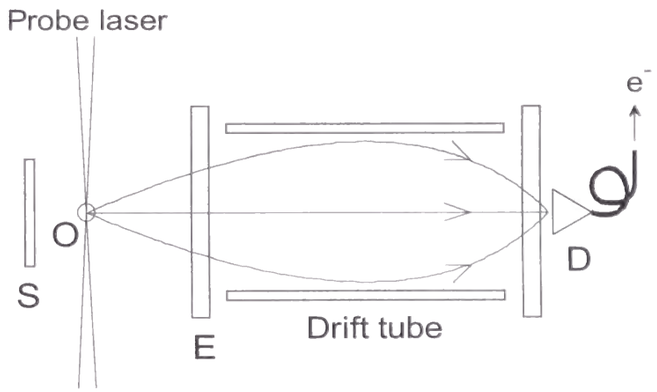

Fig. 4-5 Schematic drawing of the ion detecting system: the probe laser beam focussed on the point of O. E is the extracting-ring, which is at 3.0 kV. Drift tube (cylindrical) is at 1.5kV. The ions which fly though the drift tube are focussed on the detector D. S is the substrate.

$$t = L\left(\frac{2eV}{m}\right)^{-\frac{1}{2}}, \qquad (4.31)$$

where V is the acceleration voltage of the extractor, L is the length of the electrostatic lens tube and m is the molecular weight. The ion current is the function of the time delay from the fire of a pulse laser. If the trigger is set on the fire of the laser, the subject ion signal is appeared at delay time t. Therefore, the delay of the boxcar should be set around t with the proper gate width for the ion signal. Usually it is easily determined by using the oscilloscope.

Apparatus

Surface photodissociation on a cooled Au (111) polycrystalline substrate was performed with a combination of pulsed molecular beam, excimer and dye lasers. Our experimental setup is shown in Fig. 1-23. Neat NO_2 was deposited on an Au (111) polycrystalline substrate by expanding the gas with a pulsed molecular beam head (General Valve) at a repetition rate of 10 Hz. In order to avoid unwanted gas phase photodissociation, the delay between molecular beam and photolysis laser pulses was set to 50 ms. A typical stagnation pressure of the gas valve was kept at 100 Torr. In order to change effective exposures of NO_2 on the substrate, the open gate time of the pulsed beam head was adjusted by the pulse voltage duration for 300-500 μs. A vacuum chamber was pumped by two turbo molecular pumps in tandem (Seiko 600 / s^{-1} and Mitsubishi 50 / s^{-1}). The chamber pressure was P = 5×10^{-9} and $1\sim10\times10^{-8}$ Torr without and with sample gas injection, respectively. The chamber pressure was monitored 50 cm away from the Au substrate with a cold cathode pressure gauge (MDC, PGC3). Under these pressure conditions, multilayered N_2O_4 were

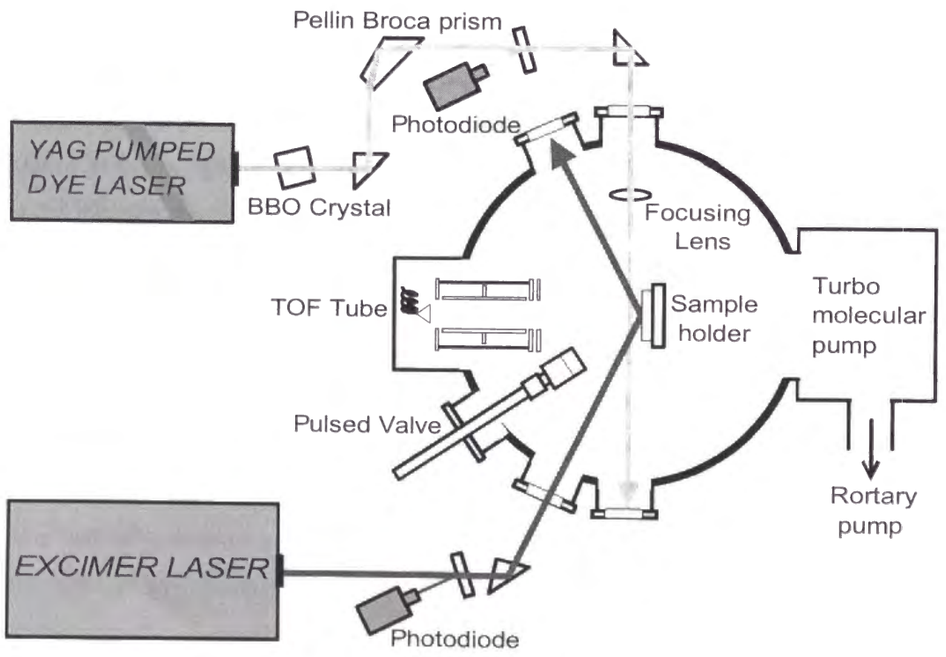

Fig. 4-6. The Apparatus for investigation of photochemical reaction dynamics.

formed on the substrate, depending on the substrate temperature and pulse duration. The substrate temperature was controlled for T = 85 - 300 K by combination of conductive cooling with liq. N_2 and resistive heating with an electric heater.

Polycrystalline Au(111) substrates were prepared by DC glow-discharge sputtering, in which Ar^+ bombardment with low energy leads to atomic surface flatness of the sputtered films. [95] The substrate flatness was examined with scanning tunneling microscopy and found to be at most 5°. This small tilt angle might cause an error within 1 % for calculation of the p- and s-polarization effect of the incident dissociation laser light. Typical grain sizes of the polycrystallines were estimated to be submicrometers.

For the surface photochemistry, the light source to occur the photochemical reaction on the surface is necessary. Pulsed lasers are available for it because of its narrow pulse width, bandwidth of the wavelength, linearity, and intensity. Among them, the excimer laser is the most suitable source for investigating photochemical reactions due to its ability for emitting high intensity ultra-violet light, such as ArF(193 nm), KrF(248 nm) and XeF(351 nm) excimer lasers. It is easy for them to dissociate and desorb most of molecules. Then author used the excimer laser (Lambda Physik, COMPex, 10 Hz, 0.1 - 5 mJ/cm^2) as a dissociation laser for photochemical experiments. The temperature rises due to the photoirradiation of the dissociation lasers are estimated lesser than 5 K in all of this experimental condition, since the thermal conductivity of Au is extremely high, 3.15 J / s cm K. The molecules dissociated and desorbed from a substrate by the dissociation laser are radicals usually. The YAG pumped dye laser (Lambda Physik, ScanMate) is used for detecting the radicals by the REMPI method. The prove laser makes the desorbed molecules ionized and detects it with the ion detector. The probe pulse laser light intersects the flux of NO and O those were photodesorbed from the substrate upon irradiation of pulsed excimer laser light at 193 and 351 nm. Time-of-flight spectra were taken as a function of time delay, Δt, between photolysis and probe pulses. The time delay was controlled with a delay generator (Stanford Research, DG535). The one-photon transition of NO ($A^2\Sigma$ - $^2\Pi_{3/2}$, v"=0 and 3, J") was probed by resonance-enhanced multiphoton

ionization at 226 nm. O(^3P_j, j=0,1,2) was also probed for the two-photon resonant REMPI transition of O($^3D_{j'}$ - $^3P_{j''}$) at 225.7-226.2 nm. The photofragments were ionized at 3 mm away from the substrate. The subsequent ion signals were detected with a homemade time-of-flight mass spectrometer. When we performed the similar experiment at 248 nm, the observed results were in between the 193 and 351 nm cases. In this paper we report only two extreme cases at 193 and 351 nm.

The dye solutions, Coumarine 47 (Lambda Physik), was used for the NO ($A^2\Sigma$ - $^2\Pi_{3/2}$, v"=0, J") and O($^3D_{j'}$ - $^3P_{j''}$) detection. Coumarine 430 (Lambda Physik) was used for NO ($A^2\Sigma$ - $^2\Pi_{3/2}$, v"=0, J") detection. All the solution is prepared by diluting the dye powder with methanol.

4.2.2 Sample preparation

The sapphire substrate deposited spattered Au was cleaned by the super sonic machine washing in methanol before set into the chamber. In the UHV condition, the substrate was cleaned with following processes before every first experiment of the day. Firstly, the substrate was heated up to 500 K for 5 min, and further heated at 673 K for 10 min with exposing the substrate to NO_2 gas and an ArF excimer laser irradiation, which the gas is injected by a pulsed valve nozzle to keep the chamber pressure at 3×10^{-8} Torr, in order to remove the contaminating substance. Then the substrate is cooled to 90 K with irradiating the excimer laser to prevent from depositing any unwanted gas.

4.2.3 Dependence probe method of signal intensity on polarization of the incident light.

Utilization of the transverse polarized nature of light has proven to be of great assistance in many investigations of problems in molecular and surface physics [39, 50, 60, 96].

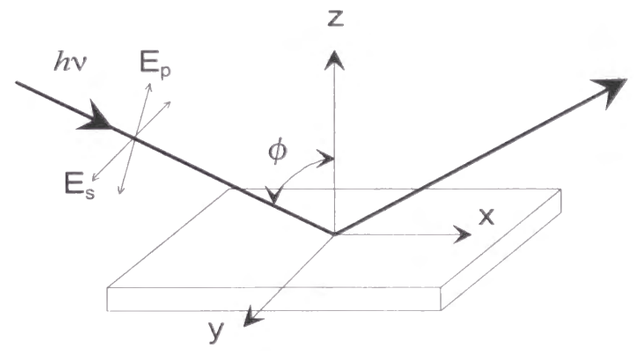

Fig. 4-7 Schematic drawing of the optical geometry at the metal interface: the light beam has two principle polarizations One perpendicular and one parallel to the plane of incidence. At the interface three components of the electric field are to be considered. They are named according to the coordinates.

Ellipsometric experiments have revealed that the macroscopic Maxwell equations provide an adequate desorption of the electromagnetic field close to an interface, which may then be considered to interact with the adsorbate.

Figure 4-7 sketches the geometry at the plane boundary between vacuum and the metal surface. Because our experiments, in general, were carried out at less than 3 ML coverage, we will neglect the refractive properties of this very thin overlayer, which are unknown. The electric field description is then governed by one material property, the complex index of refraction of the metal n_2 (μ=1), which depends on photon energy.

Part of the incident light is reflected at the interface, the rest is refracted into the substrate and absorbed within a penetration depth of about a tenth of the wavelength. The incident light can be subdivided into two independent polarizations, one with the electric field vector parallel to the plane of incidence (p polarization) and the other perpendicular to it (s polarization).

The incoming and the reflected waves form a standing wave at the boundary. In the case of an absorbing material, this wave stretches into the bulk. For s polarization only a component parallel to the surface $\langle E^2_{s,y}\rangle$ can exist. For p polarization two components are present: one in the plane of the surface $\langle E^2_{p,x}\rangle$ and one parallel to the surface normal $\langle E^2_{p,z}\rangle$.

We now briefly summarize the results of the electromagnetic theory as presented, for example, by McIntyre [96]. The Fresnel coefficients correlate the electric field amplitudes of incident and reflected light

$$r_s = \frac{\cos\phi_1 - \sqrt{n_2^{\,2} - \sin^2\phi_1}}{\cos\phi_1 - \sqrt{n_2^{\,2} - \sin^2\phi_1}}, \tag{4.32}$$

$$r_p = \frac{n_2^{\,2}\cos\phi_1 - \sqrt{n_2^{\,2} - \sin^2\phi_1}}{n_2^{\,2}\cos\phi_1 - \sqrt{n_2^{\,2} - \sin^2\phi_1}}, \tag{4.33}$$

where ϕ_1 is the angle of incidence. The reflectivity at the boundary is then given by

$$R_i = |r_i|^2 = r_i \cdot r_i^*, \tag{4.34}$$

where the subscript stands for the two polarization cases. The absorption coefficients are then calculated by

$$A_i = 1 - R_i. \tag{4.35}$$

From the Fresnel coefficients, we can also derive the absolute phase change upon reflection for the two polarizations. They are given by the quantities δ_s and δ_p with

$$\delta_i = \tan^{-1}\left[\frac{\mathrm{Im}(r_i)}{\mathrm{Re}(r_i)}\right]. \tag{4.36}$$

The mean-square electric field strength of the different components in the standing wave at the boundary is then given by – assuming unity amplitude of the incident wave –

$$\left\langle E_{s,y}^{\,2}\right\rangle = (1 + R_s) + 2\sqrt{R_s}\cos\delta_s, \tag{4.37}$$

$$\left\langle E_{p,x}^{\,2}\right\rangle = \cos^2\phi_1\left\{(1 + R_p) - 2\sqrt{R_p}\cos\delta_p\right\}, \tag{4.38}$$

$$\left\langle E_{p,z}^{\,2}\right\rangle = \sin^2\phi_1\left\{(1 + R_p) + 2\sqrt{R_p}\cos\delta_p\right\}. \tag{4.39}$$

With this set of equations all relevant quantities can be easily calculated based on the optical constants for Au. Figure 4-8 shows the electric field intensities and absorption coefficients as function of angle of incidence for 193 nm radiation. For perpendicular incidence, the absorption is independent of the polarization. With increasing angle of incidence the absorption for the p component passes through a maximum, whereas the absorption for the s component decreases continuously. At grazing incidence no light will be absorbed.

The field intensity of the component parallel to the metal surface decreases, for both polarization cases, monotonically to zero. But the field component parallel to the surface normal $\langle E_{p,z}^{\,2}\rangle$ is zero at normal incidence, shows a pronounced maximum, and falls then to zero at large angles.

The absorption by an adsorbate A_{mol} will be dependent on its molecular orientation determining the direction of the transition dipole moment μ with respect to the total electric field vector E at the surface

$$A_{mol} \approx (E \cdot \mu)^2. \tag{4.40}$$

If, for example, a molecule is oriented with its axis normal to the surface and exhibits a perpendicular transition dipole moment, only the field components parallel to the surface will contribute to the absorption by the molecule. In the opposite case, molecule with a transition dipole moment along the surface normal, only the z component in the case of p polarization can be absorbed by the molecule and there will be no absorption for s polarization. In the most general case for p polarization, both components can contribute, but they are weighted by the cosine squared of their respective angle to the direction of μ.

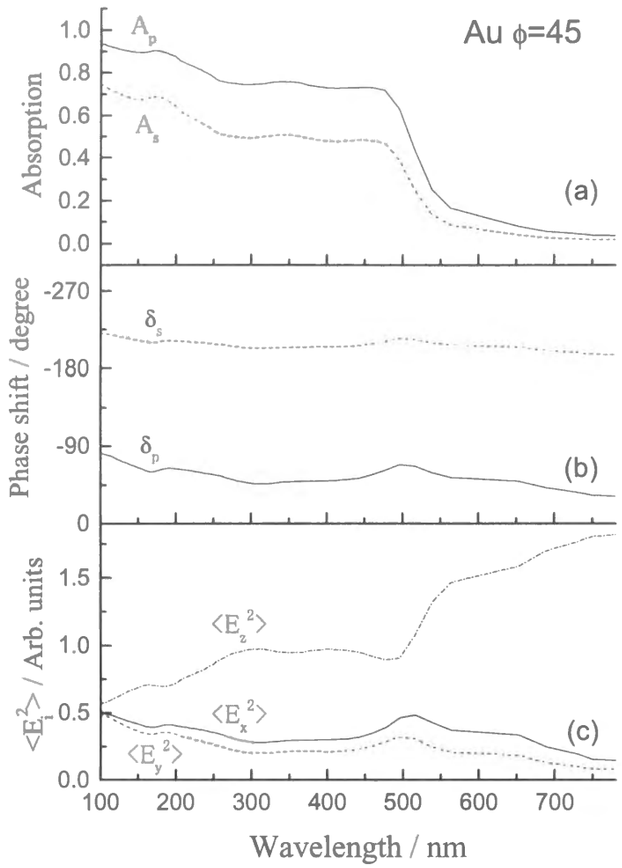

Fig. 4-9 The optical parameters of Au for p, s-polarized incident light, absorption A_i (a), phase shift δ_i (b), and electrical field intensities $\langle E_i^2 \rangle$, as a function of a incident photon wavelength. The incident angle from the surface normal is ϕ = 45°. All the plots are calculated with Eq(3.25-3.36). The complex indexes of refraction were referred to Ref. [97].

When the transition dipole moment of the molecule leans toward the surface at the angle θ from the surface normal and assuming // transition, A_{mol} has three components, A_x, A_y and A_z, that can be described as

$$A_x = \int \left\{ \langle \cos^2 \phi \rangle \sin^2 \theta \left\langle E_x^{\,2} \right\rangle \right\} d\phi = \frac{1}{2} \sin^2 \theta \left\langle E_x^{\,2} \right\rangle, \tag{4.41}$$

$$A_y = \int \left\{ \langle \sin^2 \phi \rangle \sin^2 \theta \left\langle E_y^{\,2} \right\rangle \right\} d\phi = \frac{1}{2} \sin^2 \theta \left\langle E_y^{\,2} \right\rangle, \tag{4.42}$$

$$A_z = \cos^2 \theta \left\langle E_z^{\,2} \right\rangle. \tag{4.43}$$

The desorption signal intensities by the s and p-polarized, I_s and I_p respectively, are given by

$$I_p = A_x + A_z, \tag{4.44}$$

$$I_s = A_y. \tag{4.45}$$

Then, the signal intensity ratio, I_s/I_p is

$$\frac{I_s}{I_p} = \frac{\sin^2 \theta \left\langle E_y^{\,2} \right\rangle}{2\cos^2 \theta \left\langle E_z^{\,2} \right\rangle / \xi + \sin^2 \theta \left\langle E_x^{\,2} \right\rangle} \text{ (for // transition)}, \tag{4.46}$$

where $\xi = \left|\varepsilon_{eff}\right|^2 = \left|\sqrt{\varepsilon_{vac} \cdot \varepsilon_{sub}}\right|^2 = \left|\varepsilon_{sub}\right| = \left|n\right|^2$. (4.47)

E_{eff} is the geometric mean of the macroscopic dielectric fields constant between the vacuum (E_{vac}) and substrate (E_{sub}) sides,

Meanwhile, If assuming perpendicular transition, the A_x, A_y and A_z, that can be described as

$$A_x = \int\int (\cos\varphi \cos\theta \cos\phi - \sin\varphi \sin\phi)^2 \, d\phi \, d\varphi + \int\int (\sin\varphi \cos\theta \cos\phi + \cos\varphi \sin\phi)^2 \, d\phi \, d\varphi = 2\mu^2\pi^2 (\cos^2\theta + 1), \tag{4.48}$$

$$A_y = \int\int (-\cos\varphi \cos\theta \sin\phi - \sin\varphi \cos\phi)^2 \, d\phi \, d\varphi + \int\int (-\sin\varphi \cos\theta \sin\phi + \cos\varphi \cos\phi)^2 \, d\phi \, d\varphi = 2\mu^2\pi^2 (\cos^2\theta + 1), \tag{4.49}$$

$$A_z = \int\int (\cos\varphi \sin\theta)^2 \, d\varphi + \int\int (\sin\varphi \sin\theta)^2 \, d\varphi = 4\mu^2\pi^2 \sin^2\theta \tag{4.50}$$

where ϕ, φ, θ is defined by Euler angles. [98]

Then, the signal intensity ratio, I_s/I_p is given by (4.45) and (4.46),

$$\frac{I_s}{I_p} = \frac{(\cos^2\theta + 1)\left\langle E_y^{\,2} \right\rangle}{2\sin^2 \theta \left\langle E_z^{\,2} \right\rangle / \xi + (\cos^2\theta + 1)\left\langle E_x^{\,2} \right\rangle} \text{ (for } \perp \text{ transition)}, \tag{4.51}$$

Since ϕ, the incident angle of the laser light, δ, phase change, and R, reflectivity, are easily determined by experimental set up and the index of reflectivity of the metal, $\langle E_{p,x}^2 \rangle$, $\langle E_{s,y}^2 \rangle$ and $\langle E_{p,z}^2 \rangle$ can be calculated by using them. Figure 4-9 shows changes of the parameters, δ_i, A_i, $\langle E_{p,x}^2 \rangle$, $\langle E_{s,y}^2 \rangle$ and $\langle E_{p,z}^2 \rangle$, at a incident angle ϕ=45°, which is our experimental condition, as a function of the incident photon wavelength in the UV-visible light region. If the I_s/I_p is measured experimentally and correctly, θ can be estimated by using the Eq.(4.46). Calculated I_s/I_p values in both cases of perpendicular and parallel

Table 4-1 Effect of laser polarization (s or p) on the signal intensity of NO(v=0) from N_2O_4 on Au(111): Direct photoabsorption of O_2NNO_2

		Signal intensity ratio (I_s/I_p)					
	λ(nm) =	193		248		351	
	χ(deg) =	0	90	0	90	0	90
Θ(deg) = 90		0.85	0.56	0.86	0.57	0.72	0.48
54.7		0.56	0.66	0.57	0.68	0.48	0.58
0		0	0.85	0	0.86	0	0.72
Experimental		0.88±0.05		0.75±0.05		0.65±0.03	

Θ is defined as an angle between the N-N axis of the adsorbed molecule and the Au surface. Random orientation is defined as Θ = 54.7°.
χ is an angle between the N-N axis and the transition moment.
Incident angle of dissociation laser light is fixed at ϕ = 45° for calculation of the ratios in the equations given by Ref. [50].

transitions are presented in Table 4.1, comparing with the experimental values that is obtained in Section 4.3.6.

4.2.4 Estimations of a substrate temperature during the photoirradiation.

Most of incident photon energies that is not used for the photodesorption of adsorbates will cause a substrate temperature rise in the photoirradiated region of the substrate, after a relaxation of the energy. Since the photon penetration depth in most metals is on the order of 10^{-6} to 10^{-5} cm (several hundred Å) and scattering length are slightly shorter (~ 10^{-6} cm), the majority of the created hot carriers will reach the surface with undergoing inelastic scattering. In a complicated, and so far poorly understood, many-body scattering process, the energy in the nascent electrons (holes) will be lost through electron (hole-electron) collision, electron-plasmon collisions, electron-hole recombination associated with Auger processes, and electron-photon collision. After ~10^{-12} s, the excitation energy is ultimately shared with the atoms in the solid and is transformed into lattice photons (forming heat). [99] Since thermal activation generally lead to chemistry, it is important to determine the extent to which thermal effects contribute to the observed photon-driven chemistry.

If a surface photochemical process is the result of surface heating, its rate is then a function of the energy deposited into the substrate. The only wavelength requirement, and one easily met throughout the visible and

ultraviolet region, is absorbed by the substrate. When pulse laser light is employed, the temperature rise is very different from that for cw laser by which the substrate is in the equilibrium state. The thermal consequence of the pulsed laser irradiation has been discussed by Yardley [100] and Osmundsen et al.[101].

In order to determine the temperature rise of a surface due to pulse laser heating, it is necessary to find solutions to the heat-condition wquation which can be written as

$$\nabla \cdot J(r,t) + \rho c \frac{\partial T(r,t)}{\partial t} = A(r,t), \tag{4.52}$$

where T(r,t) is the temperature as a function of position (on the surface) and time, J(r,t) is the thermal energy crossing a unit area per unit time (i.e. heat flux), ρc is the heat capacity per unit volume, and A(r,t) is the net energy per unit volume per unit time generated within the solid. Since

$$J(r,t) = -K\nabla T(r,t), \tag{4.53}$$

where K is assumed to be isotropic, then Eq. (4.47) becomes

$$\nabla^2 T(r,t) - \frac{1}{\beta}\frac{\partial T}{\partial t}(r,t) = -\frac{A(r,t)}{K}, \tag{4.54}$$

where β, the thermal diffusivity, is defined by

$$\beta = \frac{K}{\rho c}. \tag{4.55}$$

If it is assumed that the substrate is a semi-infinite slab of material with its surface at the plane z = 0 and that the transverse dimensions of the laser beam are large compared to the distance over which heat is conducted during the laser pulse, the problem can be formulated in one dimension by the heat flow equation as

$$\frac{\partial^2 T(z,t)}{\partial z^2} - \frac{1}{\beta}\frac{\partial T(r,t)}{\partial t} = -\frac{A(r,t)}{K}. \tag{4.56}$$

The temperature raised by the pulse laser light is given by the following way. Letting T(z,t =0) = 0 and assuming that the incident laser pulse is square with a pulse width of τ seconds, then the temperature rise of the surface is

$$T(0,\tau) = \frac{2\alpha I_m (1-R)}{K}\frac{(\beta\tau)^{1/2}}{\pi^{1/2}}, \tag{4.57}$$

where α is the fraction of the radiation passing through the substrate that is adsorbed, R is the surface reflectivity at the laser wavelength, $\alpha I_m(1-R)$ is the intensity adsorbed at the surface. The radiative loss term is ignored.

For a metal, R correlates to the incident angle and the complex index of refraction. The calculations have been explained in the Section 3.2.3. R_s and R_p are estimated with Eqs. (3.25-3.27). Since the excimer laser beams are circularly polarized lights approximately, the following equation can be derived,

$$R = \frac{R_s + R_p}{2}. \qquad (4.58)$$

With using estimated R, the substrate temperature rises are estimated for all the experimental condition and represented in Table 4-2. Used physical properties of the substrate are presented in Table 4-3.

Table 4-2. Substrate temperature increase of Au by photoirradiation.

wavelength (nm)	Peak laser power I_m (W/cm^2)	α	R	τ (s)	ΔT (K)	T_s (K)
			Au (80 K)			
193	3.1×10^5	1	0.23	1.6×10^{-8}	3.86	84
248	3.1×10^5	1	0.34	1.6×10^{-8}	3.30	83
351	3.1×10^5	1	0.37	1.6×10^{-8}	3.15	83

Table 4-3. The physical properties of Au substrates (Ref. 15)

parameters	value
Density, ρ (g/cm^3)	19.32
specific heat, C (J/g K)	1.310
heat capacity per unit volume, ρC (J/cm^3 K)	25.3
thermal conductivity, K (W/cm K)	3.15
thermal diffusivity, β (cm^2/sec)	0.125

References

[1] R. B. Hall and S. J. Bares, in: Chemistry and Structure at Interfaces, Eds. R. B. Hall and A. B. Ellis (VCH, Deerfield Beach, FL, 1986) p. 85

[2] C. E. Bartosch, N. S. Gluck, W. Ho. and Z. Ying, Phys. Rev. Lett. **57**, 1425 (1986)

[3] N. S. Gluck, Z. Ying, C. E. Bartosch and W. Ho, J. Chem. Phys. **86**, 4957 (1987)

[4] T. S. Baller, J. C. S. Kools and J. Dieleman, Appl. Surf. Sci. **46**, 292 (1990)

[5] J. M. Hicks, J. E. Urbach, E. W. Plummer and H. –L. Dai, Phys. Rev. Lett. **61**, 2588 (1988)

[6] R. Zenobi and R. N. Zare, in: Advances in Multi-Photon Processes and Spectroscopy, Vol. 7, Ed. S. H. Lin (World Scientific, Singapore, 1991)

[7] J. F. Ready, Effects of High Power Laser Radiation (Academic Press, New York, 1971)

[8] J. H. Bechtel, J. Appl. Phys. **46**, 1585 (1975)

[9] D. Burgess, Jr., P. C. Stair and E. Weitz, J. Vac. Sci. Technol. A **4**, 1363 (1986)

[10] B. G. Koehler and S. M. George, Surf. Sci. 248, 158 (1991)

[11] W. C. Natzle, D. Padowitz and S. J. Sibener, J. Chem. Phys. **88**, 7975 (1988)

[12] E. F. Lazneva, Rad. Eff. Defects Solids **115**, 257 (1991)

[13] J. A. Prybyla, T. F. Heinz, A. Kalamarides, M. M. T. Loy and J. A. Misewich, Surf. Sci. **283**, 143 (1993)

[14] A. Peremans, K. Fukutani, K. Nase and Y. Murata, Phys. Rev. B **47**, 4135 (1993)

[15] F. –J. Kao, D. G. Busch, D. Cohen, D. Gomes da Costa and W. Ho, Phys. Rev. Lett. **71**, 2094 (1993)

[16] H. T. Liu and Z. Wu, Phys. Rev. Lett. **72**, 3891 (1994)

[17] D. Burgess, Jr., R. R. Cavanagh and D. S. King, J. Chem. Phys. **88**, 6556 (1988)

[18] J. C. Tully, Surf. Sci. **111**, 461 (1981)

[19] D. A. Mantell, R. R. Cavanagh and D. S. King, J. Chem. Phys. **84**, 5131 (1986)

[20] D. Burgress, Jr., R. Viswanathan, I. Hussla and E. Weitz, J. Chem. Phys. **79**, 5200 (1983)
[21] C. J. S. M. Simpson and J. P. Hardy, Chem. Phys. Lett. **130**, 175 (1986)
[22] J. A. Prybyla, T. F. Heinz, J. A. Misewich and M. M. T. Loy, Surf. Sci. **230**, L172 (1990)
[23] D. S. King and R. R. Cavanagh, in: Molecule Surface Interactions, Ed. K. P. Lawley (Wiley, New York, 1989) p. 45
[24] T. Mull, B. Baumeister, M. Menges, H. –J. Freund, D. Weide, C. Fischer and P. Andresen, J. Chem. Phys. **96**, 7108 (1992)
[25] M. Asscher, F. M. Zimmermann, L. L. Springsteen, P. L. Houston and . Ho, J. Chem. Phys. **96**, 4808 (1992)
[26] S. F. Shane, H. A. Michelsen and R. N. Zare, in: Laser Spectroscopy and Photochemistry on Metal Surfaces, Eds. H. –L. Dai and W. Ho, Advances in Physical Chemistry Series (World Scientific, Singapore, 1995)
[27] J. C. Tully, Surf. Sci. **111**, 461 (1981)
[28] G. S. Higashi, Appl. Surf. Sci. **43**, 6 (1989)
[29] S. J. Lombardo and A. T. Bell, Surf. Sci. Rep. **13**, 1 (1991)
[30] G. P. Brivio and T. B. Grimley, Surf. Sci. Rep. **17**, 1 (1993)
[31] S. A. Buntin, R. R. Cavanagh and L. J. Richter, J. Chem. Phys. **98**, 7651 (1993)
[32] P. M. Chu, S. A. Buntin, L. J. Richter and R. R. Cavanagh, J. Chem. Phys. **101**, 2929 (1994)
[33] Z. C. Ying and W. Ho, J. Chem. Phys. **94**, 5701 (1991)
[34] A. Peremans, K. Fukutani, K. Nase and Y. Murata, Surf. Sci. **283**, 189 (1993)
[35] P. M. Ferm, F. Budde, A. V. Hamza, S. Jakubith, D. Weide, P. Andresen and H. –J. Freund, Surf. Sci. **218**, 467 (1989)
[36] L. J. Richter, S. A. Buntin, D. S. King and R.R. Cavanagh, J. Chem. Phys. **96**, 2324 (1992)
[37] Z. C. Ying and W. Ho., J. Chem. Phys. **93**, 9089 (1990)
[38] F. A. Houle, Phys. Rev. B **39**, 10120 (1989)
[39] L. J. Richter, S. A. Buntin, R. R. Cavanagh and D. S. King, J. Chem. Phys. **89**, 5344 (1988)

[40] K. Fukutani, A. Peremans, K. Mase and Y. Murata, Surf. Sci. **283**, 158 (1993)
[41] S. A. Buntin, L. J. Richter, D. S. King and R. R. Cavanagh, J. Chem. Phys. **91**, 6429 (1989)
[42] F. Weik, A. de Meijere and E. Hasselbrink, J. Chem. Phys. **99**, 682 (1993)
[43] Z. –J. Sun, S. Gravelle, R. S. Mackay, X. –Y. Zhu and J. M. White, J. Chem. Phys. **99**, 10021 (1993)
[44] K. Leggett, J. C. Polanyi and P. A. Young, J. Chem. Phys. **93**, 3645 (1990)
[45] St. J. Dixon-Warren, K. Leggett, M. S. Matyjaszcyk, J. C. Polanyi and P. A. Young, J. Chem. Phys. **93**, 3659 (1990)
[46] J. C. Polanyi and P. A. Young, J. Chem. Phys. **93**, 3673 (1990)
[47] E. Hasselbrink, S. Jakubith, S. Nettesheim, M. Wolf, A. Cassuto and G. Ertl, J. Chem. Phys. **92**, 3154 (1990)
[48] St. J. Dixon-Warren, E. T. Jensen and J. C. Polanyi, J. Chem. Phys. **98**, 5938 (1993)
[49] T. L. Gilton, C. P. Dehnbostel and J. P. Cowin, J. Chem. Phys. **91**, 1937 (1989)
[50] E. P. Narsh, F. L. Tabares, M. R. Schneider, T. L. Gilton, W. Meier and J. P. Cowin, J. Chem. Phys. **92**, 2004 (1990)
[51] V. A. Ukraintsev and I. Harrison, J. Chem. Phys. **98**, 5971 (1993)
[52] Q. Y. Yang, W. N. Schwarz and R. M. Osgood, Jr., J. Chem. Phys. **98**, 10085 (1993)
[53] X. –Y. Zhu, J. M. White, M. Wolf, E. Hasselbrink and G. Ertl, Chem. Phys. Lett. **176**, 459 (1991)
[54] M. Wolf, S. Nettesheim, J. M. White and G. Ertl, J. Chem. Phys. **94**, 4609 (1991)
[55] M. Wolf. E. Hasselbrink, G. Ertl, X. –Y. Zhu and J. M. White, Surf. Sci. **248**, L235 (1991)
[56] L. J. Richter, S. A. Buntin, D. S. King and R. R. Cavanagh, Chem. Phys. Lett. **186**, 423 (1991)
[57] S. R. Hatch, X. –Y. Zhu, J. M. White and A. Campion, J. Chem. Phys. **92**, 2681 (1990)
[58] S. R. Hatch and A. Campion, J. Vac. Sci. Technol. A **10**, 2191 (1992)

[59] M. Wolf, X. –Y. Zhu and J. M. White, in: Desorption Induced by Electronic Transitions, DIET V, Eds. A. R. Burns, E. B. Stechel and D. R. Jennison (Springer, Berlin, 1993) p. 53
[60] Q. Y. Yang and R. M. Osgood, Jr., J. Phys. Chem. **97**, 8855 (1993)
[61] X. –Y. Zhu, M. Wolf, T. Huett and J. M. White, J. Chem. Phys. **97**, 5868 (1992)
[62] Z. –J. Sun and J. M. White, J. Phys. Chem. **98**, 4641 (1994)
[63] D. Menzel and R. Gomer, J. Chem. Phys. **40**, 1164 (1964)
[64] P. A. Redhead, Can. J. Phys. **42**, 886 (1964)
[65] P. R. Antoniewicz, Phys. Rev. B **21**, 3811 (1980)
[66] J. W. Gadzuk, L. J. Richter, S. A. Buntin, D. S. King and R. R. Cavanagh, Surf. Sci. **235**, 317 (1990)
[67] P. Feulner, D. Menzel, H. J. Kreuzer and Z. W. Gortel, Phys. Rev. Lett. **53**, 671 (1984)
[68] W. Huebner and K. –H. Bennemann, Z. Phys. B **78**, 131 (1990)
[69] Z. W. Gortel, Surf. Sci. **231**, 193 (1990)
[70] H. L. Fragnito, J. –Y. Bigot, P. C. Becker and C. V. Shank, Chem. Phys. Lett. **160**, 101 (1989)
[71] F. M. Zimmermann and W. Ho., Phys. Rev. Lett. **72**, 1295 (1994)
[72] B. Gumhalter, K. Wandelt and Ph. Avouris, Phys. Rev. B **37**, 8048 (1988)
[73] F. J. Himpsel and Th. Fauster, Phys. Rev. B **49**, 1583 (1982)
[74] I. Kinoshita, A. Misu and T. Munakata, J. Chem. Phys. **102**, 2970 (1995)
[75] N. D. Lang and A. R. Williams, Phys. Rev. B **18**, 616 (1978)
[76] Ph. Avouris and R. E. Walkup, Annu. Rev. Phys. Chem. **40**, 173 (1989)
[77] A. R. Burns, E. B. Stechel and D. R. Jennison, Phys. Rev. Lett. **58**, 250 (1987)
[78] X. –L. Zhou, X. –Y. Zhu and J. M. White, Surf. Sci. Rep. **13**, 73 (1991)
[79] I. Kinoshita, A. Misu and T. Munakata, J. Chem. Phys. **102**, 2970 (1995)
[80] R. M. Jaeger, K. Homann, H. Kuhlenbeck and H. –J. Freund, Chem. Phys. Lett. **203**, 41 (1993)
[81] I. Harrison, J. C. Polanyi and P. A. Young, J. Chem. Phys. **89**, 1498 (1988)
[82] D. Bassi, in: Atomic and Molecular Beam Methods, Ed. G. Scoles, Vol. 1 (Oxford Univ. Press, New York, 1988) p. 180

[83] K. Mase, S. Misuno, M. Yamada, I. Doi, T. Katsumi, S. Watanabe, Y. Achiba and Y. Murata, J. Chem. Phys. **91**, 590 (1989)
[84] K. A. Trentelman, D. H. Fairbrother, P. G. Strupp, P. C. Stair and E. Weitz, J. Chem. Phys. **96**, 9221 (1992)
[85] D. H. Fairbrother, K. A. Briggman, P. C. Stair and E. Weitz, J. Chem. Phys. **102**, 7267 (1995)
[86] R. Zenobi and R. N. Zare, in: Advances in Multi-Photon Processes and Spectroscopy, Vol. 7, Ed. S. H. Lin (World Scientific, Singapore, 1991)
[87] D. Burgress, Jr., R. Viswanathan, I. Hussla and E. Weitz, J. Chem. Phys. **79**, 5200 (1983)
[88] G. Comsa and R. David, Surf. Sci. Rep. **5**, 145 (1985)
[89] P. M, Johnson and C. E. Otis, Ann. Rev. Phys. Chem. **32**, 139 (1981)
[90] D. A. Gobeli, J. J. Yang and M. A. El-Sayed, *Advances in Multiphoton Processes and Spectroscopy*, vol. 1, ed. By S. H. Lin, World Scientific (1984) Chap. 2
[91] J. R. Ackerhalt and J. H. Eberly, Phys. Rev. A **14**, 1705 (1976)
[92] M. Ito, T. Ebata and N. Mikami, Ann. Rev. Phys. Chem. **39**, 123 (1988)
[93] Y. Isono, E. Morikawa and M. Kotani, Chem. Phys. Lett. **125**, 344 (1986)
[94] M. Ito and M. Fujii, Advances in Multiphoton Processes and Spectroscopy, vol. 4, ed. S. H. Lin, World Scientific (1988) p.1
[95] M. Kawasaki, Appl. Surf. Sci. **135** (1998) 1159
[96] J. D. E. McIntyre, Adv. Electrochem. Electrochem. Eng. **9**, 68 (1973)
[97] David W. Lynch and W. R. Hunter, *Handbook of Optical Constants of Solids*, Ed. E. D. Palik , Academic Press (1985) p. 293
[98] R. N. Zare, Molecular photochemistry **4**, 1 (1972)
[99] G. L. Eesley, Phys. Rev. Lett. **51**, 2140 (1983)
[100] J. T. Yardley, *Laser chemistry: processing at the micro level*, *Laser Handbook*, 405 (1985)
[101] J. F. Osmundsen, C. C. Abele and J. G. Edsen, J. Appl. Phys. **57**, 2921 (1985)

4.3 Results

4.3.1 Time-of-flight spectra of photofragment NO

Figure 4-10 shows typical time-of-flight spectra for NO($X^2\Pi_{3/2}$, v"=0, Q-head) as a function of time delay t, which indicates the flight time of the molecule. These spectra were detected by the density detector, therefore, the spectra indicate S(t), which has already explained in Section 4.2.1. The experimental conditions were as follows: the substrate temperature, T = 80 - 140 K, chamber pressure, P = 5×10^{-7} Torr, and dissociation wavelength, λ = 193 nm. The spectra are simulated with a combination of v^3 Maxwell-Boltzmann

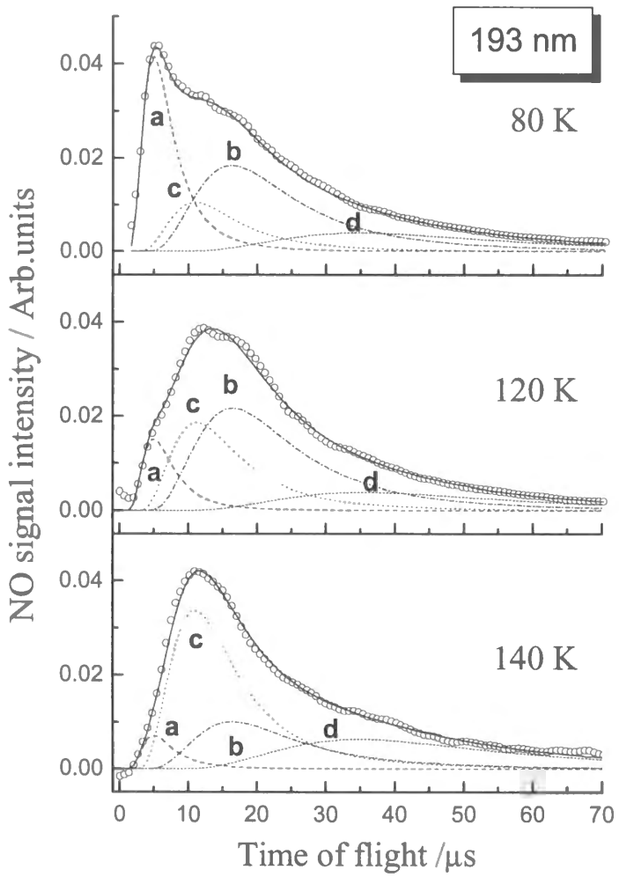

Fig. 4-10. Resonance-enhanced multiphoton-ionization time-of-flight (REMPI-TOF) spectra for NO($X^2\Pi_{3/2}$, v = 0, Q-head from the 193 nm photodissociation of N_2O_4 on polycrystalline Au(111) as a function of delay time between the dissociation and probe laser pulses. Temperatures shown in the figure are for the Au substrate. Curve (a) corresponds to a Maxwell-Boltzmann energy distribution with T_{trans} = 1400 K, (b) 150 K, (c) 270 K and (d) 30 K

translational energy distributions for different translational temperatures, T_{trans}. Component (a) corresponds to T_{trans} = 1400±100 K, (b) 150±20 K, (c) 270±20 K and (d) 30 K. The component (d) is considered to be false signals caused by NO photofragments that are once scattered and bounced back to the detection region. Relative contribution of the components (a), (b) and (c) depends on the substrate temperatures, reflecting the difference in adsorption states of N_2O_4. It also depends on the dissociation wavelengths. Figure 4-11 shows typical time-of-flight spectra of NO(v=0) from the photodissociation at 193 and 351 nm under the same experimental conditions, T = 85 K and P = 5×10^{-8} Torr. At 193 nm the fast component (a) with T_{trans} = 1400 K is dominant, while the slow component (b) of T_{trans} = 170 K is dominating at 351 nm.

The inset of Fig. 4-11 shows NO(v=3) that was produced in the 193 nm

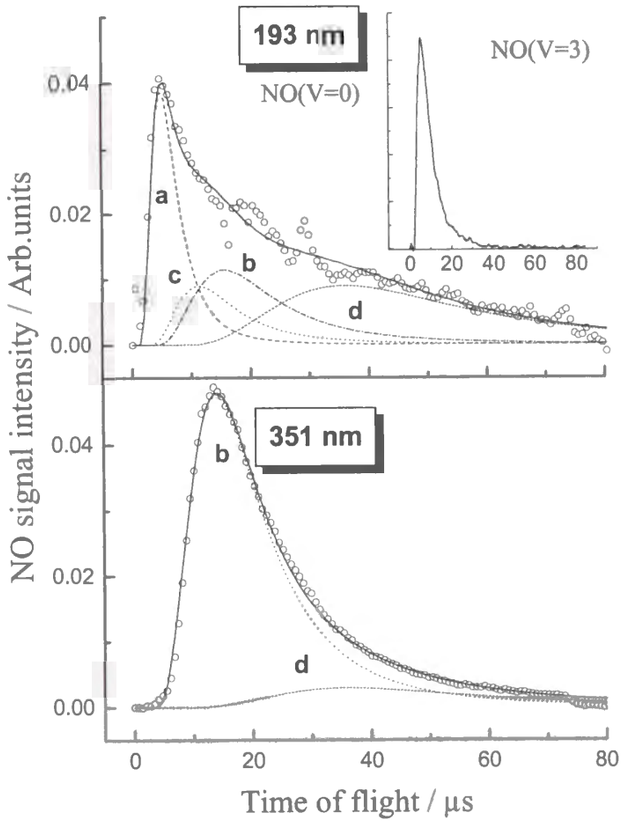

Fig. 4-11. REMPI-TOF spectra of NO(X, v=0, Q-head) from the photodissociation of N_2O_4 at 193 and 351 nm. Curves marked with a, b and d correspond to Maxwell-Boltzmann distributions with T_{trans} = 1400, 150, 270 and 30 K. The inset shows REMPI-TOF spectrum of NO(v=3) at 193 nm, which consists of component (a). In the photodissociation at 351 nm, NO(v=3) was not produced.

photodissociation. The observed TOF spectrum for NO(v=3) consists of the fast component (a). High vibrational excitation of NO(v=0-9) was previously reported in the 248 nm photodissociation of N_2O_4 adsorbed on a LiF (001) crystal surface by Dixon-Warren *et al*. In our experiment, NO (v=3) was not detected at 351 nm because of its insufficient photon energy to produce vibrationally excited NO(v).

4.3.2 Rotational spectra of photofragment NO

Figure 4-12 shows the rotational spectra of NO(X, v=0, J) that was probed for the transition ($A^2\Sigma$, v'=0, J' - $X^2\Pi_{3/2}$,v"=0,J") at two different TOF positions, Δt = 5 and 13 μs, for the 193 nm photolysis, and at one peak position,

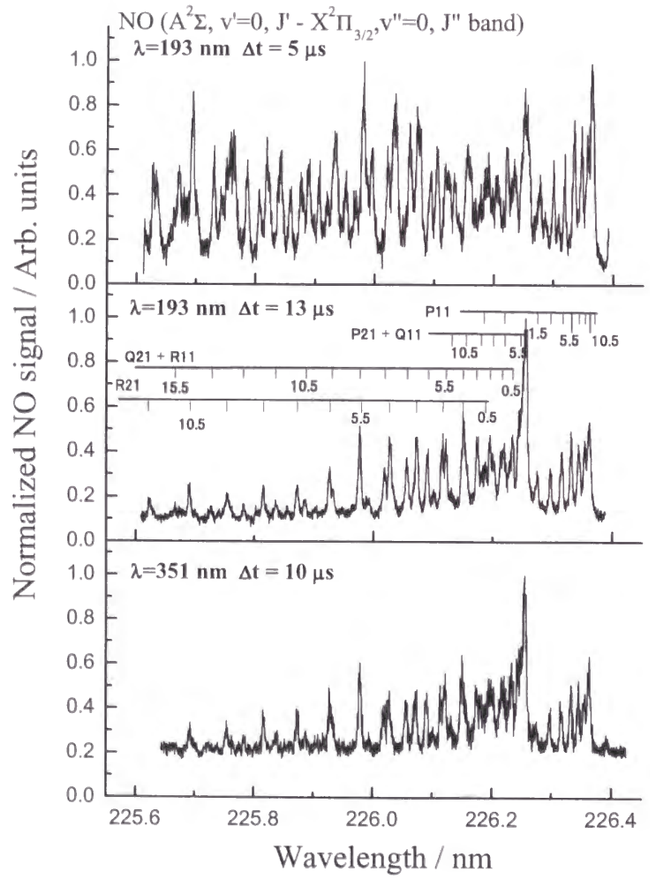

Fig. 4-12 Rotational spectra of NO(A- X, 0-0,) at different TOF positions, Δt = 5 and 13 μs, for the 193 nm photolysis, and at Δt = 10 μs for 351 nm. T = 85 K and P = 5×10^{-8} Torr.

10 μs for 351 nm under the conditions, T = 85 K and P = 5×10^{-8} Torr. The top spectrum of Fig. 4-12 shows a hot rotational band of NO from the photodissociation at 193 nm and Δt = 5 μs. The observed spectrum is congested in the R-band region, because the transition due to NO($X^2\Pi_{1/2}$, v"=0, P-branch) overlaps NO($X^2\Pi_{3/2}$, v"=0, R-branch). The middle panel of Fig. 4-12 shows a rather cold spectrum observed at Δt = 13 μs. By simulating the spectra for non-overlap region, rotational temperatures are estimated for the 5 and 13 μs peaks to be T_{rot} = 600 and 80 K, respectively. At 351 nm and Δt = 10 μs, T_{rot} is 200 K. These rotational temperatures are not in agreement with the corresponding translational temperatures, T_{trans} = 1400 K (5 μs), 270 K (10 μs) and 150 K (13 μs). Because the TOF signals at a certain Δt composed of two or more M-B distributions, the rotational temperatures observed are averaged ones between the corresponding translational temperatures. It is safe to say that the faster photofragment has the higher rotational temperature. Hasselbrink et al. reported a positive linear correlation between the translational temperatures and rotational energies of the NO fragments from the 193 nm photodissociation of adsorbed N_2O_4. The relation of their results is approximated by T_{trans} (K) = 0.5 T_{rot} (K) + 700. Our results are also approximated by a similar equation: T_{trans}= 1.9 T_{rot} (K) + 140.

4.3.3 Power dependence of NO signal intensity

In order to make sure the number of photons involved in the photoexcitation processes, laser power dependence was measured at 193 and 351 nm at T = 85 K and P = 5×10^{-8} Torr. As shown in Fig. 4-13, the power dependence of the signal intensity was linear, suggestive of one-photon process for the photodissociation. Typical laser intensities used in the present experiment were 1 mJ cm^{-2} at 193 nm and 5 mJ cm^{-2} at 351 nm. Both laser intensities satisfy the condition of one-photon dissociation.

Meanwhile, an evidence of the laser induced thermal desorption is not observed in this experimental condition. Calculated temperature rise is ~3 K at the highest photon flux conditions in each wavelength, that is presented in the Table 4-2. The reason of the low temperature rise is due to its large thermal conductivity of the substrate.

Comparison of the two lines gives relative desorption yield $\phi(\lambda)$ of NO at 193 and 351 nm, which yields ϕ(193 nm)/ϕ(351 nm) = 2.9. This ratio will be discussed in Section 3.8.

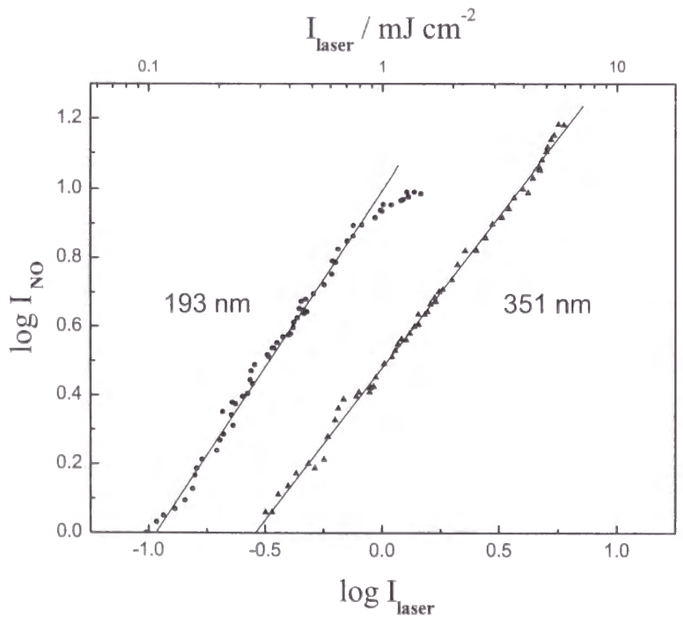

Fig. 4-13 Dependence of NO(X, v=0, Q-head) signal intensity on dissociation laser intensity. The unit slopes are suggestive of one-photon dissociation pathways in these laser intensities. T = 85 K and P = : 5×10^{-8} Torr

4.3.4 Effect of layer thickness on time-of-flight spectra

TOF spectra of NO(v=0, Q-head) were measured for various chamber pressures, P = 1 - 10×10^{-8} Torr, under the substrate temperature T = 85 K. Figure 4-14 shows the spectra for 193 and 351 nm. At 193 nm, both the fast and slow components (a) and (b) appear. Component (d) is the false signal described before. As the consequence of the pressure increases, the absolute signal intensity increases. The TOF shapes for three different pressures are essentially the same to each other at 193 nm. However, at 351 nm the TOF shape changes drastically as a function of pressure. The fast component that appears at Δt = ~ 5.5 μs is dominating for P = 1×10^{-8} Torr. With increasing P, the slower component (b) becomes dominant. The absolute signal intensity initially

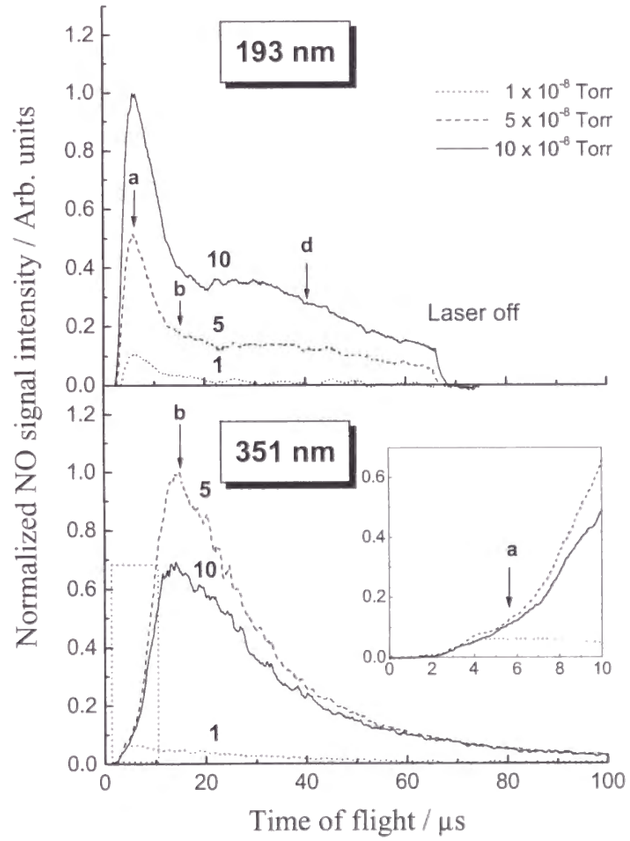

Fig. 4-14 Effect of chamber pressure or thickness of layers of N_2O_4 on time-of-flight spectra of NO(v=0) from the photodissociation of N_2O_4 on Au at 193 and 351 nm. The numbers indicated are the chamber pressures in units of 10^{-8} Torr. The inset shows an expanded area near the origin.

increases with pressure up to P = 5×10^{-8} Torr, and then starts decreasing. The pressure effect, or the effect of thickness of N_2O_4 layers on the signal intensity is shown quantitatively in Fig. 4-15. At 351 nm, the NO(v=0, Q-head) intensity of component (b) increases initially, and then decreases at P > 5×10^{-8} Torr. However, at 193 nm the intensity of component (a) increases linearly. Similar behavior was observed in the 248 nm photodissociation of CH_3Br on brominated Ni(111) by Marsh et al. [1] They reported that the surface mediated slow signal starts decreasing at 3 ML region, but the fast signal that comes from the photodissociation of top layers increases linearly up to 10 ML.

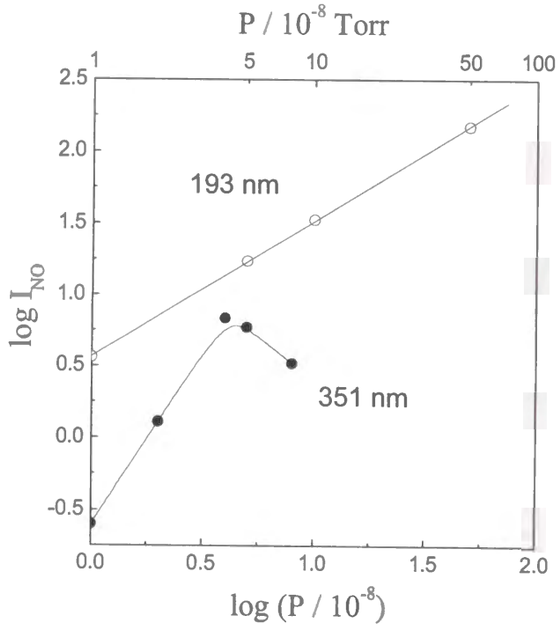

Fig.4-15 Chamber pressure dependence of signal intensities of NO(X, v=0, Q-head). Curves are for eye clarity. Signal intensities measured are for component (a) of Fig. 4-14 at 193 nm and for component (b) at 351 nm.

4.3.5 REMPI detection of NO photofragment for temperature programmed desorption spectroscopy (REMPI-TPD)

The molecular beam of NO_2 from the pulsed valve was synchronized to the dissociation laser's trigger. Direct expansion of the gas toward the cooled Au surface resulted in formation of N_2O_4 multilayers. The delay between the valve and laser trigger was set to achieve an intermitted dosing regime. The surface was replenished between the photodissociation laser shots. TOF signal intensities were measured as a function of the Au substrate temperature. We refer this measurement to REMPI-TPD, in which photodesorbed NO was probed by the REMPI method with increasing Au substrate temperature at a rate of 2 K s^{-1}. Figure 4-16 shows REMPI-TPD spectra of NO(v=0) at two different chamber pressures, P = 1×10^{-8} and 2×10^{-8} Torr with 193 nm irradiation. Figure 4-16 shows that the spectrum for P = 1×10^{-8} Torr has a broad peak at 206 K. For P = 2×10^{-8} Torr, the spectrum becomes strong in intensity and

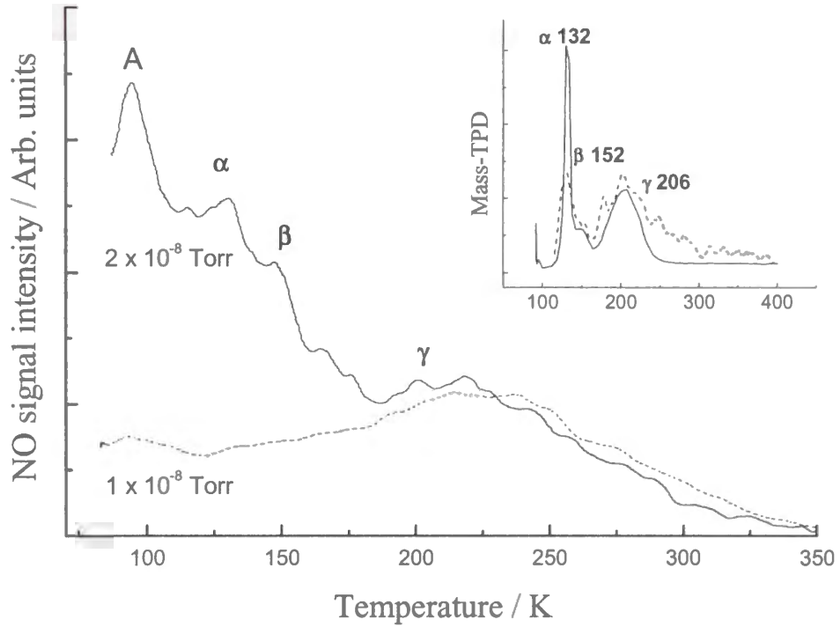

Fig. 4-16 REMPI signal intensities of NO(v=0, Q-head) as a function of substrate temperature at two different chamber pressures, P = 1×10^{-8} and 2×10^{-8} Torr. The Au substrate temperature was increased at a rate of 2 K s^{-1}. The inset shows a conventional temperature programmed desorption of NO_2 from N_2O_4 (1.6 ML) on Au without photon irradiation, using a mass spectrometer. (Ref. [2])The dotted line in the inset indicates the differential of the spectrum obtained at P = 2×10^{-8} Torr.

complicated in shape, which is characterized by three different temperatures, 132, 152 and 206 K. Each temperature corresponds to the peak, α132, β152 or γ206 of the inset that is a conventional TPD spectrum of NO_2 from N_2O_4 (1.6 ML) on Au(111) without photon irradiation, using a mass spectrometer.[2]) The dotted line in the inset indicates the differential of the spectrum obtained at P = $2x10^{-8}$ Torr. The two spectra in the inset are excellently corresponding to each other at the respects of the peak position and shape.

4.3.6 Dependence of signal intensity on polarization of the incident light

Using a pile-of-plate polarizer, the excimer laser light was linearly polarized. Measured degree of polarization ρ was 0.90 at 193 nm and 0.95 at 351 nm. We examined the polarization dependent desorption yields of NO(v=0) by changing the direction of electric vector of incident laser light from parallel (p polarization) to perpendicular (s polarization) with respect to the plane of incidence. In our experiment the angle of incidence φ was fixed at π/4. At 80-120 K and for P = $2\text{-}5\times10^{-8}$ Torr, the ratios of I_s/I_p were measured and presented in Table 4-1. After correction for incomplete polarization of the excimer laser light, the ratios are temperature-independent, and 0.88±0.05 for the fast signal at 193 nm, 0.75±0.05 for the peak signal at 248 nm, and 0.65±0.03 at 351 nm.

As a test, N_2O_4 was deposited on amorphous surface of water ice and irradiated at 193 nm. The ratios of I_s/I_p was unity due to random orientation of N_2O_4 on the amorphous ice surface. Since an electron transfer from the substrate to adsorbates through the first water layer is prohibited according to Cowin and coworkers in Ref. [3], it is unlikely that the dissociation takes place via the surface mediated processes. Thus, randomly oriented N_2O_4 absorb directly UV photons to dissociate at 193 nm. The polarization effect seen for the N_2O_4 multilayers on Au suggest different energy transfer processes at different dissociation wavelengths.

4.3.7 Formation of $O(^3P)$ atoms

Two-photon REMPI signals of $O(^3P_2)$ were detected at 225.7 nm from the N_2O_4 photodissociation at 193 nm as shown in Fig. 4-17. Similarly, at 248 nm $O(^3P)$ atoms were found, while at 351 nm no signals were detected. The TOF spectrum has four components (T_{trans} = 24000, 5100, 1035 and 157 K). The slow component is the false signal as which described for one of NO signal before. The fast three components come from the photodissociation of the topmost layer of N_2O_4. These results are consistent with the fact that a part of oxygen atoms produced are remain trapped on the Au surface as reported by Sato *et al.* [2] and Wang et al. [4] The trapped oxygen atoms appear as surface oxygen molecules in the temperature desorption spectrum at > 500 K. Thus, at 351 nm, since photodissociation takes place near the surface with overlayers, oxygen atoms cannot leave to the gas phase from the bottom of the layers.

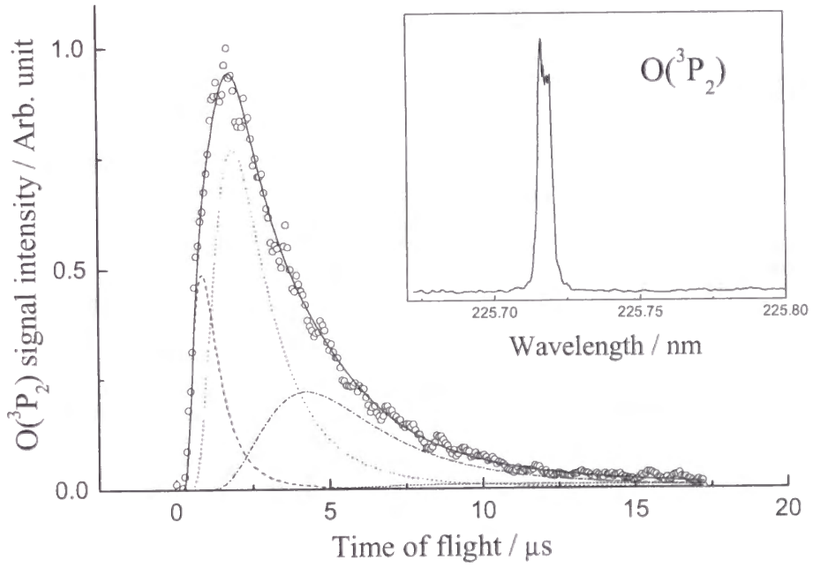

Fig. 4-17 Two-photon REMPI signals of $O(^3P_2)$ at 225.7 nm from the N_2O_4 photodissociation at 193 nm. No signals of oxygen atoms were detected at 351 nm. The inset shows a excitation spectrum of Two-photon REMPI signals of $O(^3P_2)$ around 225.7 nm. Dotted curves correspond to Maxwell-Boltzmann distributions with T_{trans} = 24000, 5100, 1035 and 157 K.

4.3.8 Relative photoabsorption efficiencies at 193, 248 and 351 nm

Data were collected without the intermittent dosing regime for measurement of relative photoabsorption efficiency. The surface was first dosed with NO_2 for P = 1×10^{-7} Torr and 2 min the pulsed molecular beam was turned off during the photoirradiation. The signal intensity of NO(v=0) decreased as the number of laser shots increased. The data were analyzed according to the following equation:

$$N = N_0 \exp(- \sigma n_{hv}), \qquad (4.59)$$

where N_0 is the initial amount of N_2O_4, σ the photodissociation cross section, and n_{hv} the total number of photon irradiated. The observed ratios, σ(351 nm)/ σ(248 nm)/ σ(193 nm) were 0.2/0.8/1. These ratios are much different from the gas phase ones, σ(351 nm)/ σ(248 nm)/ σ(193 nm) = 0.013/0.016/1 [5], and also the absorption coefficient of Au metal at the incident angle of π/4, σ(351 nm)/ σ(248 nm)/ σ(193 nm) = 0.82/0.86/1. As measured in Section 4.3.3, the ratio of the desorption yields of NO(v=0) is ϕ(351 nm)/ϕ(193 nm) = 0.34/1, while the present σ(351 nm)/ σ(193 nm) is 0.2/1. This discrepancy is due to the contribution of the higher vibrational levels of NO(v≥1) at 193 nm, which is comparable to that of NO(v=0).

References

[1] E. P. Marsh, F. L. Tabares, M. R. Schneider, T. L. Gilton, W. Meier, J. P. Cowin, J. Chem. Phys. **92**, 2004 (1990)

[2] S. Shinri, T. Senga, M. Kawasaki, J. Phys. Chem. B **103**, 5063 (1999)

[3] T. L. Gilton, C. P. Dehnbostel and J. P. Cowin, J. Chem. Phys. **91**, 1937 (1989)

[4] J. Wang,; M. R. Voss,; H. Busse,; B. E. Koel, J. Phys. Chem. B **102**, 4693 (1998)

[5] Bass, A.M. A. E. Ledford, Jr. , A.H. Laufer, J. Res. Natl. Bur. Stand. Sec. A **80**, 143(1976)

4.4 Discussion

4.4.1 REMPI-TPD and number of monolayers of N_2O_4 on Au

Bartram and Koel, and Sato et al. investigated the adsorption state of NO_2 on Au(111) using TPD, HREELS (high resolution electron energy loss spectroscopy) [1] and IRAS [2, 3]. At 100 K, NO_2 is adsorbed molecularly to form a Au-O,O nitroso surface chelate with C_{2v} symmetry, which is referred to chemisorbed NO_2. The saturation coverage of chemisorbed NO_2 is 0.4 ML. Pure adlayer of chemisorbed chelating NO_2 was prepared by forming the layer and heating up to 185 K. After the chemisorbed state is saturated, crystalline N_2O_4 multilayers are formed at 100 K with large exposures of NO_2. Crystalline N_2O_4 multilayers are aligned preferentially with the C_2 axis perpendicular to an Au(111) surface. The inset of Fig. 4-16 shows three different peaks, α132, β152 or γ206 of that is a conventional TPD spectrum of NO_2 from an Au(111) surface with a mass spectrometer. [3] The 206 K peak in the TPD is attributable to chemisorbed NO_2 on Au(111).

In order to control number of surface molecular layers, n_L, the backfill method is usually used and an unit of "Langmuir" is a measure of n_L. In our experiment, however, we cannot estimate the dose rate by this unit, because NO_2 from the pulsed nozzle was expanded directly toward the cooled Au surface with the pulsed exposure of the molecular beam. At 10 Hz occasions adsorption and dissociation of the N_2O_4 layers occur alternatively. The author will estimate n_L from REMPI-TPD spectra as described in Section 4.3.5. For P = 2×10^{-8} Torr the REMPI-TPD spectrum of Fig. 4-16 has one broad peak at 206 K. For P = 2×10^{-8} Torr, the spectrum shows three characteristic features at 132, 152 and 206 K. These peaks correspond to α132, β152 and γ206 of the conventional TPD spectrum of NO_2 from an Au(111) surface measured by Sato *et al*. They concluded that three different TPD peaks of NO_2 at γ206, β152 and α132 K are attributable to desorption of chemisorbed NO_2, N_2O_4 adsorbed directly on Au (referred to first layer N_2O_4), and physisorbed NO_2 on the chemisorbed NO_2 (referred to physisorbed N_2O_4), respectively. In our REMPI-TPD experiment with the intermittent dosing regime of N_2O_4 almost all surface molecules were dissociated by one UV laser shot. Therefore, a signal height at a certain temperature corresponds to the amount of N_2O_4 adsorbed on the Au

substrate. Thus, differentiating the REMPI-TPD spectrum and change the sign of it would give a conventional TPD spectrum. The spectrum differentiated thus is shown in the inset by the dotted curve, which is in good agreement with the reported TPD spectrum at 120 - 270 K. The intensity of the α132 K peak at P = 2×10^{-8} Torr is a half of the conventional TPD spectrum for N_2O_4(1.6 ML). Hence, the number of monolayers at α132 K is estimated to be ~0.8 ML in units of physisorbed N_2O_4. By comparing the height at 94 K to that at 132 K, n_L at 94 K can be estimated ~ 1 ML.

Now, we will estimate the number of layers, n_L, under our typical pressure condition, that is, 3 - 5×10^{-8} Torr. Figure 4-14 shows NO signal intensity measured at 193 nm at various chamber pressures. A linear relation between NO signal intensity and chamber pressure is observed with a slope of unity. Thus, n_L is estimated to be ~2 ML for our typical pressure condition of P = 3 - 5×10^{-8} Torr at 80 - 90 K. Similarly at 351 nm, the pressure dependency was measured. The signal intensity increases linearly up to P = 5×10^{-8} Torr or estimated to be ~3 ML. Above this pressure, signal intensity starts decreasing. This estimation of ~3 ML is reasonable if one considers that the photoexcitation process at 351 nm is surface mediated and inhibited by overlayers. The same behavior at 4 ML was reported for surface-mediated photodissociation of CH_3Br on Ni(111). [4]

4.4.2 Effect of adsorption states of N_2O_4 on dissociation dynamics at 193 nm

As shown in Fig 4-16, the adsorption state of N_2O_4 is a function of pressure and temperature. According to IRAS measurement by Sato et al. [3], multilayered N_2O_4 (physisorbed N_2O_4) is aligned preferentially with the C_2 axis perpendicular to the surface. These species disappear at T = 132 K, meanwhile, the first layer N_2O_4 desorb at 152 K. This species is oriented on Au randomly. In Fig. 4-10, the substrate temperature was increased after adsorption of N_2O_4 on Au at 80 K. Then, the adsorption state of the N_2O_4 layers is changed due to thermal rearrangement. Physisorbed N_2O_4 starts desorption at 132 K and first layer N_2O_4 remains on the surface. In Fig. 2, this change in the adsorption state is clearly seen by the change in the relative contributions of three different

components (a), (b) and (c). At T = 80 K, most of N_2O_4 are physisorbed ones that feel weak interaction, giving the fast component (a). At 140 K, most of N_2O_4 are the randomly oriented ones that feel strong interaction with the Au surface, giving slow component (c). The component (b) is attributable to the slowed components by collisions due to the multilayer dissociation. This indicates that the rearrangement of the N_2O_4 adlayer causes the photodesorption energy to reduce. A annealing of the substrate results in the rearrangement, i.e. the crystallization, of the adlayer. The crystallized N_2O_4 releases the absorbed photon energy to neighbor N_2O_4 in some extent. The released energy is estimated to 3.37 kcal/mol, which corresponds 81% of the averaged translational energy of component (a). A strong interaction has to exist in the crystallized N_2O_4 layer.

4.4.3 Energy partition in translational and rotational degrees of freedom at 193 nm

Assuming an impulse model, the resulting torque imparts angular momentum on the NO fragment. Let the momentum of NO be P_{NO} and the angular momentum of NO be J_{NO}, then, $E_t = (P_{NO})^2/2\mu$, and $E_r = (J_{NO})^2/2I$, where μ and I are reduced mass and moment inertia. Using the relation of $J_{NO} = r_{CM} \times P_{NO}$ where r_{CM} is a distance between the center-of-mass of NO and the N atom:

$$E_{rot}/E_{trans} = [m_O/(m_O + m_N)]^2 = 0.28. \quad (4.60)$$

Using $E_{rot} / E_{trans} = T_{rot} / 2T_{trans}$, the experimental ratios are 0.23, which are in fair agreement with the simple momentum conservation rule.

The energy partitioning among solid parent molecules makes the TOF spectra much wider and slower than those of gas-phase photodissociation. This wide distribution reflects energy flow among the oscillators in the N_2O_4 layers. Based on the phase-space theory, the number of effective modes may be estimated by using the following equation for the translational energy distribution if we ignore the rotational degrees of freedom [5]:

$$P(E_t) = E_t^{1/2} (E_{avl} - E_t)^{s-1}, \quad (4.61)$$

where s is the number of vibrational modes over which the vibrational energy is distributed among the multilayer of N_2O_4. Our data are well fitted with s = 40. This number corresponds to about six N_2O_4 molecules, with which the NO

photofragments are energetically relaxed, assuming that the effective vibrational modes is one third of all vibrational degrees of freedom.

4.4.4 Primary processes of N_2O_4 photodissociation on Au

Table 4-4 shows channels that are plausible primary processes from energetic point of view. The Energetics are calculated from the gas-phase thermodynamic values.

Table 4-4 Energetics of decomposition of N_2O_4

			E_{avl}(kcal mol^{-1})		
			λ(nm) = 193	248	351
Process	ΔH(kcal/mol)	Corresponding wavelength to ΔH			
(1) NO_2 + NO + O	88	325	60	26	-
(2) N_2O_3 + O	77	370	71	37	4
(3) NO_3 + NO	37	430	111	77	44

Photodissociation at 351 nm

The photon energy of 351 nm is below the thermodynamical threshold for the formation of NO. However, Hasselbrink et al.[6] reported the formation of NO from N_2O_4 on Pd at 351 nm by laser-induced fluorescence method. Sato et al. [3] measured the formation of NO from N_2O_4 adsorbed on Au at ~ 300 nm with mass spectrometry. In the present experiment, σ(351 nm)/σ(193 nm) on the surface is much larger than that of the gas phase. The effect of the N_2O_4 coverage at T = 85 K is clearly shown in Figs. 4-14 and 4-15. In the inset of Fig. 4-14, the fast component (a) appears in the TOF spectrum for the lower coverage or P = $1x10^{-8}$ Torr. As increasing the coverage to P = $5x10^{-8}$ Torr, the slow component (b) becomes dominant. Further increase of the coverage to P = $10x10^{-8}$ Torr annihilates the signal intensity (Fig. 4-15). The linear relation for the low coverage region indicates that all the layers take part in the photodecomposition process with an equal probability, or constant dissociation cross section. The non-linear relation for the high coverage region indicates that the photoproducts only from the layers near the N_2O_4 – Au interface are released by photoirradiation. These results suggest the surface mediated excitation at 351 nm as well as the monolayer coverage is achieved for P = 1 -

$5x10^{-8}$ Torr. According to Hasselbrink et al. [6] this excitation process is regarded as a sequence of the following processes: (1) electron-hole pairs are produced, (2) the hot carriers propagate to the surface, and (3) they are transferred to the adsorbates. Since the effective work function of Au metal is 5.3 eV and the photon energy at 351 nm is 3.5 eV, this mechanism occurs through the tunneling process. Sato et al. [3] have also proposed the enhancement mechanism by electron transfer from the substrate. A large increase in the work function upon NO_2 adsorption on an Au surface implies significant electron transfer from the substrate to chemisorbed NO_2. [1] Successive electron transfer would occur from the chemisorbed NO_2 to multilayer N_2O_4.

About the effect of polarization of the incident laser light, s- and p-polarized light, I_s/I_p was 0.65±0.03. This ratio is close to that for surface photoabsorption, $(1-R_s)/(1-R_p)$ = 0.68, where R_s and R_p are the reflection coefficients of the Au substrate. This result is in consistent with the surface mediated mechanism. The other possible photoprocess could occur by induced electric field on the Au surface. The induced intensities parallel or perpendicular to the surface are calculated with complex refractive indexes (n and k) and .the angle of incident (ϕ). (details of electromagmetic theory is given by Ref. [6-8] In our case ϕ was fixed at 45°. After Ying and Ho [9)] the microscopic field that the surface adsorbed molecules feel is equivalent to the geometric mean of the macroscopic fields between the vacuum and substrate sides. Thus, we used the dielectric constant ε_{eff} = 2.54. Since the most plausible orientation of the adsorbed molecules is perpendicular to the surface (θ= 0°) and the weak electronic transition of N_2O_4 at 351 nm is Y-polarized or $^1B_{2u}$ in D_{2h}. [10, 11], I_s/I_p is calculated to be 0.718. For the case of random orientation the ratio is 0.567 for θ = 54.7°. Hence, we cannot eliminate the possibility of the excitation process by the induced surface field at 351 nm. However, as stated above, the 351 nm photoprocess is surface-mediated one, in which hot carriers generated in Au are involved. Concerning the surface mediated process, Masson et al.[12] found the ballistic oxygen atoms, $O(^3P)$ and $O(^1D)$, leave the monolayer N_2O covered Pt(111) surface by irradiation at 193 nm. The photodissociation yields of O and N_2 strongly depend on the polarization of the incident laser light. These

results suggest that hot electrons generated near the surface by the photoirradiation attach to N_2O to form a surface N_2O^-. Surface recaptures of the electron and the subsequent decay to neutral species can lead to the decomposition into N_2 + O, as suggested by Kiss et al. [13]. In this dissociation, the NN-O bond is weakened by the attachment of an electron. It is reasonable to assume that a similar dissociation mechanism occurs in the N_2O_4 photodissociation at 351 nm. The electron attachment mechanism is also favored to explain the channel where oxygen atoms remain trapped on the Pt surface after the photodissociation. [3] The following dissociation pathways could be considered at 351 nm(3.5 eV).

$$N_2O_4 \rightarrow NO + O + NO_2 \qquad \Delta H < 3.8 \text{ eV}, \qquad (1)$$

$$e^- + N_2O_4 \rightarrow NO + NO_3^- \qquad \Delta H = -2.6 \text{ eV}. \qquad (4)$$

However, neither NO_2 nor NO_3^- were detected by our previous IRAS measurement in the 300 nm photolysis of multilayer N_2O_4 adsorbed on Au. [3] According to Koch et al. [14] NO_3^- is converted to NO_2 and O^- via a multiphoton process at 325 and 375 nm. Concluding, it seems reasonable to assume that NO_2 or NO_3^- species to form N_2O_4.

Rieley et al. [15] investigated the photodissociation of N_2O_4 multilayers on water layers/Cu at 355 nm. Since the size of the N_2O_4 multilayers was 30 ML, direct photoabsorption process of N_2O_4 generates only NO_2 due to N-N bond scission. No desorption of N_2O_4 occurred at this wavelength. They estimated the translational energy of the NO_2 fragment from the surface is 17 meV or 100 K. This translational temperature is much lower than that of the main component (b) at 351 nm for our case. NO_2 desorption followed by its one-color dissociation process at 226 nm (probe laser wavelength) could give the signal in our case. However, since $O(^3P_j)$ was not detected in our experiment at 351 nm, we can eliminate its possibility. The reaction mechanism on metal surface differs from on water ice.

Marsh et al. [16] reported photoirradiation effect on the thin layer of CH_3 Br on Pt. Upon irradiation, an electron is transferred from the substrate to the adsorbate with an excited hole left on the substrate: $CH_3 + Br^- + Ni^+$ (bulk). The rapid deexcitation of the excited hole induces the adsorbate molecule back to a neutral potential. Then, the molecule dissociates to slow neutral

photofragments. When the signal intensity was monitored as a function of coverage, intensity increased first up to four monolayers (4 ML) and then, decreased drastically. Coupled with the fact that the fragment velocity is slowed relative to the expected gas-phase velocity, it was concluded that the charge transfer process is dominating the fragmentation at low coverage of ~1 ML. This slow channel died off steadily from 4 ML to complete extinction at ~10 ML.

Photodissociation at 193 nm

The photon energies at 193 and 248 nm are well above the threshold energy of the formation of an O atom and NO via processes (1 - 3). Hasselbrink et al. [6] reported the formation of NO from N_2O_4 on Pd at 193 nm by laser-induced fluorescence method. In our experiment, the effect of the coverage of N_2O_4 on the time-of-flight spectrum of NO at T = 85 K is shown in Figs. 4-14 and 4-15. The different behavior observed for excitation at 193 and 351 nm is attributed to difference in the excitation processes. The linear increase of the NO signal intensity for 193 nm suggests the photodissociation of the topmost layer. Thus, only a slight shape change of the TOF spectra is seen for the entire coverage or pressure range P = 1 - $10x10^{-8}$ Torr in Fig. 4-14. These TOF spectra consist of the fast component (a) and slow component (b). The slow one comes from photodissociation of inner layers of N_2O_4, while the fast component comes from that of the top layer or near top layers. The slow photofragments produced in the former process receive many collisions before they come out to vacuum from the layers and are translationally and rotationally relaxed. Actually for the slow component, the rotational temperature is lower than that for the fast one (Fig. 4-12).

About the effect of polarization of the incident laser light, s- and p-polarized light, I_s/I_p was 0.88±0.05 at 193 nm. Although this ratio is close to that for surface photoabsorption, $(1-R_s)/(1-R_p)$ = 0.75, the discussion described above suggests that the dissociation at 193 nm occurs via the direct photoabsorption of N_2O_4 by the induced electric field on the Au surface. The strong electronic transition of N_2O_4 at 185 nm is theoretically and experimentally attributed to Z-polarized or $^1B_1$ in D_{2h}. [17, 18] Using ε_{eff} = 1.84, I_s/I_p is calculated to be 0 for $\theta = 0°$ and 0. 564 for $\theta = 54.7°$. The calculated value for the random

case is in fair agreement with the experimental one. However, the random orientation is not the case according to the IRAS measurement. As will be discussed below, the coverage of N_2O_4 under our typical experimental conditions was two or three monolayers. By the intermittent dosing regime of N_2O_4, the Au surface was replenished between the photodissociation laser shots. Thus, almost all surface molecules were dissociated. Thus, the polarization effect was almost bleached. Actually at 248 nm where the photoabsorption cross section in the gas phase is fairly large, I_s/I_p was 0.75 ±0.05 that is also close to unity.

References

[1] M. E. Bartram and B. E. Koel, Surf. Sci., **213**, 137 (1989)

[2] J. Wang, and B. E. Koel, J. Phys. Chem. B **102**, 4693 (1998)

[3] S. Shinri, T. Senga, M. Kawasaki, J. Phys. Chem. B **103**, 5063 (1999)

[4] E. P. Marsh, F. L. Tabares, M. R. Scheider, T. L. Gilton, W. Meiser, J. P. Cowin, J. Chem. Phys. **92**, 2004 (1990)

[5] R. D. Levine and R. B. Bernstein, *Molecular Reaction Dynamics* (Oxford University, New York, 1974)

[6] E. Hasselbrink, S. Jakubith, S. Nettesheim, M. Wolf, A. Cassuto and G. Ertl, J. Chem. Phys. **92**, 3154 (1990)

[7] J. D. E. McIntyre, Adv. Electrochem. Eng. **9**, 68 (1973)

[8] L. J. Richter, S. A. Buntin, D. S. King, R. R. Cavanagh, Chem. Phys. Lett. **186**, 423 (1991)

[9] Z.C. Ying and W. Ho, J. Chem. Phys. **93**, 9089 (1990)

[10] W. Niessen, W. Domcke, L. S. Cedarbaum and J. Schirmer, J. Chem. Soc. Faraday Trans. II **74**, 1550 (1978)

[11] W.N. Sisk, C. E. Miller and H. S. Johnston, J. Phys. Chem. **97**, 9916 (1993)

[12] D. P. Masson, E. J. Lanzendorf, A. C. Kummel, J. Chem. Phys. **102**, 9096 (1995)

[13] J. Kiss, D. Lennon, S. K. Jo and J.M. White, J. Phys. Chem. **95**, 8054 (1991)

[14] T. G. Koch, N. S. Holms, T. B. Roddis, and J. R. Sodeau, J. Phys. Chem. **100**, 11402 (1996)

[15] H. Rieley, D. J. Colby, D. P. McMurray and S. M. Reeman, J. Phys. Chem. B **101,** 4982 (1997)

[16] E. P. Marsh, F. L. Tabares, M.R. Scheider, T. L. Gilton, W. Meiser, J. P. Cowin, J. Chem. Phys. **92**, 2004 (1990)

[17] J. Mason, J. Chem. Soc. Dalton Tarns. **1**, 19 (1985)

[18] M. Kawasaki, K. Kasatani, H. Sato, H. Shinohara and N. Nishi, Chem. Phys. **78**, 65 (1983)

4.5 Conclusion

N_2O_4 monolayers adsorbed on a polycrystalline Au(111) are photodissociated at 193 and 351 nm. At 193 nm, the adsorbed N_2O_4 are directly excited by induced electric field on the Au surface to produced NO and O. The translational energy distribution of NO correspond to three different translational temperatures: the fast component of T_{trans} = 1400 K comes from the photodissociation of the top-most layers, the slowed component of T = 170 K is attributed to collisions due to the multilayer dissociation, and the intermediate component of T = 280 K comes from the photodissociation of randomly oriented N_2O_4 on Au. At 351 nm, the photodissociation process is induced by an enhancement mechanism via electron transfer from the Au substrate. The production of NO is inhibited by overlayers.

General conclusion

This thesis reports for photochemical reactions of various molecules on various substrates. All of the surface photochemical reactions described in this thesis are well explained in the terms of the 'direct-excitation' of the adsorbed molecule and substrate mediated 'indirect-excitation'. These differences mainly depend on the incident photon energy and the characteristics of the electronic structure for the substrate and adsorbed molecules.

The direct-excitation is observed in the following case:

(1) Adsorbed molecules have large adsorption crosssections around the wavelength of the incident photon.
(2) The surface electric field intensity induced by the incident photon is strong enough for the adsorbate to be excited, because in the near field of the interface between a thin adlayer and the substrate surface the electric field intensity is enhanced or reduced due to the interference of the incident light polarization and incident angle.
(3) The incident photon energy is large enough to dissociate the molecule or brake the bound between the adsorbate and surface, after release of the energy into some degrees of freedom, e.g. a energy transfer to the substrate and the molecule - substrate vibrations.

The rest of energy is shared with degrees of freedom in the molecule, e.g. the translational, vibrational and rotational energy.

On the other hand, in indirect-excitation the substrate absorbs the photon. Therefore, the occasion of this process depends on the substrate band structure. Metal and semiconductor have a large cross section in the visible and ultra-violet region usually due to its free electrons or low band gaps, whereas the insulator dose not have a large cross section in the same region due to its high band gap. Hence, the former substrates can induce the indirect-excitation in the visible and ultra-violet region.

In the case of the metal substrate, the photon energy absorbed by the substrate is mostly used for the photoelectron emission, and the excitation of the free electron, plasmon and phonon. A part of the energy can be transferred to the adsorbed molecule through the excited free electrons. In the case of the

semiconductor substrate, the absorbed photon energy is used for the generation of the free electron and hole, and the excitation of the exciton, plasmon and phonon. Electrons and holes may move for a short lifetime and be recombined near the surface. Excitons also recombines in the short time and releases the energy. Some of them give the energy to the adsorbate by the recombination, which makes the adsorbed molecule excited electronically. Adsorbed molecules electronically excited by such substrate-mediated processes are dissociated or desorbed from surface with some degrees of freedom on the molecule.

In Chapter 1, the photochemical etching reaction of GaAs with Cl_2 and HCl was discussed. Only the 193 nm photoirradiation effect induced by the direct excitation process was observed. The weak photoirradiation effect at 488 nm was induced by indirect excitation effect. Other photoirradiations, 248, 266, 355 and 532 nm, did not induce any photochemical etching reactions.

In Chapter 2 and 3, photochemical reactions of N_2O_4 and N_2O_3 on Au surface was examined. The substrate mediated indirect-excitation process on a metal surface was described in detail. Multilayer N_2O_4 was photodecomposed to NO_2 (for N_2O_4) and NO (for both N_2O_4 and N_2O_3) at < 430 nm. However, when the Au surface was covered with an Insulator layer, which was a thin water ice film (~5 ML), the yields of NO_2 and NO dropped significantly as compared to the bare surface, suggesting that the photodissociation is enhanced by substrate excitation or by electron transfer from the surface to the adsorbates.

In Chapter 4, photochemical reaction dynamics of N_2O_4 on Au surface was investigated. The direct-excitation process of the adsorbed molecule was described in detail. The 193 and 351 nm irradiation induced different molecular dynamics of the desorbed molecule. Basically, these differences are caused by the excitation process, suggesting the 193 nm induces the direct-excitation process, and 351 nm induces the indirect-excitation process.

Consequently, the author could succeed in the investigation of revealing the photochemical reaction process on a surface in some cases in this way. This thinking way of 'direct' or 'indirect' photochemical reaction on a surface can be applicable for all other photochemical reactions on a surface. It will be available for understanding the surface photochemistry.

Acknowledgements

The author would like to thank Professor Masahiro Kawasaki (Kyoto Univ.) for his kind guidance, significant suggestions, and encouragement in the course of this work.

The author acknowledges Professor Shinri Sato (Hokkaido Univ.), Professor Yutaka Matsumi (Nagoya Univ.) and Associate Professor Mitsuo Kawasaki (Kyoto Univ.) for his adequate advises. The author thanks to Dr. Satoshi Hashimoto, Dr. Masafumi Ohashi and Dr. Tomoo Sato for their suggestions especially in the course of the construction of the apparatus.

The author is grateful to his coworkers, Mr. Ryuich Hayashi (Chapter 1), Mr. Akihiro Yabushita and Mr. Yoshihiko Inoue (Chapter 4), for their assistance of experiments. The author would like to thank all members of the Kawasaki laboratory for the many fruitful suggestions.

The author expresses his grateful acknowledgement to Professor Karl Heinz Gericke (Technical University of Braunschweig) for his cooperation in the Japan-Germany collaboration.

List of Publications

Chapter 1 Takehito Senga, Yutaka Matsumi, and Masahiro Kawasaki,
"Chemical dry etching mechanisms of GaAs surface by HCl and Cl_2,"
J. Vac. Sci. Technol. B ***14****(5), 3230-3238 (1996)*

Chapter 2 Shinri Sato, Takehito Senga, and Masahiro Kawasaki,
"Adsorption states and Photochemistry of NO_2 Adsorbed on Au(111),"
J. Phys. Chem. B ***103****, 5063-5069 (1999)*

Chapter 3 Shinri Sato, Dai Yamaguchi, Takehito Senga, and Masahiro Kawasaki,
"Photodissociation of N_2O_3 adsorbed on Au(111),"
J. Phys. Chem. B, (in press)

Chapter 4 Takehito Senga, Akihiro Yabushita, Yoshihiko Inoue, Masahiro Kawasaki, and Shinri Sato
"Photodissociation of N_2O_4 multilayers adsorbed on polycrystalline Au(111),"
J. Phys, Chem. B. (submitted for publication)

The following papers are not included in this thesis:

(1) Melanie Roth, Christof Maul, Karl-Heinz Gericke, Takehito Senga, and Masahiro Kawasaki
"State and energy characterization of fluorine atoms in the A band photodissociation of F_2,"
Chem. Phys. Lett. ***305****, 319-326 (1999)*

(2) Akihiro Yabushita, Yoshihiko Inoue, Takehito Senga, Masahiro Kawasaki, Shinri Sato

"Photodissociation of N_2O_4 multilayers adsorbed on low temperature water ice layers," J. Chem. Phys. B. (submitted)

Rewiew

(1) 川崎昌博, 千賀岳人

"光プロセスの反応機構と半導体素子製造への応用"

化学総説, 36, 248-256 (1998)